AN INVESTIGATION ON QUALITY CHARACTERISTICS OF FRICTION STIR WELDING PROCESS

Thesis submitted by

ABHISHEK MANDAL

Doctor of Philosophy (Engineering)

MECHANICAL ENGINEERING DEPARTMENT
FACULTY COUNCIL OF ENGINEERING &TECHNOLOGY
JADAVPUR UNIVERSITY
KOLKATA, INDIA

2024

JADAVPUR UNIVERSITY
KOLKATA-700032, INDIA

INDEX NO.**195/17/E**

REGISTRATION NUMBER: **1011711003**

Title of Thesis: **AN INVESTIGATION ON QUALITY CHARACTERISTICS OF FRICTION STIR WELDING PROCESS**

Name, Designation & Institution of the Supervisor:

Prof. Gautam Majumdar

Former Professor and HOD,

Mechanical Engineering Department,

Jadavpur University,

Kolkata-700032

Name, Designation & Institution of the Co-Supervisor:

Prof. John Deb Barma

Professor,

Mechanical Engineering Department,

NIT Agartala,

Tripura-799046

List of Publications:

Journal Publications:

1. Mandal, A., Barma, J. D., & Majumdar, G. (2024). Effect of tool pin geometries on weld quality of Al/Cu dissimilar friction stir welding. Journal of The Institution of Engineers (India): Series D, 105(1), 211-225. https://doi.org/10.1007/s40033-023-00472-z
2. Mandal, A., Banik, A., Deb Barma, J., & Majumdar, G. (2024). Friction stir welding of two dissimilar metals: weld quality characterization using the wavelet transform approach. Iranian Journal of Science and Technology, Transactions of Mechanical Engineering, 48(3), 1223-1241. https://doi.org/10.1007/s40997-023-00706-1
3. Mandal, A., Banik, A., Deb Barma, J., & Majumdar, G. (2024). Experimental investigation of tool geometries on Al/Cu dissimilar friction stir welded joint for varying rotational speed. Welding International, 38(12), 847–866. https://doi.org/10.1080/09507116.2024.2436103
4. Mandal, A., Banik, A., Deb Barma, J., & Majumdar, G. (2025). Analysis of weld quality in dissimilar friction stir welding of aluminum and copper using characterization of force and torque signals (Accepted in the Journal of Material Engineering and Performance)

Presentation in Conferences:

1. Mandal, A., Barma, J.D. &Bandyopadhyay, A.; EFFECT ON WELD QUALITY OF FRICTION STIR WELDED ALUMINIUM-COPPER JOINTS BY VARYING TOOL TRAVEL SPEED; International Conference on Precision, Meso, Micro and Nano Engineering (COPEN 2019), IIT Indore.
2. Mandal, A., Barma, J.D. & Majumdar, G.;Effect on material flow for different tool pin geometries in dissimilar FSW;2nd International Conference on Mechanical Engineering on January 5& 6, 2024 at Jadavpur University Kolkata India.

Statement of Originality

I, Abhishek Mandal, registered on 11th August 2017 do hereby declare that this thesis entitled **An Investigation on Quality Characteristics of Friction Stir Welding Process** contains literature survey and original research work done by the undersigned candidate as part of Doctoral studies.

All information in this thesis have been obtained and presented in accordance with existing academic rules and ethical conduct. I declare that, as required by these rules and conduct, I have fully cited and referred all materials and results that are not original to this work.

I also declare that I have checked this thesis as per the "Policy on Anti Plagiarism, Jadavpur University, 2019", and the level of similarity as checked by iThenticate software is 7%.

Signature of Candidate: Abhishek Mandal

Date: 1/7/2024

Certified by Supervisor(s):
(Signature with date, seal)

1. C. Majumdar 01/07/2024

Professor
Dept. of Mechanical Engineering
Jadavpur University, Kolkata-32

2. 01/07/24

Prof. John Deb Barma
Professor, Mechanical Engineering Department
NIT Agartala

CERTIFICATE FROM THE SUPERVISOR/S

This is to certify that the thesis entitled **An Investigation on Quality Characteristics of Friction Stir Welding Process**submitted by Sri. Abhishek Mandal, who got his name registered on 11.08.2017 for the award of Ph.D. (Engineering) degree of Jadavpur University is absolutely based upon his own work under the supervision of Prof. (Dr.) GautamMajumdar, and Prof. (Dr) John Deb Barma thatneither his thesis nor any part of the thesis has been submitted for any degree/ diploma or any other academic award anywhere before.

G. Majumdar 01/07/2024

1. Signature of the Supervisor with Date and Office Seal

Professor
Dept. of Mechanical Engineering
Jadavpur University, Kolkata-32

01/07/24

2. Signature of the Co-Supervisor with Date and Office Seal

Prof. John Deb Barma
Professor, Mechanical Engineering Department
NIT Agartala

ACKNOWLEDGEMENT

The PhD research work was conducted under the supervision of Prof. Gautam Majumdar of the Mechanical Engineering Department at Jadavpur University, Kolkata, India. I also want to express my sincere appreciation to my guide, Prof. John Deb Barma, the Co-Supervisor of my PhD work, whose technical and moral support were instrumental in completing this work. I am immensely grateful to my supervisors for their guidance and valuable suggestions during the experimental and computational work. Special thanks to Prof. Gautam Majumdar for his motivation and inspiration, which were essential for the completion of my Ph.D. I would like to express my gratitude to my supervisor, Late Prof. Asish Bandyopadhyay, under whom I began my PhD journey.The experimental works were carried out at the Workshop of the Mechanical Engineering Department, NIT Agartala. Some parts of the research works were done at the Metrology Laboratory and Metallography Laboratory, Department of Mechanical Engineering, Jadavpur University. I am thankful to all the laboratory assistants of those facilities, including Mr. Ganesh Patra, the laboratory assistant at the Metallography Laboratory. SEM-EDAX studies and were conducted in the Materials and Metallurgy Department at IIT Kharagpur. I am truly grateful to Mr. Mithun Das, the Lab Assistant at the materials and Metallurgy Department, IIT Kharagpur. Special thanks to my colleagues Late Mr. Suman Nihar, Mr. Nabendu Ghosh, Dr. Ranjib Biswas, Mr. Dipanjan Saren, and Dr. Suswagata Poria for their encouragement and assistance in completing this work. I would like to express my gratitude to my friends, Soumya Mukherjee, Anghuman Roy, Nitesh Kumar, Nikhil Kumar, Dwaipayan De and all the other friends who supported me throughout this research period. I am especially thankful to Dr. Abhijit Banik, whose unwavering support was crucial to the success of my PhD research work.

I would like to express my gratitude to my father, Late Mr. Ranjit Kumar Mandal, my mother, Mrs. Nilima Mandal, my elder brother, Mr. Abhijit Mandal, and finally, I would like to thank my wife, Mrs. Jaya Mandal, for her continuous support throughout this journey.

Abhishek Mandal

Abhishek Mandal

Date: 1/7/2024

Place: Kolkata

INDEX

List of Tables

List of Figures

Abstract

Aluminium can be a feasible alternative to copper as both materials possess almost the same electrical and thermal properties. However, at the same time, aluminium is very much less expensive than copper. Aluminium also has low density and high strength. The welding of metals like aluminium and copper has a lot of economic benefits in the electric, aerospace, chemical, electronics, refrigeration, nuclear, and transportation industries. Welding these materials poses a significant challenges they possess different chemical and physical properties, which may result in large intermetallic compounds (IMCs), residual stresses, and cracking formed during welding. Friction stir welding (FSW) is very suitable for joining materials with different physical and chemical properties than conventional fusion welding. The prior benefits are that FSW eliminates distortion, cracks, porosity, and reduce formation of IMCs as no melting occurs during this process. During FSW a non-consumable rotating tool having a specially designed pin and shoulder which has been plunged into adjoining edges of sheets or plates to be welded and moved to joint line. Functions of the tool are to generate frictional heat which leads to plastic deformation of material, movement of workpiece materials and also acts as a reservoir of the hot material under tool shoulder. Weld quality is governed by tool geometry and process parameters which includes tool traverse speed, tool rotational speed, plunge depth etc. The tool experiences different forces and torque during welding. The present work analyzes the effect of different tool geometries on joining aluminium and copper for varying tool traverse speed and rotational speed. These variations affect material flow, heat input, and formation of IMCs, interfacial layer thickness, and force and torque generation and subsequently affect metallurgical and mechanical properties. The investigation includes microstructure and mechanical characterization, and also weld quality prediction based on force and torque signal characterization.

Chapter 1:

Introduction

1.1 Introduction

Applications of welding are so diverse and widespread that every metal industry and engineering branch relies on some form of welding. Scientists and engineers are increasingly focusing on developing methods to combine different materials. This is driven by the growing need across industries for lightweight, strong, versatile, and affordable machine parts and structures[1][2]. Aluminium can be a feasible alternative to copper as both materials possess almost the same electrical and thermal properties. However, at the same time, aluminium is very much less expensive than copper. Aluminium also has low density and high strength [3][4]. The welding of metals like aluminium and copper has a lot of economic benefits in the electric, aerospace, chemical, electronics, refrigeration, nuclear, and transportation industries. Welding these materials poses a significant challenges they possess different chemical and physical properties, which may result in large intermetallic compounds (IMCs), residual stresses, and cracking formed during welding. [5][6][7][8]. Friction stir welding (FSW) is very suitable for joining materials with different physical and chemical properties than conventional fusion welding.FSW was primarily used to join aluminium alloys [9]. However, now, it is widely used for joining dissimilar materials like Al-Cu, Al-Mg, Al-steel, Al-Ti, Al-Inconel, Mg-steel, etc. [10]. The prior benefits are that FSW eliminates distortion, cracks, porosity, and reduces formation of IMCs as no melting occurs during this process [11][12].

1.2 Working Principle of FSW

FSW is categorized as a solid-state welding process that uses a non-consumable rotating tool having an especially designed pin and shoulder which has been plunged into adjoining edges of sheets or plates to be welded and moved to joint line (Fig. 1.1). Functions of the tool are to generate frictional heat which leads to plastic deformation of material, movement of workpiece materials and also acts as a reservoir of hot material under tool shoulder. Different tool geometries cause material movement complexity in nugget. The peak temperature and material movement influence microstructure of friction stir welding. Weld quality is governed by tool geometry, and process parameters include tool traverse speed, tool rotational speed, plunge depth, tool tilt angle, tool pin offset, and dwell time [9][13][14]. The tool experiences different forces and torque during welding, like Z-force or downward force, which plunges the tool into

the materials, and due to X-force or longitudinal force, materials flow around the tool pin when the tool traverses. Spindle torque is primarily responsible for deforming the materials in the stir zone and is generated during tool rotation [14][15].

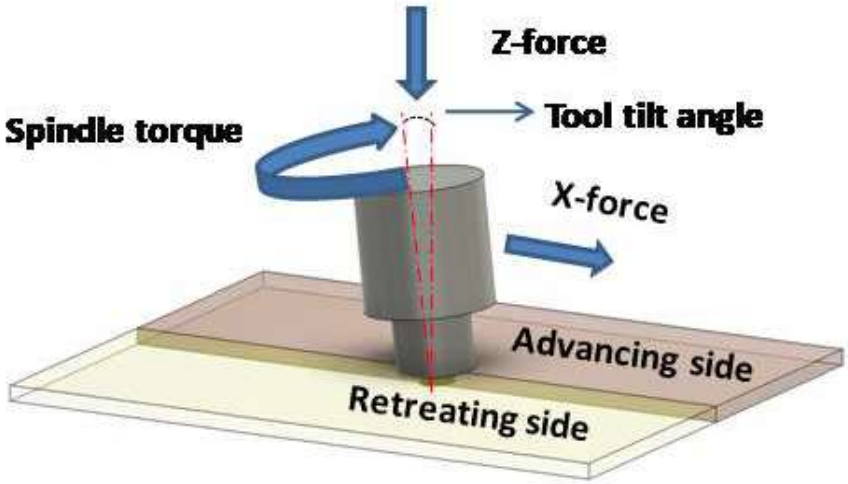

Fig. 1.1 Schematic representation of FSW

1.3 Weld Microstructure

The friction stir welding zone has three distinct zones (Fig. 1.2), namely the nugget or stirring zone at the center of welding, thermo-mechanically affected zone (TMAZ), and heat-affected zone (HAZ), subsequently base metal. Nugget is a region where dynamic recrystallization occurs due to severe plastic deformation by tool pin. In TMAZ, FSW tool has plastically deformed material, and heat generates during welding also affects the region and region on either side of a nugget. HAZ doesn't go through any plastic deformation but experiences a thermal cycle, with change in microstructure and mechanical properties. Parent material has been unaffected by heat and deformation during welding.

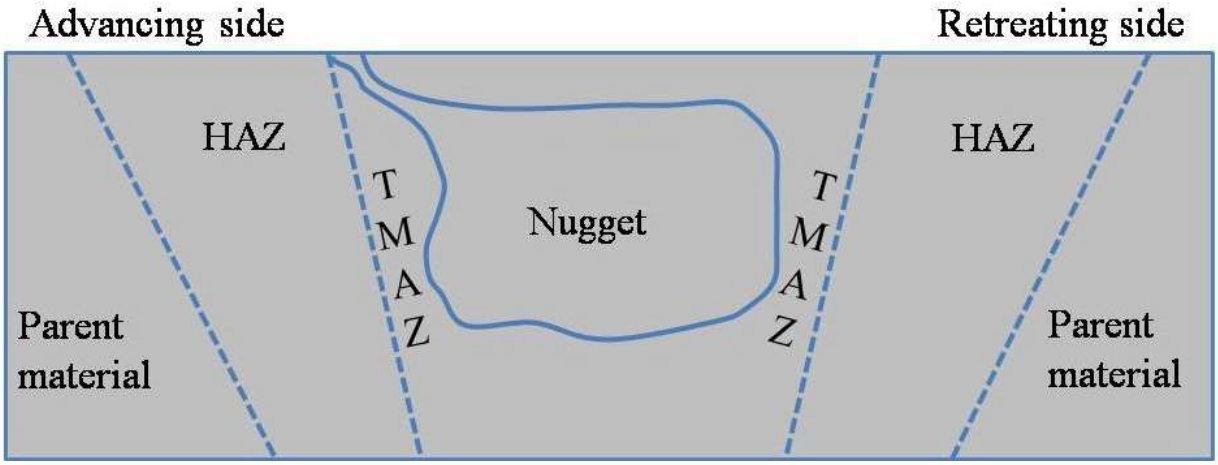

Fig. 1.2 Schematic representation of various weld zones in FSW

1.4 Heat Generation

Heat is generated in the workpiece during welding due to friction and deformation. Adequate heating is essential for proper softening and mixing of material during welding. So, it is crucial to understand the heat generation mechanism for achieving quality welding.

During welding, material may either adhere to tool or have the same velocity as the tool at tool-work interface. But when the velocity is not the same or not in the same direction the condition is called slip. The temperature and normal pressure vary throughout the welding, so, there is not a single contact condition is valid. The contact either partially sticks or partially slipped.

The average heat generation rate considering a purely rotating tool shoulder by the analogy rotary friction welding can be calculated by equation (1.1). For a slipping contact, the power q is given by:

$$q = \frac{2\pi}{3}\mu N\omega R_s^3 \qquad (1.1)$$

where,

μ = coefficient of friction

N= normal pressure

ω= angular velocity (radians/s)

During limit of sticking friction, μN is replaced by a constant shear yield stress k, so the average power generation is:

$$q = 2\pi k\omega R_s^3 \qquad (1.2)$$

Both methods need calibration. Average pressure beneath tool can be roughly calculated from downward force (if measured). However, the coefficient of friction can be adjusted within a physically meaningful range (= 0.2 to 0.5). Similarly, the shear yield stress will be approximately half of tensile yield stress and temperature close to the solidus, but it will need to be adjusted empirically.

For a cylindrical pin with a radius R_p and length L_p rotating at angular velocity ω, the heat generation rate can be represented as follows:

$$q = 2\pi k\omega L_p R_p \qquad (1.3)$$

Relative calculation of heat generation from equations 1.1 and 1.2 shows that heat generation from the pin is insignificant in thin plates but typically 10% or more for thick plates.

The modern Friction Stir Welding (FSW) machine regularly provides torque (T) and angular velocity (ω) values. Therefore, the total heat input can be calculated directly by multiplying T and ω. It is important to note that this calculation neglects the heat generated from translation, which is only about 1% of the total value. Temperature measurement through thermocouples further refines neat heat input.

1.5 Process Parameters

Sound welding can be achieved by controlling the process parameters. The important FSW process parameters are as follows:

- Tool rotational speed
- Tool traverse speed
- Tool plunge depth
- Tool tilting angle
- Dwell time

- Tool pin offset

1.5.1 Tool Rotational Speed

Tool rotation stirs and mixes material. Higher tool rotational speeds create higher temperatures due to frictional heating, leading to intense stirring and material mixing. The rotational speed must be chosen based on materials being joined. Excessive rotation can cause premature tool wear and breakages, tool vibration which will create dangerous conditions.

1.5.2 Tool Traverse Speed

Traverse speed or welding speed is the speed at which a tool passes through abuting edgesof materials to be joined. Material moves from front to back of pin due to the tool's traverse during welding. Traverse speed is also responsible for stirring at a particular instant by the tool during joining. So, a very high traverse speed during welding will cause inappropriate mixing, causing volumetric defects on the joint. A low traverse speed will provide adequate time for material mixing during welding.

1.5.3 Plunge Depth

The plunge depth is the depth of shoulder below the surface of the welded plate. This ensures quality of the weld. Plunging shoulder below the plate surface rises pressure beneath the tool and helps sufficient forging of the material at the rear of the tool.

1.5.4 Tool Tilting Angle

Tool tilt angle is the angle at which FSW tool is positioned with workpiece surface. A suitable tool tilting angle is such that the rear of the tool is lower than the front and which can help this forging process. Zero degree tool tilting angle means tool is perpendicular to the workpiece surface.

1.5.5 Dwell Time

It is the holding time provided to rotating tool before traversing along the joint line as shoulder touches workpiece surface. Generally, as the plunge does not provide sufficient heat, it is

followed by a dwell time to increase the tool and material temperature before welding, which helps the more rigid material around the pin to plasticize and flow easily.

1.5.6 Tool Pin Offset

The tool pin offset refers to shifting of tool towards a specific base material. This is often applied on softer materials, causing significant deformation, while only a few small particles are scattered from harder materials. As a result, a matrix of softer material is effectively mixed with tougher particles. The aim of this is to efficiently produce and disperse heat in both materials.

1.6 Tool Design

FSW material flow is very much influence by tool designs. FSW tool made of a shoulder and a pin, shown in Fig. 1.3. The purpose of tool shoulder is to generate heat through friction and deformation on the surface and sub-surface of the workpiece. It also applies downward forging action to consolidate the weld. Whereas, tool pin or probe disrupt contacting surfaces of workpiece, shear material in front of the tool, and move material behind it. Tool is plunged until the shoulder makes contact with the workpiece. Important factor of tool design are shoulder diameter, shoulder surface angle, pin geometry and also nature of tool surfaces. The concave tool shoulder is produces quality weld and is easy to machine. Some shoulder features increase mixing and produce high-quality welds. These features consist of scrolls (a), ridged (b), grooved(c), knurling (d), and concentric circles (e) as shown in Fig. 1.4, and can be machined into any shoulder profile (concave, convex, and flat).

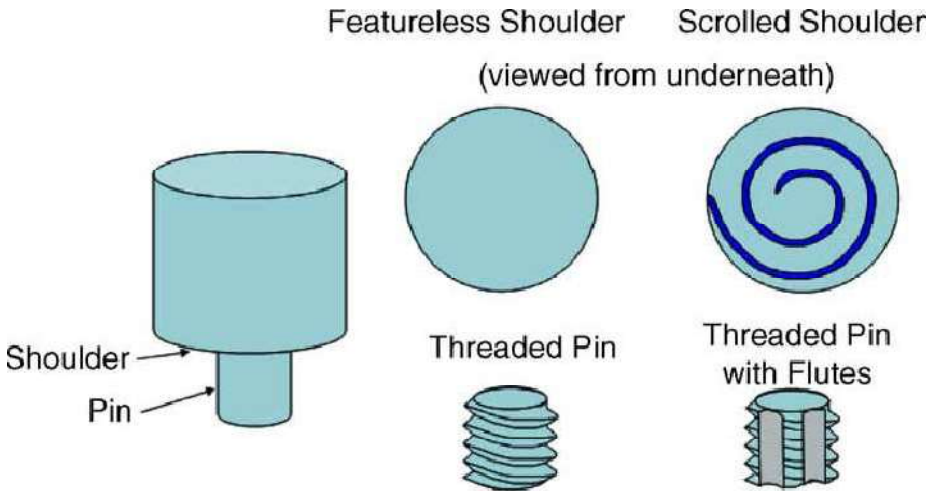

Fig. 1.3 Schematic representation of FSW tool [16]

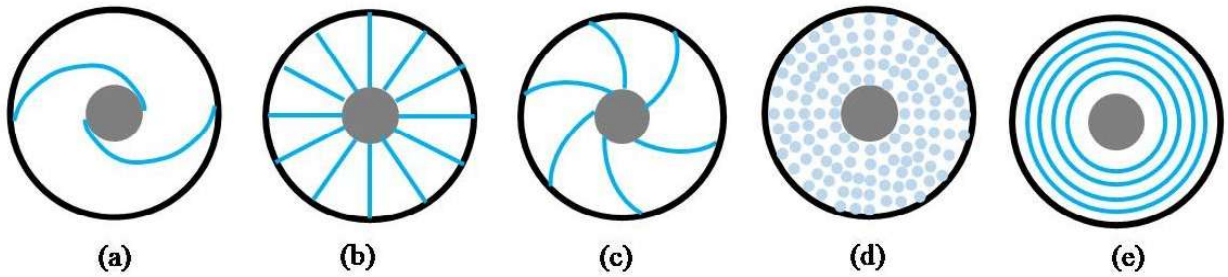

Fig. 1.4 Different shoulder features for improved material flow

The most commonly used pin profile was a circular cross-section, though the shapes of tools have undergone significant changes. Various cross-section shapes, such as triangles, squares, and hexagons, have been experimented with. Some tool pin shapes are shown in Fig. 1.5. Pins have different outer surfaces. It may have thread, flat or may be flutes. Threadless pins are favored for high-strength or highly abrasive alloys because the threaded feature can rapidly wear away. The threadless pin has been used as a baseline for studying material flow. However, threaded pins

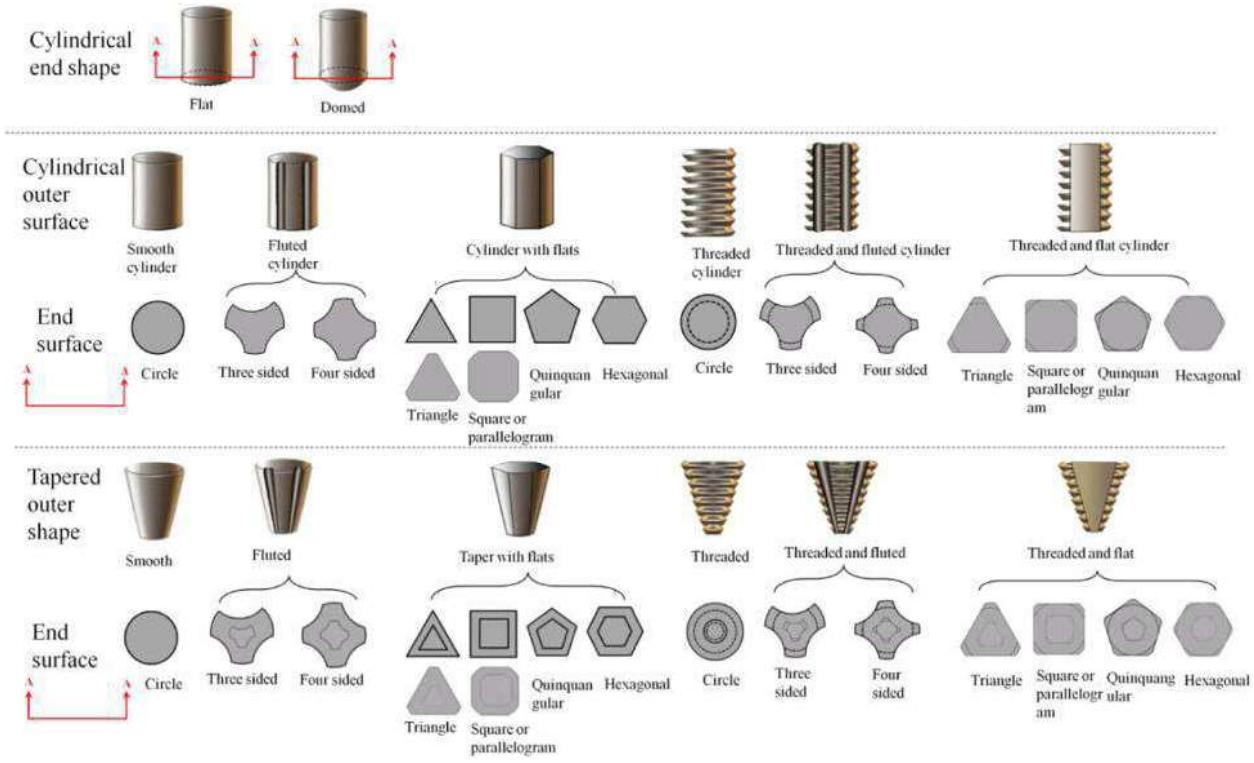

Figure 1.5 Various tool pin shapes[17]

are primarily used in FSW. Threads flow material from shoulder down to bottom of pin. The flat pin can perform better mixing due to lateral flat surfaces, which act as cutters and also trap material and release it behind tool. The flat end shape pin design is mainly used in bottom of pin. However, the main disadvantage of a flat bottom is that it generates high forge force, whereas a round end shape reduces this forge force, which also reduces tool wear. FSW pin may have a tapered outer shape, as indicated in Fig. 1.5. Taper pins have a higher contact area, generating more heat by friction and increasing plastic deformation. A tapered pin also promotes a high hydrostatic pressure in nugget, promoting enhanced material stirring and nugget integrity. But at the same time, this may cause severe tool wear also.

1.7 Tool material

FSW can join a wide range of materials, including magnesium, aluminium, titanium, ferrous metals, copper, metal matrix composites, and dissimilar alloys. Table 1 lists the typical tool material for joining particular alloys.

Table1.1 Different tool materials for different workpiece materials [18]

Workpiece materials	Thickness (mm)	Tool material
Alluminium alloys	< 12	Tool steel, WC-Co
	< 26	MP159
Magnesium alloys	< 6	Tool steel, WC
Copper and copper alloys	< 50	Nickel alloys, polycrystalline cubic boron nitride, tungsten alloys
	< 11	Tool steel
Titanium alloys	< 6	Tungsten alloys
Low-alloy steels	< 10	WC, PCBN
Nickel alloys	< 6	PCBN

1.8 Advantages and Disadvantages of FSW

Advantages:

- FSW does not result in hot cracking or solidification cracking, unlike fusion welding.

- After joining, the material experiences less shrinkage and distortion due to lower welding temperatures.
- FSW does not require filler materials, flux, or shielding gas.
- FSW does not produce fumes, spatter, or UV radiation, making it environmentally friendly.
- The process reduces the need for highly skilled workers due to its repeatability and ease of automation.
- FSW consumes less energy than conventional methods, making it more energy-efficient.
- It can join dissimilar materials, plastics, and composites.
- In most applications, there is no need for special edge preparation but which was found in fusion welding.

Disadvantages:

- An exit hole is left after a withdrawing tool is used to join the materials.
- FSW needs more force to push the welding tool into the metal and move it along the seam. This means a stronger clamp to hold the pieces together compared to arc welding.
- Because FSW doesn't add any material, the gap between the two pieces of metal needs to be very small and precise. Any big gaps can mess up the weld.

1.9 Applications

As discussed earlier, FSW has many advantages over the conventional fusion welding process, and it can also join dissimilar materials; it has a wide variety of applications in different industries. These are as follows:

1.9.1 Ship Building and Maritime Industries

- Panels for decks, sides, bulkheads, and floors
- Aluminium extrusions
- Hulls and superstructures
- Helicopter landing platforms
- Marine and transport structures

1.9.2 Aerospace Industry

- Wings, fuselages, empennages
- Cryogenic fuel tanks for space vehicles
- Aviation fuel tanks
- External throw-away tanks for military aircraft

1.9.3 Automobile and Land Transportation

- Engine and chassis cradles
- Wheel rims
- Truck bodies
- Tail lifts for lorries
- Mobile cranes
- Armor plate vehicles
- Fuel tankers Caravans

1.9.4. Railway Industry

- railway wagon and coachwork
- underground carriages
- rolling stock of railways
- Trams
- bulk carrier tanks

1.9.5 Other Areas

FSW is used to manufacture heat sinks. In the electrical industry, FSW applications include welding of electrical connectors, bus bars, electric motor housings, etc. FSW also produces components like refrigeration panels, cooking equipment, kitchens, etc. [19].

1.10 Organization of the Thesis:

This thesis related to friction stir butt welding of AA1100 and commercially pure copper. It consists of seven chapters, briefings of which are listed below.

Chapter 1 gives a general introduction to FSW, its working principle, heat generations, process parameters, advantages and disadvantages, and applications. Oganisation of the thesis is also mentioned here.

Chapter 2 reviews past literature on FSW, including process parameter, tool design, and real-time monitoring. The objective of the thesis is also discussed here.

Chapter 3 deals with selection of tool material, weld parameters, the experimental setup and procedures adopted for the present investigation.

Chapter 4 discusses the effect of tool geometries on weld quality characterization for varying tool traverse speed.

Chapter 5 discusses the effect of tool geometries on weld quality characterization for varying tool rotational speed.

Chapter 6 explains how the analysis of force and torque signals characterizes the quality of the welds.

Chapter 7 summarizes the key findings of this research work on FSW and discusses potential areas for future research on this technology.

Chapter 2:

Literature Review

and

Objective of Present Work

2.1 Introduction

Aluminium and copper joints are used in electrical connectors, bus bars, foil conductors in transformers, windings for capacitors and condensers, refrigeration tubes, heat exchanger tubes, and tube sheets, among other applications [20]. In this chapter, a review of past research works on the effect of process parameters and tool designs on weld quality characterization in dissimilar FSW of aluminium and copper is presented. The discussion focuses on material flow behavior, microstructure, IMC formation, and the influence on interfacial layer thickness, mechanical strength, and hardness of the welds. Additionally, relevant literature on weld quality analysis through real-time monitoring techniques is reviewed.

2.2 Effect of Process Parameters

A significant portion of prior research on FSW has investigated the impact of weld parameters on dissimilar joints. Ouyang et al. [21] studied weld joint of 6061 aluminium alloy and copper by varying rotational speed (151–1400 rpm) and traverse speed (57–330 mm/min). They found joining difficult due to the brittle IMCs formed in the weld nugget. IMCs are mainly $CuAl_2$, CuAl, and Cu_9Al_4. They have also observed variation in microhardness ranging from 136 to 760HV in the weld nugget due to IMCs, grain size, and intercalation periodicity.

Xia-wei et al. [3] achieved sound weld of pure copper/1350 aluminium alloy at a rotational speed of 1000 rpm and a welding speed of 80 mm/min and achieved sound weld. They have observed complex vortex-like and swirl patterns in joints. They have also observed that the lamella structure at the bottom of the nugget is more homogeneous than other regions and has higher hardness at the bottom of the nugget zone due to grain refinement and solid solution strengthening. No IMCs were found at the nugget.

Medhi et al. [22] studied the effect of variation in rotational speed on AA 6061-T6 and pure copper 3 mm plates. Welding has been performed at 800 rpm, 1,000 rpm, 1,500 rpm, and 1,800 rpm at a traverse speed of 60 mm/min. They have found that good surface appearance, as well as complex intercalated microstructure, tends to increase and also increase in interfacial layer thickness when rotational speed increases. They have also observed an increase in rotational speed, heat input increases, which increases the formation of IMCs in stir zone, increasing hardness and decreasing tensile strength with a maximum joint efficiency of 77% at 1000 rpm.

Xue et al. [23] investigated the effect of weld parameters (pin offset and rotation rate) and fixed location on the microstructure and mechanical properties of the butt joints of 1060 aluminium

alloy and commercially pure copper at a constant traverse speed of 100 mm/min. They observed that defect-free welding is achieved when Cu is on the advancing side and the tool offsets within 2-2.5mm to the aluminium side. It was also observed that defects were found when the tool rotational speed was low (400 rpm). Whereas at higher rotational speeds (600 rpm, 800 rpm, and 1000 rpm), sound joint strength was observed, but at the same time, bead surfaces were getting poorer.

Zhou et al. [24] also studied the effect of rotational speed on the microstructure and mechanical properties of FSSW 1060 aluminium alloy and T2 copper. The study revealed that higher rotational speeds led to increased temperatures and reduced torque and plunge force due to a higher degree of softening materials. This also formed a hook by extruding Cu into aluminium during stirring. High rotational speed creates a continuous $CuAl_2$-CuAl-Al_4Cu_9laminated layer at the hook interface, whereas at low rotational speeds, the interface had a discontinuous $CuAl_2$ layer. The study also revealed that high tensile properties were achieved at continuous interfacial IMC layer with a proper thickness

Muthu et al. [25] showed the effect of tool traverse speed ranging from 50mm/min to 90 mm/ min on friction stir welded AA1100 H14 and commercially pure copper at 1075 rpm. They revealed the highest tensile strength, 113 MPa, at 80 mm/min due to the fine distribution of particles, which results dispersion strengthening and also grain boundary strengthening due to presence of fine recrystallized grains at stir zone. They have also observed optimum heat input at 80 mm/min of traverse speed, reducing diffusion between Al-Cu at interface and forming a thin nano-scale IMCs Al_2Cu, AlCu, and Al_4Cu_9.

Zhang et al. [26] studied microstructure and mechanical properties at a tool rotational speed of 1050 rpm and traverse speed of 30 mm/min for pure copper and 1060 aluminium alloy. The study revealed an Intercalation structure and mainly IMCs Al_4Cu_9 at the stir zone.The average hardness values in the WN are higher due to a high dislocation density during the extreme plastic deformation involved in FSW.

Medhi et al. [27] investigated the effect of traverse speed (30 mm/min, 90 mm/min, and 150 mm/min) at a constant rotational speed of 800 rpm on friction stir butt-welded of commercially pure copper with AA 6061-T6.They found when traverse speed increases, forces and torque increased due to less heating. However, the EDS analysis shows that the interfacial layer thickness decreased with increased traverse speed due to the lower diffusion of copper into the

aluminium. They have also observed at high traverse speed, presence hard iron aluminium phase, it increases hardness along with IMCs and also decreases tensile strength due to crack initiation.

Tan et al. [28] examined the effect of traverse speeds (varied from 20 mm/min to 40 mm/min) on friction stir welded 5A02 aluminium alloy and pure copper at a constant rotational speed of 1100 rpm. They successfully joined at 20 mm/min with a composite structure made of fine Cu particles and fragments in the Al in the upper part of the WNZ. In contrast, the intercalation and swirl-like pattern were evidenced in the lower part due to a solid stirring effect. They have also observed increased mechanical strength due to composite-like structures and nano-scaled reaction layers, which cause good metallurgical bonding.

Xue et al. [29] examined mechanical properties of friction stir welded 1060 aluminium alloy and commercially pure copper with pin offsetting to aluminium side at a tool traverse speed of 100mm/min and a rotation rate of 600rpm. They found a composite structure with variously sized particles dispersed in the Al matrix at the bottom of nugget zone. The tensile strength and hardness of the composite structure were high due to the strengthening effect of IMC particles. The IMCs are mainly Al_2Cu and Al_4Cu_9. They have also found excellent bending strength at the Al-Cu interface due to forming a continuous and uniform IMC layer.

Shankar et al. [30] investigated the effect of tool traverse speed (128 mm/min, 160 mm/min, and 213 mm/min) and tool offset (0 mm and 1 mm) on friction stir welding of oxygen-free copper and aluminium alloy 1050 at a rotational speed of 640 rpm. They observed defect-free welds and improved tensile strength at 1mm offset at a traverse speed of 160 mm/min and 213 mm/min due to composite structures in the stir zone. They have also found that increased traverse speed forms less IMCs layer thickness and less IMCs due to less heat input, which improves joint strength.

Shankar et al. [31] also studied the effect of the combination of FSW parameters (rotational speed and traverse speed) on AA1050 alloy and commercially pure copper joints. Rotational speeds were varied for 1200 rpm and 1400 rpm for two traverse speeds of 40 mm/min and 63 mm/ min. Maximum tensile strength was achieved at 1400 rpm with a traverse speed of 63 mm/ min, which shows a fine-grained microstructure with a large amount of unlike-shaped Cu in nugget.

Bhattacharya et al. [32] investigated effect of welding parameters on material flow, mechanical property, and IMCs on friction stir welded AA6063 to HCP copper dissimilar butt joints without offset. They suggested that a combination of rotational speed and traverse speed provides adequate heat input, and mixing has dramatically influenced the joint strength, whereas insufficient heat input results in improper material flow, which causes sticking and sliding conditions. It is also suggested that forming Al_4Cu_9 and $AlCu_4$ thermodynamically stable intermetallics in lower amounts improves joint strength.

Galvao et al. [33] investigated the surface morphology and mechanical strength of friction stir welded 6082-T6 aluminium to copper-DHP joints by offsetting tool (0 mm to 2.5 mm). Investigation revealed that offsetting tool from the joining interface prevents large IMCs formation, as these IMCs strongly influence the welded joint's surface morphology and mechanical properties. Formation and uneven distribution of IMCs-rich structures over weld surfaces is the main reason for poor surface finish and also the formation of internal decohesion areas inside the nugget, results poor weld strength. At the same time, excessive tool offsetting also forms metallurgical discontinuities which compromise joint strength.

Galvao et al. [34] studied the influence of the friction stir welding parameters on oxygen-free copper with high phosphorous content (Cu-DHP, R 240) and 5083-H111 aluminium alloy. They have observed improper mixing patterns due to lower heat input and also heterogeneous phase composition with significant amounts of Al and Cu and some quantities of Al_2Cu and Al_4Cu_9IMC phases in weld nuggets. Meanwhile, welds with higher heat input increased the homogeneity of nugget with Cu, Cu(Al) solid solution, and Al_4Cu_9. It was also observed that rough welded surfaces are formed due to a $CuAl_2$-rich layer beneath the shoulder.

Mehta et al. [35] studied the effect of a tool tilting angle on mechanical and metallurgical properties on friction welding of AA6061-T651 to electrolytic tough pitch copper. The tool tilt angle was varied from 0° to 4° with 1° interval. Rotational speed was kept constant at 1300 rpm, traverse speed was kept constant at 40 mm/min, and tool pin offset was set at 2 mm on the aluminium side. The study revealed that defect-free joints were achieved when tool tilting angles were 2° to 4° and highest tensile strength was achieved at 4° due to a higher axial plunge load, due to better compressive material flow which filled up defects. Study also revealed that

increasing tool tilting reduces the flash effect and increases the joint's hardness, possibly due to dynamic recrystallization or because of the presence of IMCs.

Hou et al. [36] tried to find effect of tool offsets on aluminium alloy 6061-T6 and commercially pure copper C11000 joints. Tool offset was varied from 0 to 2 mm to aluminium side. They found that the tool offset greatly influences surface quality and joint strength. Tool offset of more than 1.6 mm formed a poor bonding and decreases tensile strength. Study shows that 1.2 mm of tool offset produces maximum tensile strength. The study also revealed that decreasing tool offset increases the contact area between harder Cu and tool surface, which is also responsible for more heat generation thereby favorable for more diffusion of copper to aluminium. This increases the chance of the formation of excessive IMCs of Al-Cu at higher temperatures and has a detrimental effect if the critical thickness of IMCs exceeds.

Sinha et al. [37] investigated friction stir welding of aluminium alloy (AA6351) and pure copper by varying rotational speed from 150 to 900 pm at an interval of 150 rpm at 60 mm/min of traverse speed and a constant turning angle of 2°. They observed that grain size of HAZ and TMAZ increases with rise in rotational speed, and maximum tensile strength was found at 300 rpm. Besides, IMCs like Al_4Cu_9, AlCu, Al_2Cu, and Al_2Cu_3 were found in the nugget of dissimilar joints in aluminium copper.

Akinlabi et al. [38] studied the effect of traverse speed on joining of 5754 aluminium Alloy and C11000 copper. Rotational speed was constant at 950 rpm, and the traverse speed was varied between 50, 150, and 300 mm/min. They observed improved metallurgical bonding and mixing at the lowest traverse speed due to low downward vertical force and high heat input in Al/Cu dissimilar friction stir welding. This resulted in a decrease in tensile strength with increased traverse speed. It was also observed that the higher microhardness value at the Al-Cu interface is due to IMCs and dynamic recrystallization.

Celik et al. [39] investigated the effect of various process parameters on friction stir welding 1050 Al alloys to commercially pure Cu. They observed higher tensile strength due to dispersion strengthening at the stir zone where fine Cu particles dispersed over the Al material in the stir zone. It was also observed that IMCs like $CuAl_2$ and Al_4Cu_9 were found at the stir zone, and increased IMCs decreased the strength and fragility.

2.3 Effect of Tool Design

Apart from these process parameters, researchers also showed that tool design is an important parameter affecting the quality of welding in FSW. Dimensions of FSW tool pin and shoulder with different tool geometries have an influential role in FSW by which adequate heat input and uniform material mixing can be performed [40]. Akinlabi et al. [41] studied the effect of shoulder dimension (15 mm, 18 mm, and 25 mm) on FSW between 5754 aluminium alloy (AA) and C11000 copper (Cu) with a constant tool pin diameter of 5 mm. The rotational speeds were 600, 950, and 1200 rpm and feed rates were 50, 150, and 300 mm/min respectively. They found that more pronounced mixture layers were produced by 15 mm and 18 mm diameter than 25 mm due to material flow by 25 mm was improper, and also joint efficiency was highest by the weld produced at 950 rpm and 50 mm/min with the 18mm shoulder diameter. Vicker microhardness was lower in SZ for 25 mm dia. than 15 mm and 18 mm due to lower deformation in SZ region.

Zhou et al. [42] studied the effect of featureless pin, threaded pin, and threaded pin with flutes on microstructure and mechanical properties for 1060 friction stir spot welding (FSSW) of 1060 aluminium alloy and T2 copper. The study shows threaded pin generates higher heat and temperature during welding. Tensile shear load largely depends on the pin profile and the highest tensile shear load is achieved by threaded pin. This is caused by a large stir zone area with proper IMC layer thickness (not too thick) at the interface due to proper stirring.

Muthu et al. [43] also examined whorl pin profile, plain taper pin profile, and taper threaded pin profile, on FSW of AA1100 H14 and commercially pure copper. They found that hardness variation was same in all pin profiles. However, a plain taper pin profile results in better tensile strength as distribution of fine Cu particles which form a composite-like structure at nugget and also lower IMCs content.

Galvao et al. [44] investigated the effect of tool geometries on deoxidized copper (copper-DHP) and identified that tool geometries significantly impact material mixing. Scrolled shoulder tools offered the best material flow and grain refinement compared to flat or conical designs, resulting in improved mechanical properties.

Galvao et al. [45] also examined influence of shoulder geometries on material flow and IMC formation on friction stir butt-welding of oxygen-free copper with high phosphorous content to

5083-H111 aluminium alloy. They found that the scrolled tool formed a tongue-shaped mixing region almost entirely composed of Al_2Cu. However, the conical tool formed aluminium, copper, Al_2Cu, and Al_4Cu_9mixtures with higher heterogeneity. They also observed that shoulder geometry plays a significant role in bead surface finish as irregularly distributed IMC-rich material with non-metallic solid characteristics was observed on welded surfaces produced by the conical tools. However, the welds produced by scrolled tool depicted a regular surface with insignificant amounts of IMCs.

Mehta et al. [46][47] studied the effect of various tool pin designs for the joining of ETP Cu and AA T651. They have found polygonal tools and taper tools are undesirable for aluminium copper dissimilar butt welding. Polygonal tools produce defects in the stir zone due to uneven scratching of Cu, whereas the taper pin profile is unable to mix material uniformly. However, the cylindrical pin profile shows defect-free dissimilar joints and good material mixing, showing maximum tensile strength at the joint.

Sharma et al.[48] Investigated different pin profiles for FSW of AA5754 Al alloy to commercially pure copper. Investigation revealed that the square pin profile exhibits better quality joint and microhardness than other pin profiles of cylindrical, taper, cylindrical cam, and taper cam. The study revealed that the Square tool pin provides good pulsating action in the region between the in-circle and the circum-circle of the square pin profile. The combined result of pulsation and stirring produces better material.

Beygi et al. [49] demonstrated the influence of pin geometries (threaded cylindrical, threaded conical, pyramidal) on bi-metals of Pure commercial copper and aluminium AA1050 and showed that pins that have a higher area of contact have a higher torque with a higher quantity of material plasticized around the pin. A threaded conical pin provides the highest tensile strength and fewest defects. This is because of adequate downward material flow, and no defect forms on advancing side by threaded conical tool.

Kah et al. [50] compared effect of IMCs on Al 1060 with pure Cu joints by laser welding, friction stir welding, and brazing. They observed that same intermetallics compound was found in both fusion welding and solid-state welding. However, the distinctiveness IMCs differs according to the position of the phase formed.

2.4 Weld Quality Analysis Through Real-Time Monitoring

Weld quality can be checked directly by visual inspection, and radiographic and ultrasonic testing, but indirect techniques like real-time monitoring can significantly reduce productivity loss. Hence real-time monitoring of different forces and torque signals can be a viable option [51][52]. Researchers used different sensors to measure the torque, forces, and other factors to find a correlation between process parameters and defect formation. Trimble et. al [53] examined forces generated during FSW of AA2024-T3 by rotating component dynamometer and also develeoped a 3D model of the process for predicting the tool forces. They have observed that maximum chance of damage of tool pin during plunge force and maximum chance of damage of shoulder during the translational stage. The developed model was also capable of identifying tooling designs which can more efficiently process the workpiece material.

Kumar et al. [54] analyzed the force signals on friction stir welding of AA1100 aluminium alloys to identify defect. They have used DWT to decompose the signals into detail signals and approx signals. They have observed that abrupt changes in features like square of error of detail signals present in vertical forces detect the defect in the welding joints.

Das et.al [55] identified the tunnel defect on friction stir welded AA1100 alloy by analyzing the force signals through combined wavelet packet transform and hilbert –huang transform and defective welding was found when the frequency spectra of the signal were in higher frequency bands than the signal of defect-free welding. they have also developed a machine learning based support vector regression model to predict ultimate tensile strength.

Das et al. [56] developed a low-cost setup to measure force and torque andalso developed support vector regression-based model by AI for correctly measuring joint strength from acquired force signals using DWT. A statistical indicator was projected based on co-relation with the statistical features of signals, which showed a significant correlation with the joints' UTS.

Das et al. [57] also proposed a new indicator combining the torque signal's statistical features (dispersion, asymmetry, and excess) for defect identification. They have also demonstrated and compared two machine learning-based models to predict UTS. The model with only signal features outperformed the model with signal features and process parameters.

Das et al. [58] also tried determining weld quality from two different ANN models by feeding features from current signals from the main spindle and feed motor by wavelet packet transform along with process parameters. They found that the multi-layer-fee-forward neural network model is more predictive than the radial-basis neural network model. They also demonstrated a new energy-to-entropy ratio of the signal to find out the best mother wavelet functions to decompose wavelet packets.

Roy et al. [59] introduced a novel approach by utilizing the time-frequency analysis of force and power signals through DWT (Discrete Wavelet transform) for continuous defect detection in FSW of commercially pure AA1100. Study of weld CT scans further strengthened the defect detection validation. Identifying internal and external defects was made possible by detecting abrupt changes in the square of error of details coefficients. Notably, their research revealed the superiority of power signal data over force signal data.

Rabi et al. [60] analyzed vibration signals using DWT and continuous wavelet transform during friction stir welding to identify and measure tunnel defects. Statistical parameters like kurtosis, standard deviation, mean, and crest factor have been extracted for defect validation from defect-free welds.

Researchers also found that the emission of acoustic signals has a vital role in FSW process monitoring. Zeng et al. [61] studied tool condition monitoring of friction stir welding of 6061 alumnium alloy by acoustic emission signals. They observed different distinguished features of microstructures as tool wear increased and showed that AE hits concentrated on the higher amplitudes with increasing tool wear. The results show that AE sensing provides a potentially effective method for monitoring tool wear online.

Subramanium et al. [62] monitored tensile strength through an acoustic emission approach for different tool pin profiles on AA6063-T6 alloys and found AE hits better correlate with tensile properties. They have also found that due to faster pulsating action, square pin provides better strength than cylindrical and triangular pins.

Chen et al. [63] applied a wavelet transform to the acoustic emission signals of 6061 Al alloy friction stir welding. They observed that band energy changes when the tool traverses over a defective region can predict the defects' existence, location, and size.

Boldsaikhan et al. [64] found the wormhole defect by applying a discrete Fourier transform and artificial neural network to the acquired force signals. They related the oscillations of the feedback forces to the plasticized material flow so that the frequency spectra of the feedback forces could be used to detect wormhole defects.

Yang et al. [65] developed an algorithm to monitor the gap between the two plates during the FSW of AA 2024 alloy. They compared the plunge forces signal during FSW, where a gap was known not to exist.

2.5 Objectives of Present Work

The present work aims to analyze the tool geometries for joining AA1100 and commercially pure copper for varying weld parameters. The variations in tool geometry have an effect on material flow, heat input, and force and torque generation. These changes have a significant effect on metallurgical as well as mechanical properties. This review helps to identify key research gaps in the understanding of the process-microstructure-property relationships in FSW, which form the basis for the following objectives.

1. To successfully join AA1100 and commercially pure for varying weld parameters and tool geometries.
2. To study the effect of different tool geometries for varying weld parameters on heat input, material flow at nugget.
3. To analyze the influence of different tool geometries for varying weld parameter on mechanical properties.
4. To study the effect of formation of IMCs and effect on interfacial layer for varying weld parameters and tool geometries.
5. To correlate the effect of force and torque signals with metallurgical properties as well as mechanical properties.
6. To obtain a suitable tool geometry within a specified range of process parameters.

Chapter3:

Materials, Experimental Methods and Computation Techniques

3.1 Introduction

In the present investigation, FSW was conducted to join the 1100 aluminium alloy and commercially pure copper. All the experiments were conducted by positioning copper on advancing side (AS) and Al on retreating side (RS) for sound welding, as copper is harder than aluminium [8][23]. Experiments were performed on a 3.0-ton FSW machine. The FSW machine was shown in Fig. 3.1 and installed at Workshop, Mechanical Engineering Department, NIT Agartala. The detailed specifications of the machine are available in Table 3.1. All the sequences of operations of the present investigation have been shown as a flow chart in Fig. 3.2

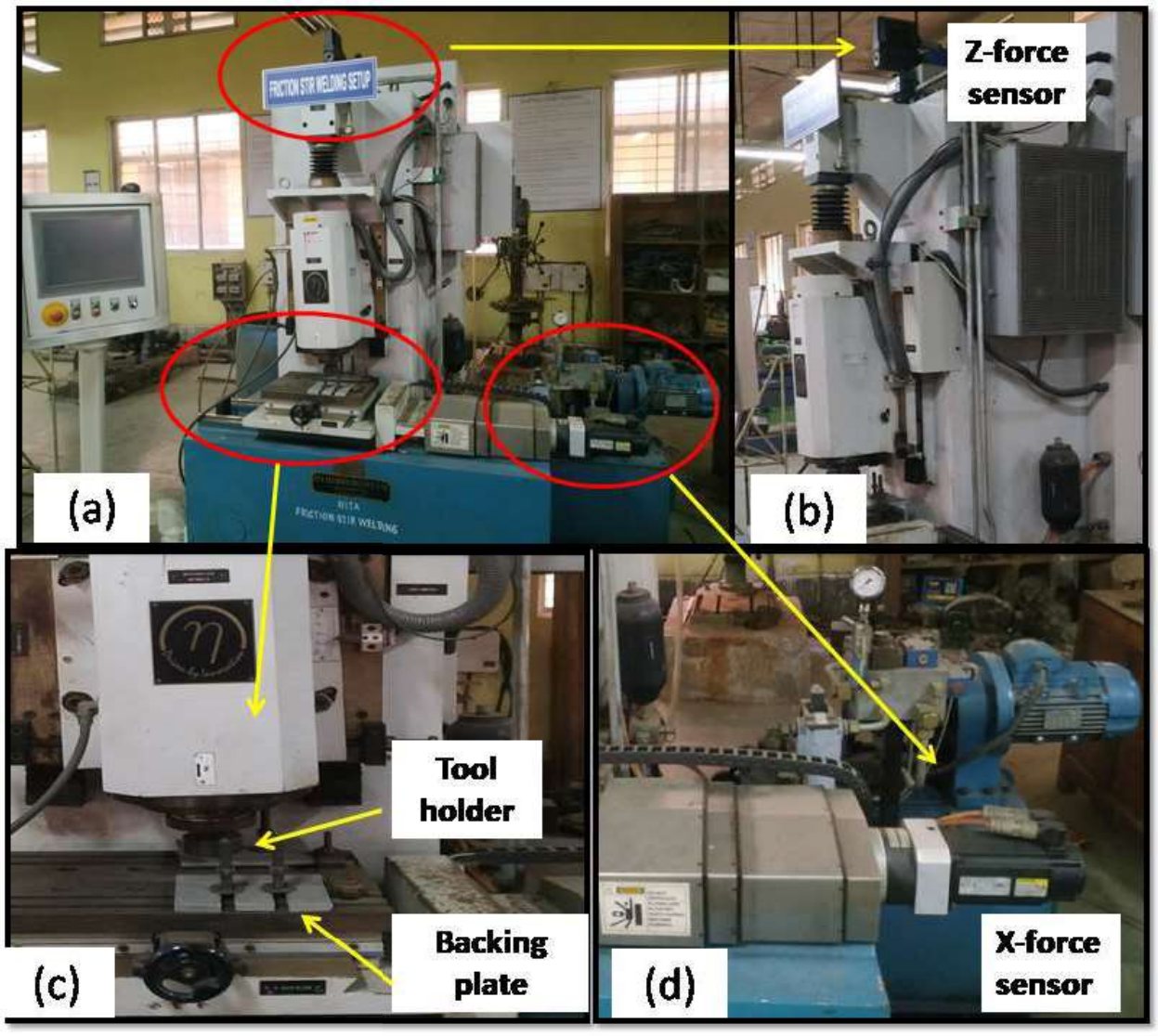

Fig. 3.1 3.0-ton FSW machine with a capacity of 30-kN axial thrust.

Table 3.1 Specifications of FSW machine.

Machine	3Ton Friction Stir Welding Units
Stir welding operations	Linear welding
Spindle speed	3000 RPM Max. –infinity variable
Spindle torque – rated	86.4 Nm @ 1650 rpm
Tool force (axial load on spindle)	30 KN
Spindle Tilting	± 10˚
Height of Table from floor level	900 mm
Table clamping area	400 mm x 275 mm
Machine weight	~2500 Kg
Machine Dimension (Width × Depth× Height)	2260 mm × 1600 mm × 1915 mm
AXIS TRAVEL	
X-Axis	400 mm
Y-Axis	50 mm
Z-Axis-(spindle slide)	100 mm
Feed rate(X-Axis)	1000mm/min. Max.
AXIS THRUST	
X-Axis	10 KN
Z-Axis	30kN Max.
Thrust feed back	Through load cell
AXIS MOVEMENT	
X-Axis	Servo motor-3000 rpm, 5 N-m
Y-Axis	Manual positioning and clamping
Z-Axis	drive Servo hydraulic cylinder
HYDRAULICS	
Hydraulic tank capacity	110 Litres
Hydraulic oil	ISO 68
Total connected load	60 Amps
Electric power supply	3 AC, 400 V, 50 Hz.

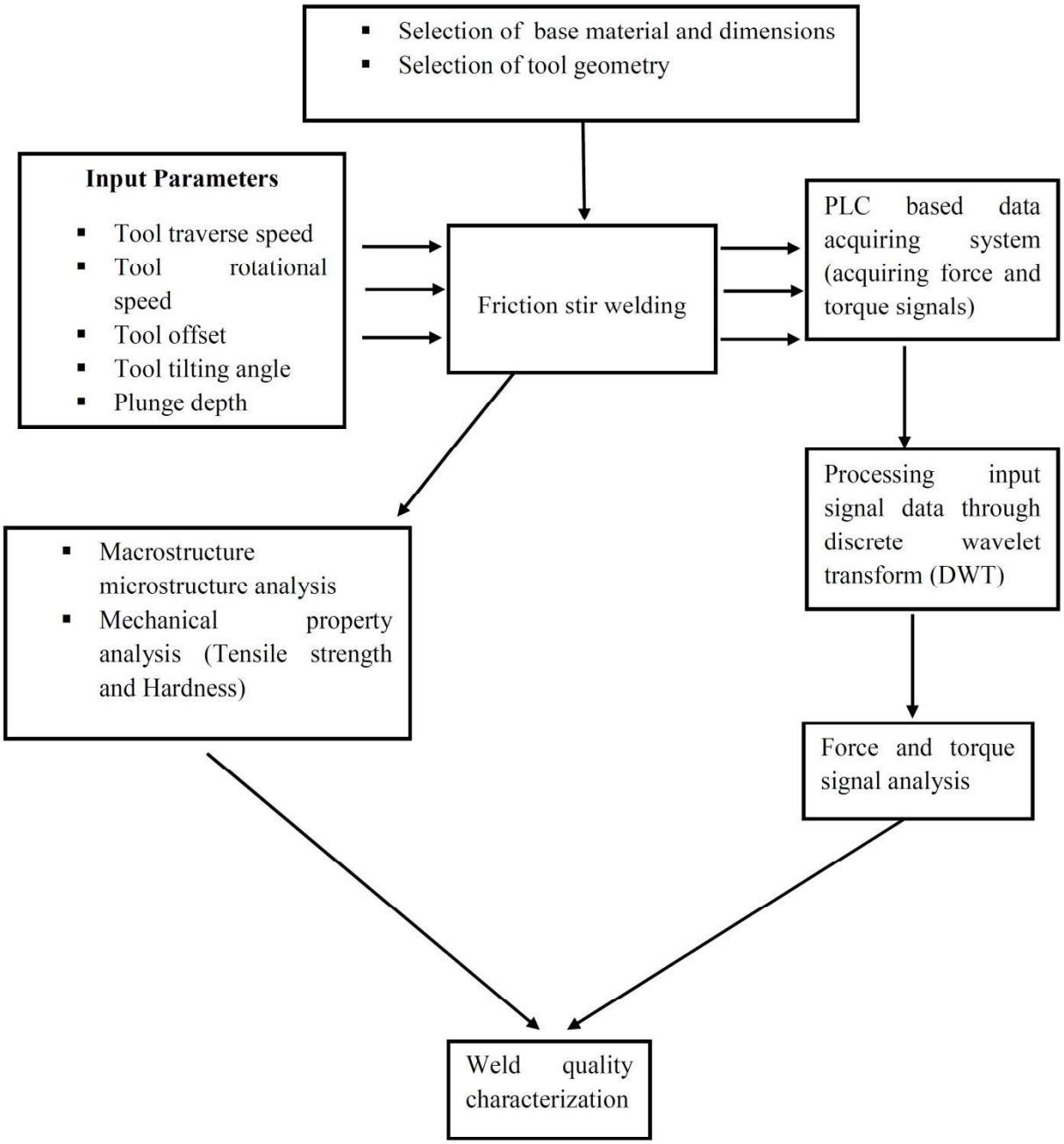

Fig. 3.2 Flow chart of the present investigation

3.2 Selection of Base Material and Plate Preparation

1100 aluminium alloy and commercially pure copper plates of 3 mm thickness have been selected as base materials for the present study. Plates have been prepared for welding according

to the size of 85 mm, ×65 mm, and ×3 mm by power saw and universal milling machine. The composition of base materials are given in Table 3.2 and 3.3.

Table3.2 Chemical compositions (wt.%) of 1100 alumnium alloy

Material	Al	Cu	Fe	Si	Zn
1100 alumnium	99.10	0.10	0.40	0.30	0.10

Table 3.3 Chemical compositions (wt.%) of commercially pure (99%) copper

Material	Cu	Si	Fe	Al	Zn	Ni	Pb
Commercially pure Copper	99.97	0.006	0.004	0.001	0.009	0.004	0.006

3.3 Selection of Tool Material

In the present investigation, H13 tool steel is used as a tool material. As briefed in the literature review, H13 tool steel is widely used for joining aluminium and copper. The advantages of using H13 tool steel as a tool material is that it has good resistance to thermal softening, high hardenability, high strength, and high toughness. The chemical compositions of H13 tool steel are shown in Table 3.4.

Table 3.4 Chemical composition of H13 tool steel

Material	C	Cr	Fe	Mo	Si	V
Percentage (wt%)	0.32-4	5.13-5.25	90.9	1.33-1.4	1	1

3.4 Selection of Tool Geometries

Present investigations have been carried out using two different tools having two different pin geometries. In between two tools, one tool consists of a cylindrical threaded pin and is referred to as SCT. The other tool have a regular hexagonal prism tool pin and this tool is referred to as the

SH tool. However, both tools have the same concave shoulder having diameter was 16 mm and 6° angle of concavity. The tool pin length of both tools is 2.75 mm. The SCT tool has a pin diameter of 5.2 mm and having 90° Right hand 'V' Thread 1 mm pitch. SH tool also has an inscribed diameter of 5.2 mm for the tool pin. The selection of tool pin geometries is based on their ability to enhance material flow. The SCT tool facilitates localized material flow multiple times before depositing it behind the tool, which enhances material stirring, promotes void closure, and helps break down oxides. In contrast, the SH tool operates with a pulsating action due to its flat surfaces, which act like cutting edges of a cutter. Material is trapped in these flats and released behind the tool, resulting in efficient mixing. Additionally flats are shown to increase the temperature and nugget area [17][47][48].The actual image of the respective tool is presented in Fig. 3.3. Manufacturer's tool design is presented in Fig. 3.4 and 3.5

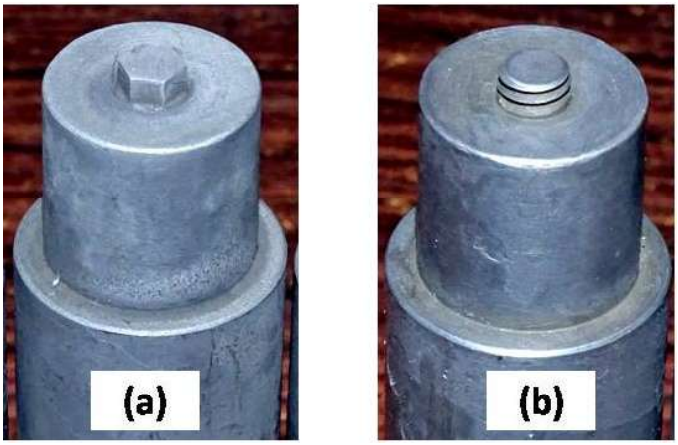

Fig. 3.3 (a) straight hexagonal (SH) (b) straight cylindrical threaded (SCT)

3.5 Selection of Process Parameters

The present investigation was conducted with to examine the effect of tool pin geometries on weld quality in terms of the microstructure and mechanical properties of friction stir welded 1100 aluminium alloy to commercially pure copper for different process parameters. All the parameters set are considered from trial and error and machine capacity. In the present study, each experiment carried out with one parameter varies at a time. Rotational speed and traverse speed have been selected as process parameters for this study. Two different sets of experiments have been carried out for each tool. In one set of experiments, rotational speed was fixed at 1000

rpm, and traverse speed was changed in four levels from 1.2 mm/s to 2.1 mm/s with an interval of 0.3 mm/s (Table 3.4). Then, in another set of experiments, the traverse speed was fixed at 1.5 mm/s, and the rotational speed was varied at 800 rpm, 1200 rpm, and 1400 rpm (Table 3.4). Thus, 14 experiments were performed using the two tools.The tool tilt angle has been set at 2° to the normal surfaces of the welded material. The Tool pin offset was 1.5 mm to the aluminium side. Since copper is harder than aluminium, it is positioned on the advancing side during welding, which allows better heat generation on the advancing side and facilitates better Cu diffusion [23][66].

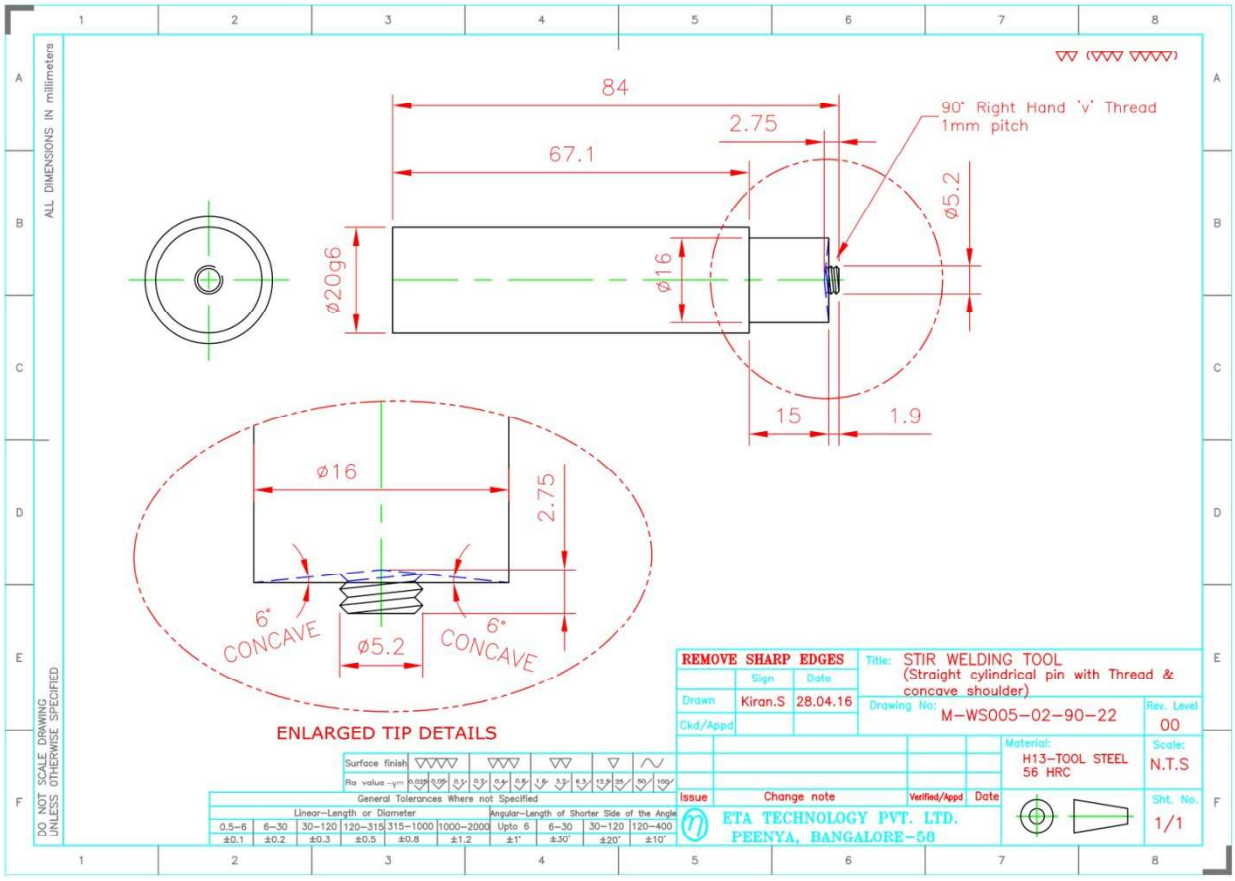

Fig. 3.4: Manufacturer design of SCT tool

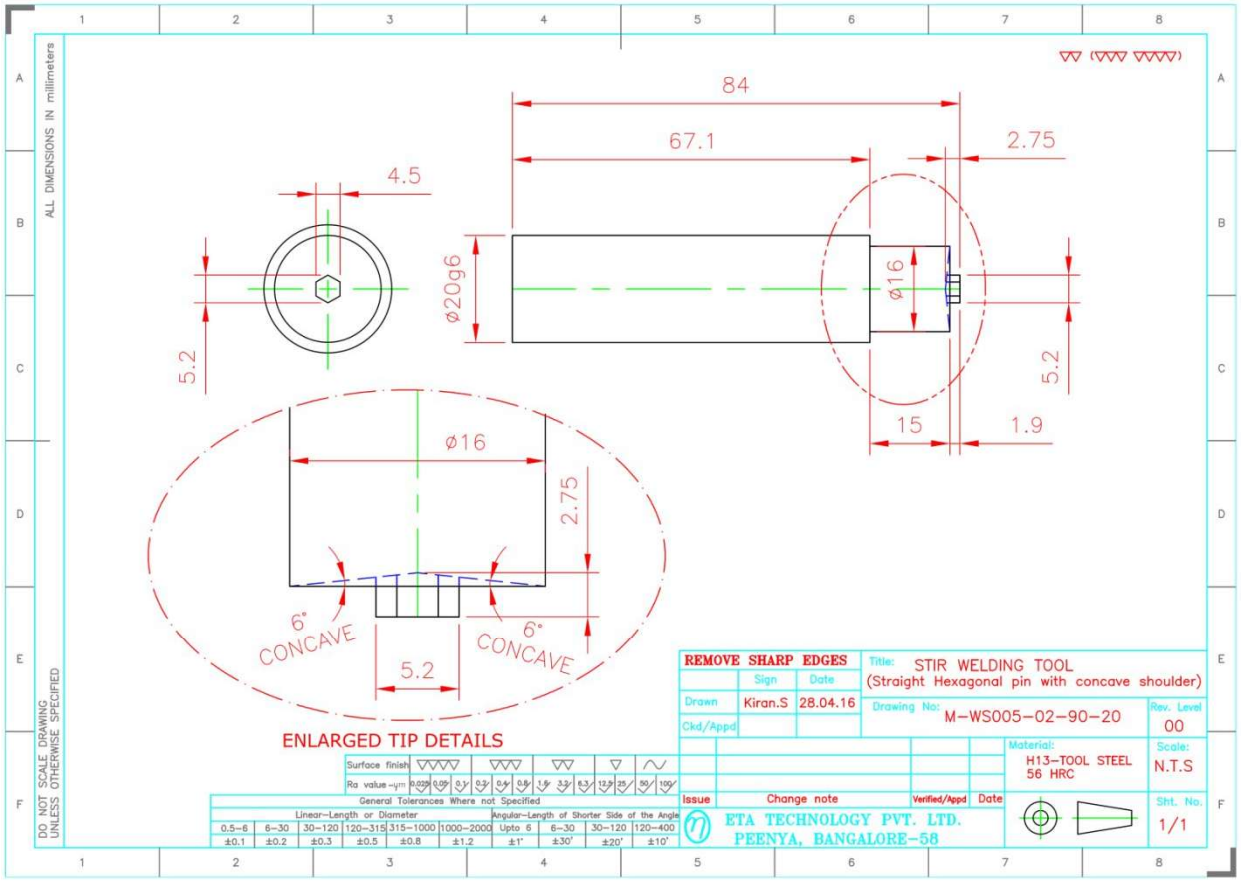

Fig. 3.5 Manufacturer design of SH tool

3.6 Experimental Measurement of Torque and Forces

Two Strain gauge-based load cells were employed to measure different forces and spindle torque. One is attached at the spindle head (5 ton) for Z-force and spindle torque detection, and the other is set to the auxiliary slide for X-force measurement. Load cells are connected to the PLC system and equipped with Lab View software for data acquisition. The data acquisition interval is set to 0.1 sec, which is found to be adequate. The machine is operated in constant Z-axis position mode. The obtained data from machine were by using 'Origin' plotting software. The plots that are obtained show the relationship between torque and Z-force with time. The variation so obtained is called distribution, and later on, average values are evaluated by considering the mean value.

Table 3.5 Design of experiments

Experiment no.	Rotational speed (rpm)	Traverse speed (mm/s)
1	1000	1.2
2	1000	1.5
3	1000	1.8
4	1000	2.1
5	800	1.5
6	1200	1.5
7	1400	1.5

3.7 Estimation of Heat Input during Welding

Heat input for all the welding is evaluated using equations (3.1) and (3.2)

$$P = \frac{2\pi\omega T_s}{60} \quad (3.1)$$

$$H = \eta \times \frac{P}{f} \quad (3.2)$$

where,

P= weld power (watt)

ω=Tool rotational speed (rpm),

T_s=Spindle torque (N-m)

H= heat input (J/mm)

f = traverse speed of tool (mm/min)

η = Efficiency factor, and it varies from 0.9 to 1, and here it was taken as 0.9[67].

3.8 Post Weld Analysis

3.8.1 Metallographic Analysis

The welded specimens have been cut from the workpiece into 30 mm × 3mm × 6 mm (Fig. 3.6) from the welding cross-section using a wire-cut electro-discharge machine. After cutting the samples, cold mounting was done to the samples (Fig. 3.7) using epoxy resins for proper gripping. Then, the specimens were grinding by grinding sequences of 180, 240, 400, and 600 mesh grit sizes. After that, the samples were polished using emery papers from 1000 grades to 3000 grades. After every stage of polishing, samples were cleaned with running water and then dried by a hand dryer. The final polishing involved using diamond paste (grade 3, 1, 0.25) with HI-FIN fluid on selvyt cloth for 15 minutes to obtain a flat scratch-free surface by disk polisher, LECO CORPORATION,SPECTYRUM SYSTEM^{TM} 1000, USA (Fig. 3.8). After polishing, the surface became a mirror finish. Then, the samples were cleaned with running water and dried with a hand dryer. The aluminium side was etched by modified Keller's solution having 190 ml of distilled water, 5 ml of HNO_3, 3 ml of HCL, and 3 ml of HF, whereas for the Copper side, a solution of 5 g $FeCl_3$, 50 ml HCL and 100 ml H_2O has been used.

Fig. 3.6 Metallographic analysis specimen

Fig. 3.7 Metallographic analysis specimen with cold mounting

Fig. 3.8 Disk polisher for specimen polishing

Fig. 3.9 Stereo microscope

Macrostructure examinations were done using a stereo microscope ZEISS Stemi 508, Germany (Fig. 3.9). Microstructure examinations were conducted using a light optical microscope OLYMPUS BX53M, JAPAN (Fig. 3.10). A SEM-EDX study was conducted using a field emission scanning electron microscope ZEISS SUPRA 40, Germany (Fig. 3.11) in the Metallurgical & Materials Engineering Department at IIT Kharagpur, West Bengal.

Fig. 3.10 Light optical microscope

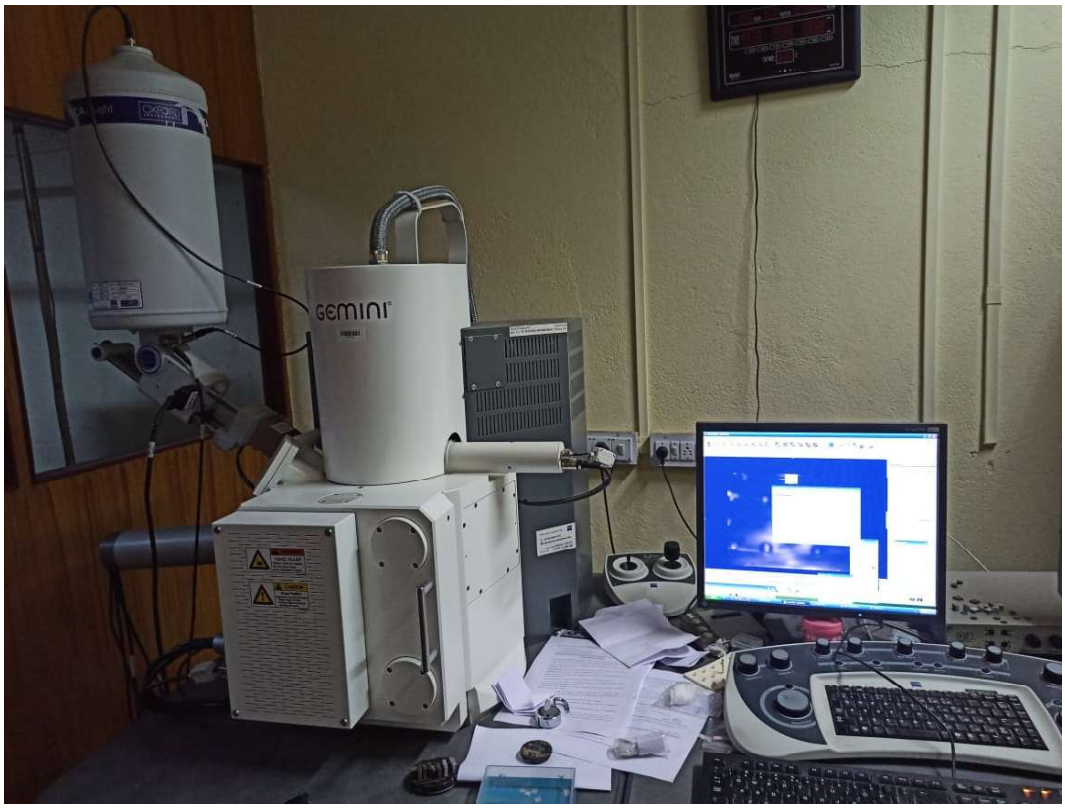

Fig. 3.11 Field emission scanning electron microscope

3.8.2 Tensile Test

Tensile tests were carried out to measure ultimate strength (UTS), yield strength (YS) and percentage of elongation at a constant strain rate of$1\times10^{-3}s^{-1}$**.** Tensile specimens (Fig. 3.12) were prepared as per ASTM E8 sub-size specimen (Fig. 3.13). Tensile test was performed on Tinius OlsenUTM-H50KS, UK the Metallurgical & Materials Engineering Department at IIT Kharagpur (Fig. 3.14).

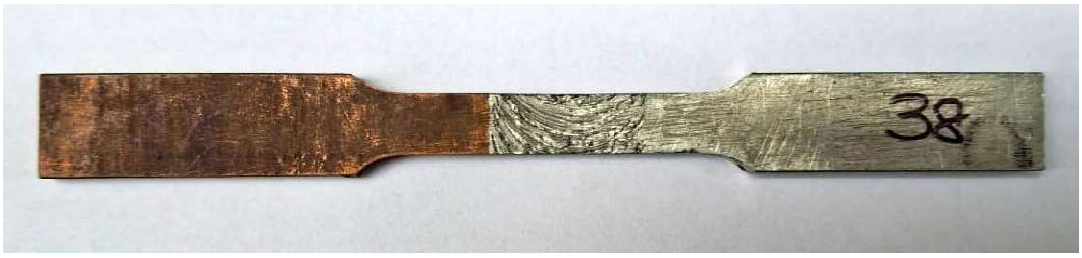

Fig. 3.12 Tensile specimen

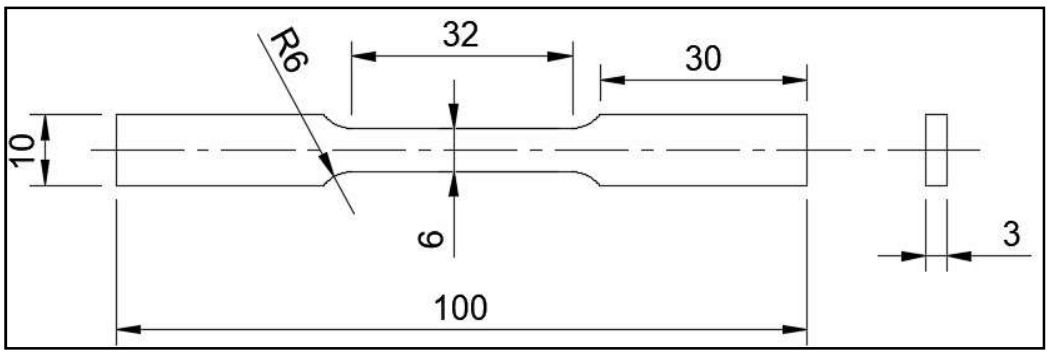

Fig. 3.13 Tensile Specimen as per ASTM E8 standard (all dimensions are in mm)

Fig. 3.14 Universal testing machine

Fig. 3.15 Micro hardness tester machine

3.8.3 Microhardness Test

Regular hardness tests can be too rough for delicate materials. Microhardness testing provides a precise way to assess the resistance to wear and tear in minute samples, intricate shapes, specific material zones, and even thin surface layers. Micro-hardness testing provides precise, accurate

information for material having fine microstructures. In the present investigation, microhardness tests have been performed on Micro Hardness Tester-VMH-002V, Walter UHL, Germany (Fig. 3.15) at a load of 100 gf after every 1 mm indentation with a dwell time of the 20s.

3.8.4 Force and Torque Signal Analysis

Spindle torque and Z-force distribution during welding with respect to time is considered here as signal and discrete wavelet transformation (DWT) is used here for filtering purpose of those signal (Spindle torque and Z-force) as Fourier Transform (FT) is not useful in the present study as the signals are non stationary and FT is failed portray the localization of frequency components. FT only shows the frequency components in the respective signal. Techniques such as the Discrete-Time Fourier Transform (DTFT), Discrete Fourier Transform (DFT), and Fast Fourier Transform (FFT) serve as techniques for analyzing of discrete time signals. However, these transformations are mainly applicable to stationary signals. In contrast, time-domain analysis enables us to identify specific frequencies at any moment. Discrete wavelet transform analyzes a non-stationary signal in a two-dimensional space of timescale. DWT employs long time intervals to generate more precise low-frequency information and shorter regions for high-frequency information. In DWT, the signal in consideration is passed through high-pass and low-pass filters. The high-pass filters generate detailed coefficients, whereas the low-pass filters give approximate coefficients [54]. Several mother wavelet functions are available as filters and for selecting one among these a proper procedure needs to be incorporated for best data extraction as mentioned below.

For a selected mother wavelet function, the wavelet coefficients of discrete child wavelet are computed by shifting and scaling the mother wavelet function (Eq. (3.3)) [57].

$$\psi(t) = \frac{1}{\sqrt{2^j}}\psi\left(\frac{t-k.2^j}{2^j}\right) \tag{3.3}$$

where ψ(t) represents the mother wavelet function, j, and k are scale and shift parameters, respectively. Then, the wavelet coefficient (ϒ) can be expressed in the following manner (Eq. (3.4)) [57], where S(t) denotes the input signal. The wavelet coefficient evaluated here is the convoluted form of the original signal with dilated, reflected, and normalized mother wavelet, sampled at points 1, 2^j, 2^{2j},……., 2^{Nj}(for a signal of length N).

$$\Upsilon = \int_{-\infty}^{\infty} S(t) \frac{1}{\sqrt{2^j}} \psi\left(\frac{t-k.2^j}{2^j}\right) dt \quad (3.4)$$

3.8.4.1 Optimum Level of Signal Decomposition

Decomposition of signals has been performed using the DWT tool of MATLAB 2016a software package. The selection of optimum level of decomposition has been chosen according to minimum entropy criteria.

a. The decomposition of the signal proceeds to the next level when parent wavelet packets yield an entropy value less than the total entropy values of the decomposed packet.
b. In violation of the above condition, the respective level will be considered the optimum level for decomposition.

Shannon entropy has been considered for selecting the optimum level of signal decomposition (Eq. 3.5). The optimum level of signal decomposition is set to the 5^{th} level for both spindle torque and Z-force according to the decomposition rule.

$$E(S) = -\sum_{i=1}^{N} {S_i}^2 \log ({S_i}^2) \quad (3.5)$$

where E(S) is the Shannon entropy of the signal S (decomposed signal), and S_i is the i^{th} value of the signal [58].

3.8.4.2 Method for Finding the Best Mother Wavelet Function and Corresponding Level

For selecting the best mother wavelet and their corresponding level for the spindle torque and Z-force highest tensile strength among all the welding considering both the tool has been selected. Accordingly, it has been split into detail and approximate signals for multiple levels with available mother wavelet functions (Coiflet, Daubechies, Symlet). Then the optimum level of decomposition for mother wavelet functions has been found using minimum entropy criteria. Now best mother wavelet function has been selected from the ratio of the energy of the original signal to the entropy of the decomposed wavelet packet using the selected mother wavelet functions. Accordingly, the particular mother wavelet function which gives maximum energy to entropy ratio is selected as the best mother wavelet function.

Chapter 4:

Effect of Tool Geometries on Weld Quality of Al-Cu Dissimilar Joint for Varying Traverse Speed

4.1 Introduction

This chapter presents the effect of different pin geometries on varying traverse speeds for 1100 aluminium alloy (Al) to commercially pure copper (Cu). The investigation includes studying heat input during welding, weld bead surface morphology, material flow, formation of IMCs at the interface and stir zone, and the mechanical properties of the joints in terms of tensile strength and microhardness. For this investigation, experiments were conducted with a fixed tool rotational speed of 1000 rpm, while the tool traverse speed was varied from 1.2 mm/s to 2.1 mm/s at intervals of 0.3 mm/s.

4.2 Effect of Tool Pin Geometries on Heat Input at Different Traverse Speeds

Figure 4.1 show the variation in heat input for at different traverse speed for different tool geometries. It was observed that at 1.2 mm/s rpm heat input for SH tool (786.18 J/mm) was much higher than SCT tool (525.95 J/mm). This may happen due to slip happening at the tool work interface for SCT tool. It was also observed when the tool traverse speed increases to 1.5 mm/s, the heat input in case of SCT tool (516.21J/mm) is almost the same but for SH tool

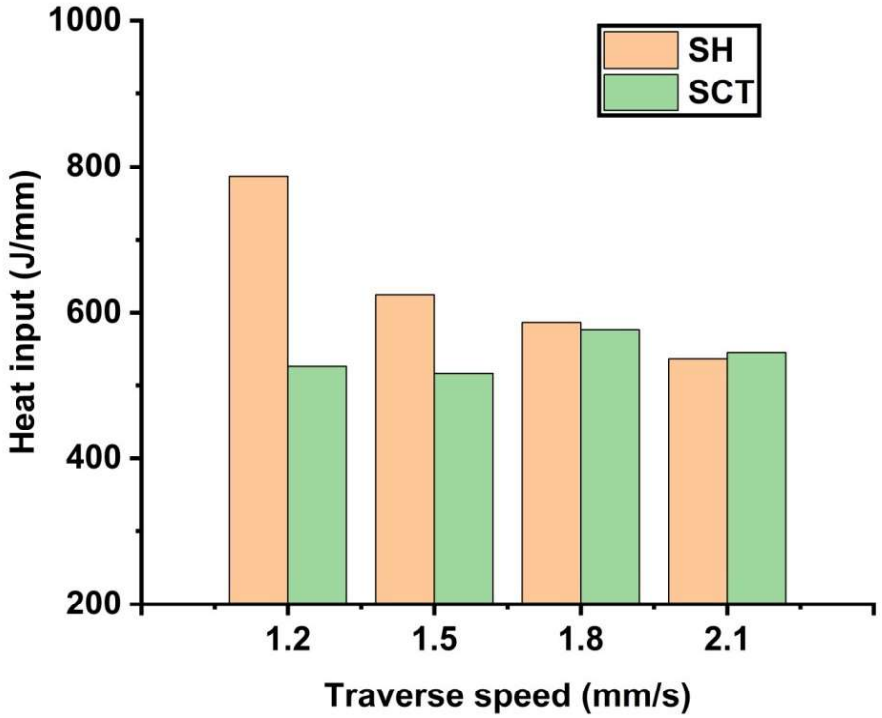

Fig. 4.1 Heat input at different traverse speeds for SH and SCT tool

(624.23 J/mm) it decreases drastically. It can assumed that at 1.5 mm/s, slip phenomenon influences friction as well as deformation which reduces the heat input of SH tool drastically as heat input depends on the amount of friction and deformation. At 1.8 mm/s heat input for SH tool (586.66 J/mm) decreases and for SCT tool (576. 71 J/mm) it increases and found that both tools have almost the same amount of heat input which signifies that at this combination of rotational speed and traverse speed (1000 rpm and 1.8 mm/s), the geometry of both tools plays an insignificant role in heat input. At 2.1 mm/s both tools have also almost the same amount of heat input. But both tools have decreased heat input (SH- 536.04 J/mm and SCT- 544.56 J/mm) which may be due to very little tool-workpiece contact time for frictional and deformation heating and also may be slip phenomenon increase for both the tools at the tool-workpiece interface which reduces the heat input.

4.3 Effect of Tool Geometries on Welded Surfaces at Different Traverse Speeds

Figure 4.2 shows welded surfaces at different tool traverse speeds for different tool geometries. From Fig. 4.2 it has been observed that for lower traverse speed excess hot flash occurred at edges for SH tool for higher heat generation [46][68] which has already been marked in Fig. 4.2a. At lower traverse speeds material flow beneath the tool shoulder was bad because of uneven distribution of materials may be due to slipping. Slipping occurs due to unbalanced heating and insufficient downward plunge-force for which, two materials having different material properties, results in improper mixing in stir zone and also over the weld surfaces. Improper mixing of two different materials having different flow stress results in sometime defects (cluster of voids) which have already been marked in the above Fig. 4.2(e) [69][70]. Tool traverse speed at 1.8 mm/sec for both tools shows better surface appearance. This may be due to a combination of traverse speed and rotational speed providing optimum heat generation as well as stirring. It has been also observed that as tool traverse speed increases the circular flow pattern over the weld bead surface decreases as the slipping torque of material decreases and also at higher traverse speed due to higher sticking torque, the materials struggle to flow over the weld surface [71] which is seen at 2.1 mm/s for SCT tool (Fig. 4.2h).

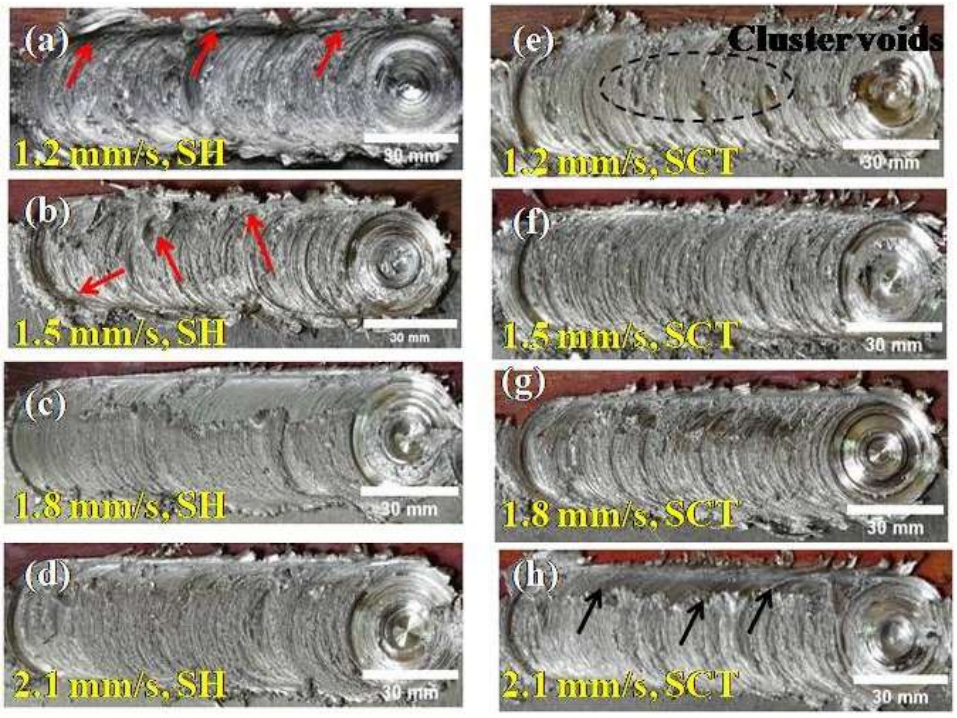

Fig. 4.2 Welded surface at different tool traverse speeds for different tool geometries

4.4 Effect on Weld Formation for Different Tool Geometries at Different Tool Traverse Speeds

Microstructure can be one of the attributes for judging weld quality. Figure 4.3 shows the detailed microstructure of welded joints for SH tool. At a low traverse speed of 1.2 mm/s, heat input was higher due to the contact time between the tool and workpiece was higher and shows a lamella structure at stir zone[25] along with Cu bulks. When the traverse speed increases to 1.5 mm/s, heat input reduces drastically may be due to slip at the tool-workpiece interface which causes bad material mixing at stir zone with bulk Cu insertion in the stir zone and also no proper flow pattern observed. But when the traverse speed increased to 1.8 mm/s an optimum heating condition was achieved which resulted in metal proper softening and deformation into fine Cu particles at stir zone. Similarly, when traverse speeds increase 2.1 mm/s, also better material mixing of Cu into Al was observed due to proper the heat input and stirring action at 2.1 mm/s.

Figure 4.4 shows a microstructure examination of the SCT tool for different tool traverse speeds. 1.2 mm/s for SCT tool a reverse phenomenon has been observed than SH tool. It was already

discussed that at 1.2 mm/s for SCT tool reduction in heat input may be due to the slipping phenomenon which reduces the friction and deformation by the tool resulted in improper material mixing at stir zone with bulk Cu insertion to the Al [68]. It is also found that improper mixing at stir zone results defects like voids for 1.2 mm/s shown in Fig. 4.4b, c.

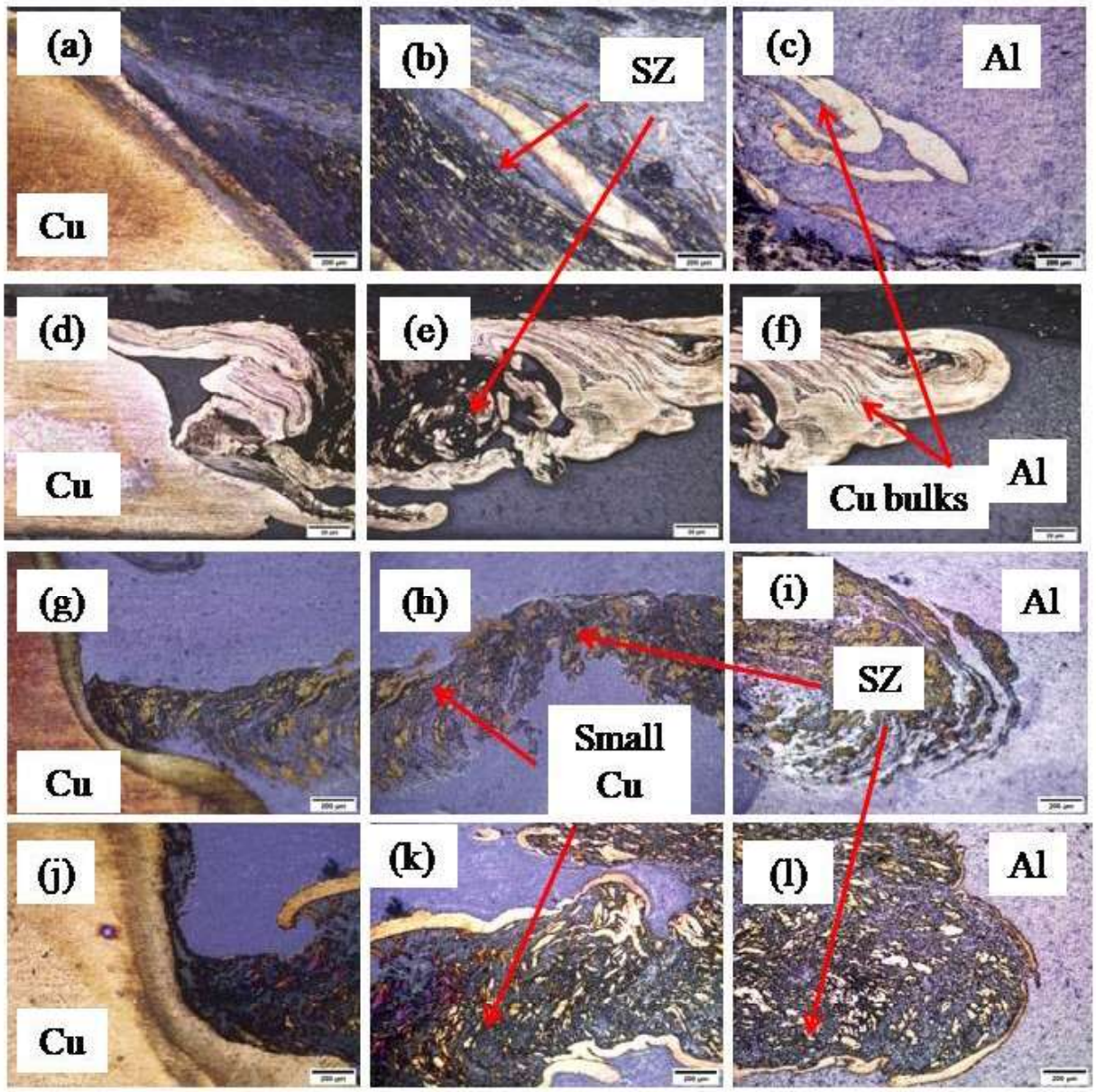

Fig. 4.3 Microstructure of different stir zone at 1.2 mm/s (a, b, c), 1.5 mm/s (d, e, f), 1.8 mm/s (g, h, i) and at 2.1 mm/s (j, k, l) of traverse speed of SH tool

Again at 1.5 mm/s of traverse speed, bulk Cu insertion at stir zone was found as at 1.5 mm/s heat input is also low may be due to some slipping phenomena. Due to low heat input SCT tool

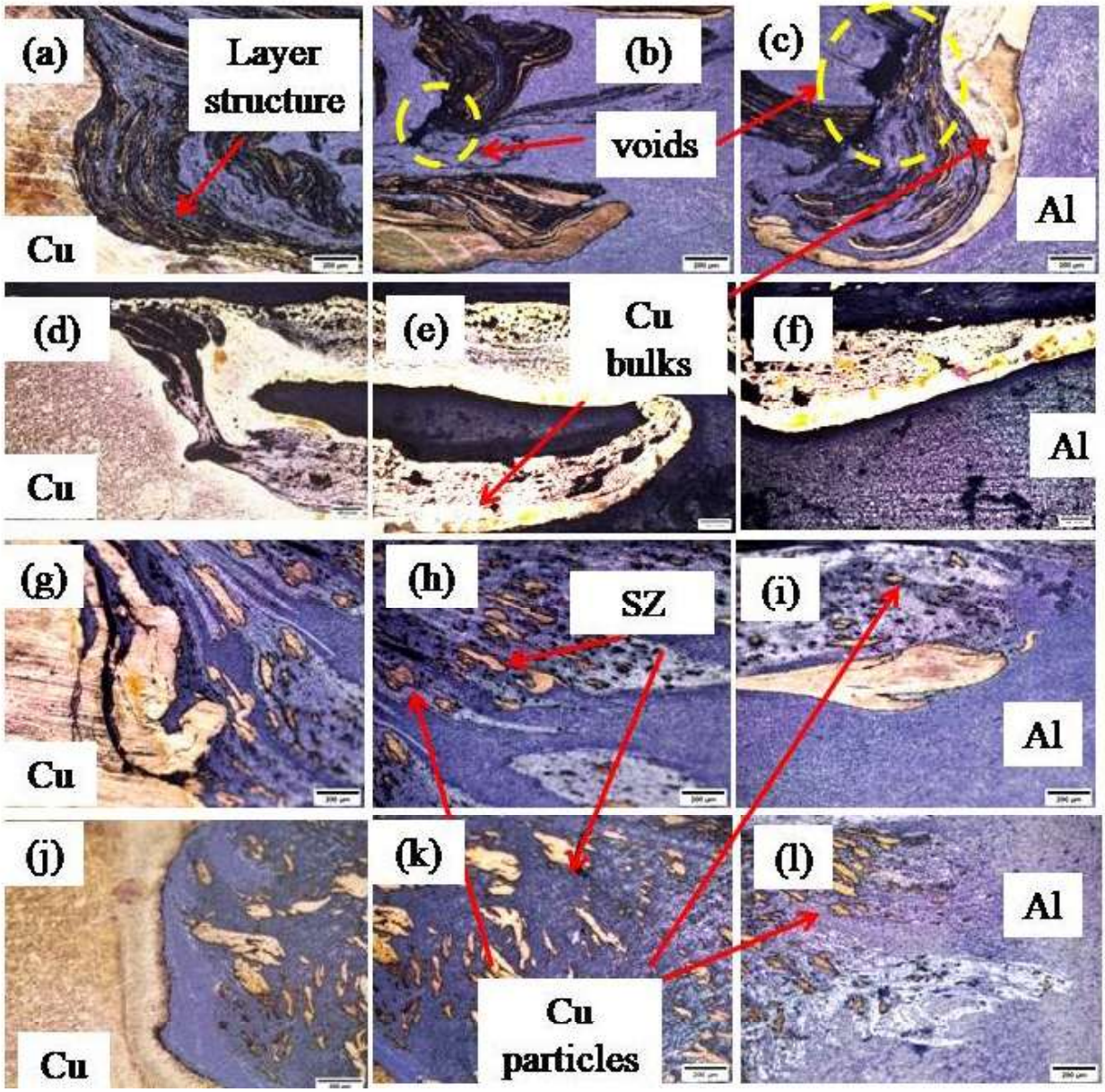

Fig. 4.4 Microstructure of different stir zones at 1.2 mm/s (a, b, c), 1.5 mm/s (d, e, f), 1.8 mm/s (g, h, i) and at 2.1 mm/s (j, k, l) of traverse speed of SCT tool

unable to deform the large Cu into small particles. At 1.8 mm/s speeds SCT tool also shows better mixing as small to medium Cu particles are distributed in the stir zone may be due to good amount heating and stirring action by the tool. At 2.1 mm/s heat input for SCT tool also gives shows better material deformation like 1.8 mm/s of traverse speed as relatively small Cu particles were visible at stir zone. Comparing the material deformation for both the tools from

Figs. 4.3 and 4.4, it was observed that that SH tool shows more uniform deformation of Cu at stir zone than SCT tool due to pulsating stirring action of lateral flat surfaces of tool pin [48].

4.5 Effect on Microstructure for Different Tool Geometries at Different Tool Traverse Speeds

SEM-EDS analysis have been carried out to detect probable phases of hard and brittle intermetallic compounds, at joint that formed due to Cu particles mixed with Al, based on atomic ratio analysis from EDS. These large intermetallics are formed due to excessive heat generation and unusual plastic deformation during welding which may affect weld quality by reducing the strength of welding [26][39][47]. Spectrum EDS was performed to analysis probable phases of intermetallics at marked regions of SEM in Fig. 4.5, Fig. 4.6, Fig. 4.7 and Fig. 4.8. SEM image 4.5a also shows fine distribution of Cu particles in stir zone for SH tool at 1.8 mm/s. Further EDS analysis has been carried out at marked regions (4.5b, c) of Fig. 4.5a shows probable formation phases in S1 and S2 are Cu+ Al_4Cu_9[72][73] and Al_4Cu_9 [72] at interface of Al-Cu and at stir zone S3 and S4 are$Al_4Cu_9$and Al+Al_2Cu [74][75]. Figure 4.6a also shows the good amount of mixing at stir zone by SH tool at 2.1 mm/s. EDS analysis of Fig. 4.6b, suggest formation of Al +Al_2Cu at S1 and S2 whereas S3 and S4 represents Al_2Cu [72][74] and Al+Al_2Cu of Fig. 4.6c. SEM images of Fig.4.5 and 4.6 also depict that the fine distribution of Cu particles in stir zone for SH tool due to adequate heating as well as pulsating stirring action by SH tool which causes uniform distribution of intermetallics and also decreases formation of large amount of intermetallics compounds[25][39][48]. EDS analysis of marked area (Fig. 4.7b, c) of Fig. 4.7a suggests that solid solution of Al are found in S1 and S3 and Al+Al_2Cu at S3 and S4. From Fig.4.7 it was observed that small elongated Cu particles at stir zone which presents good amount mixing at 1.8 mm/s for SCT tool due to adequate heating and stirring action. Fig. 4.8a it also some lamella structure near Al-Cu interface but the improper mixing predominant at stir zone with Cu bulks and spectrum EDS of Fig. 4.8b and c, shows the presence of intermetallics Al_4Cu_9, AlCu, Al_2Cu and Al_2Cu_3 [28][37] in the welding zone at points S1, S2, S3 and S4.This improper material flow caused uneven distribution of intermetallics and also may be formed large intermetallics formation is very detrimental for joint strength.

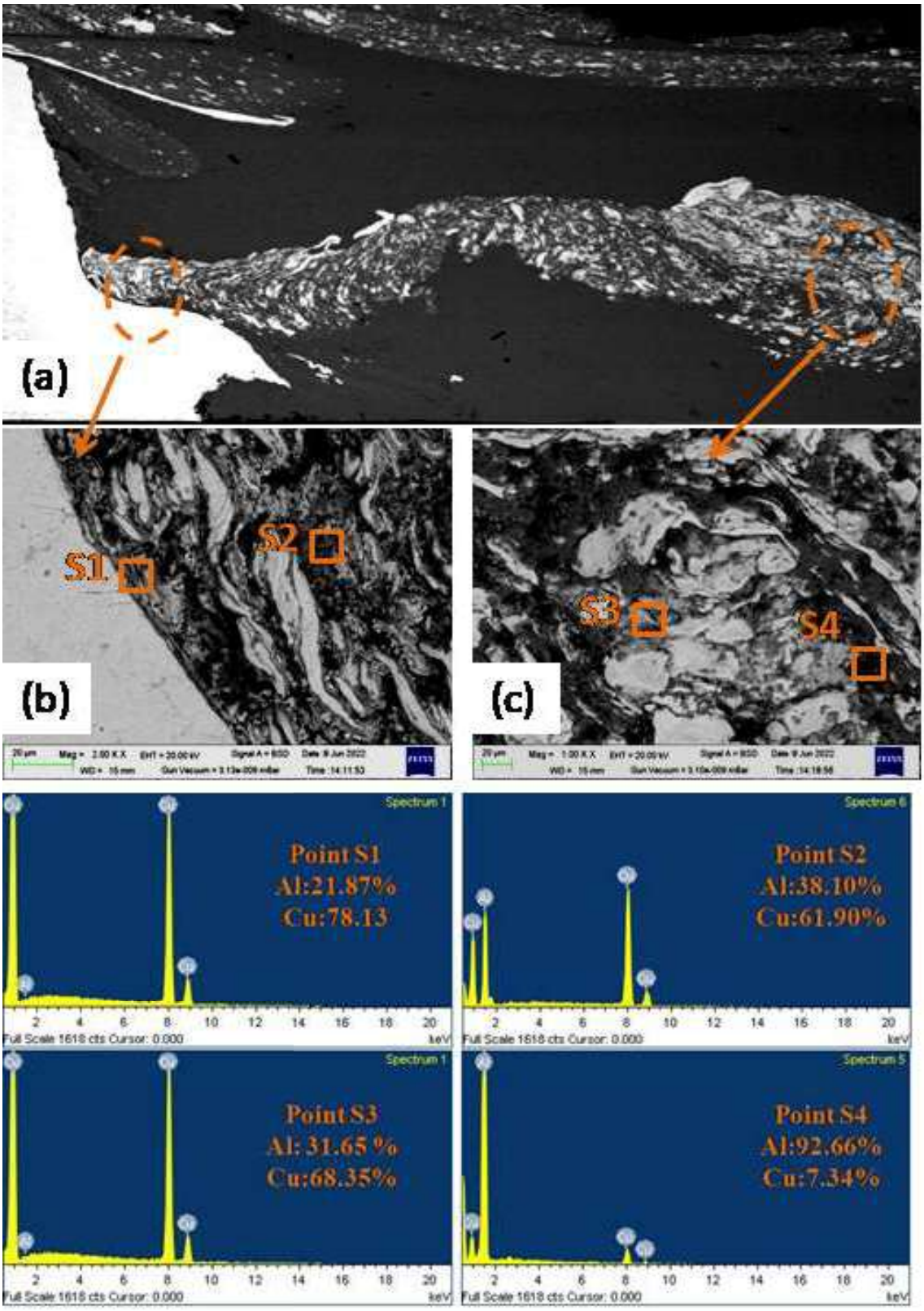

Fig. 4.5 SEM and EDS analysis at 1.8 mm/s for SH tool

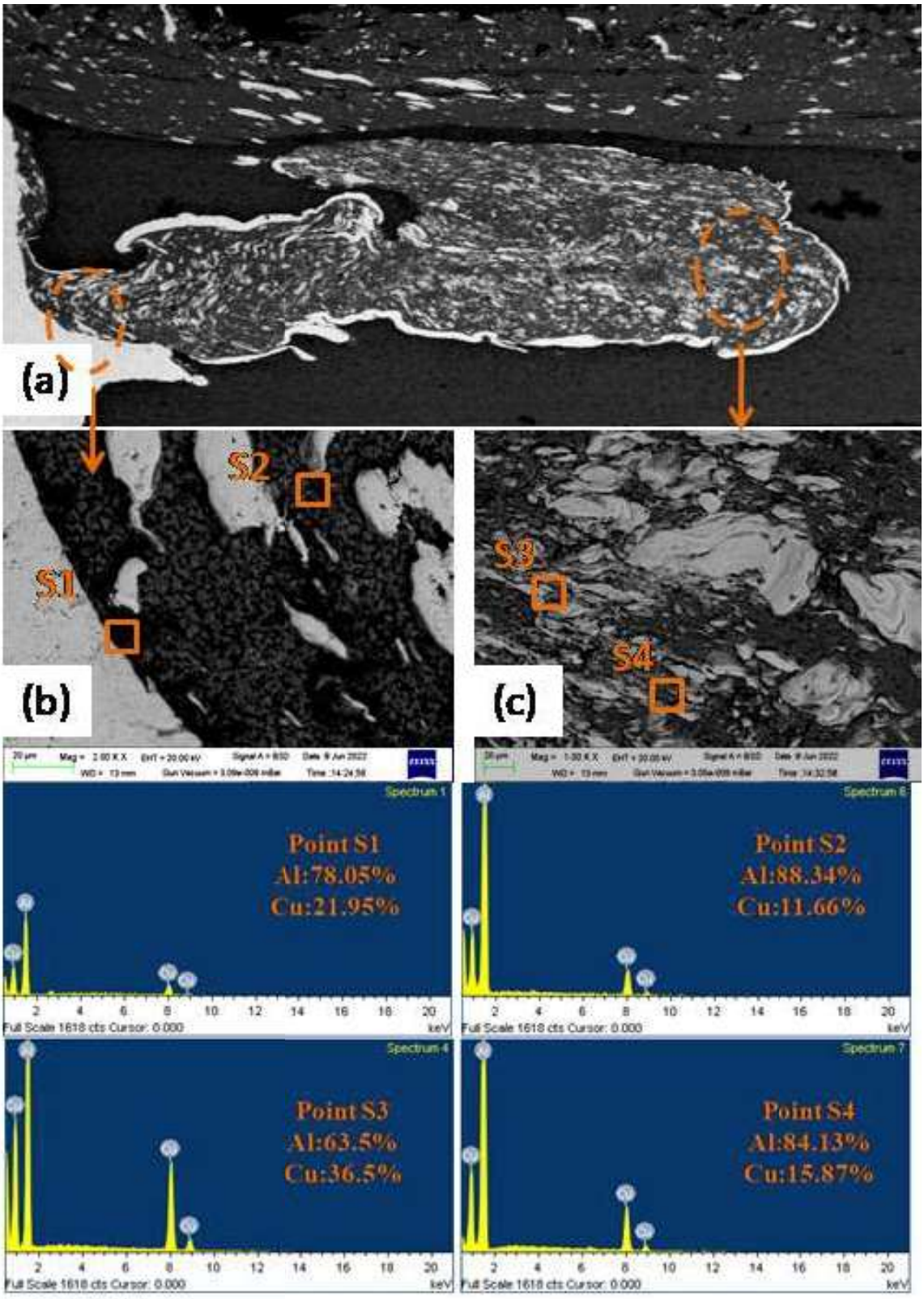

Fig. 4.6 SEM and EDS analysis at 2.1 mm/s for SH tool

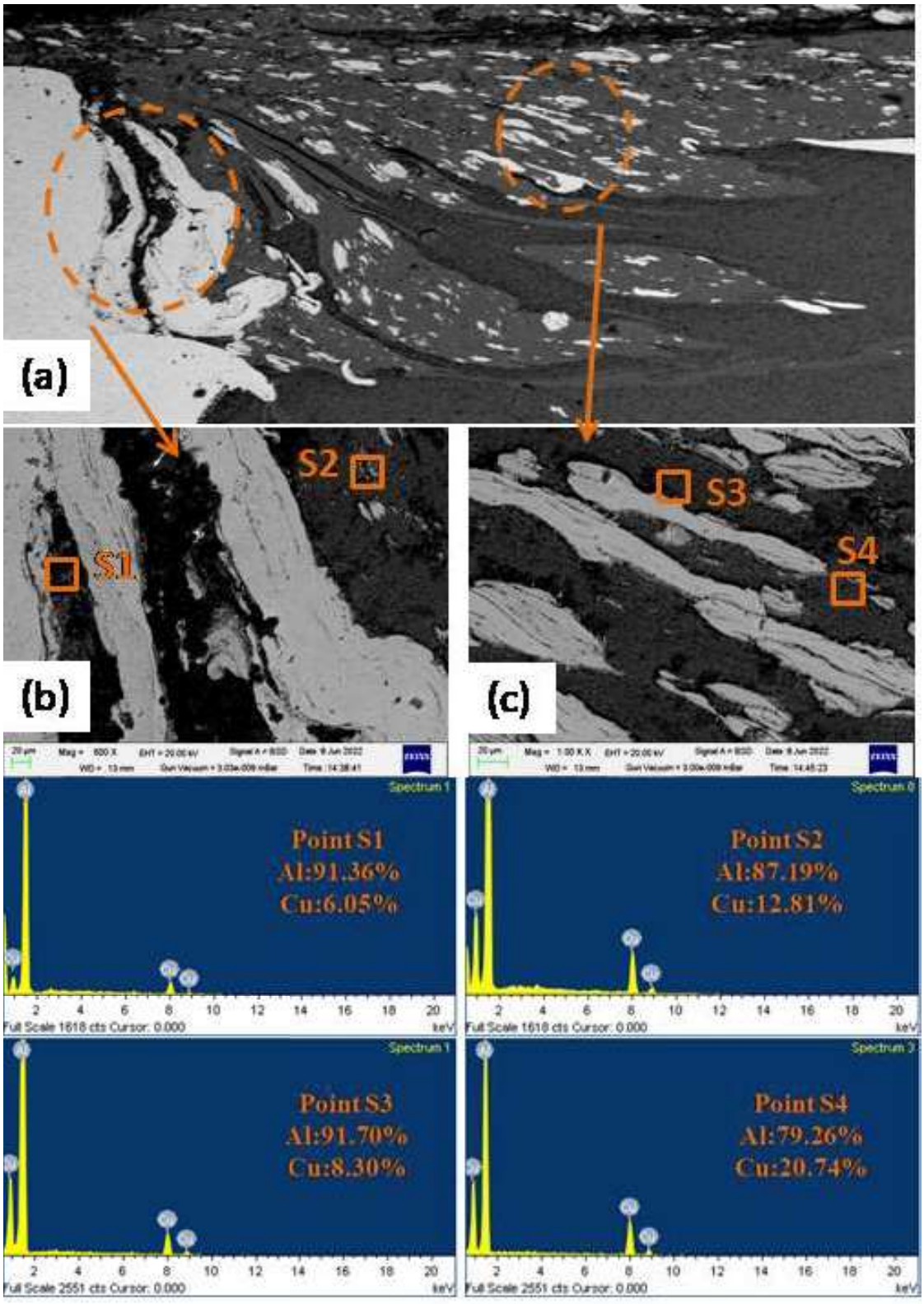

Fig. 4.7 SEM and EDS analysis at 1.8 mm/s for SCT tool

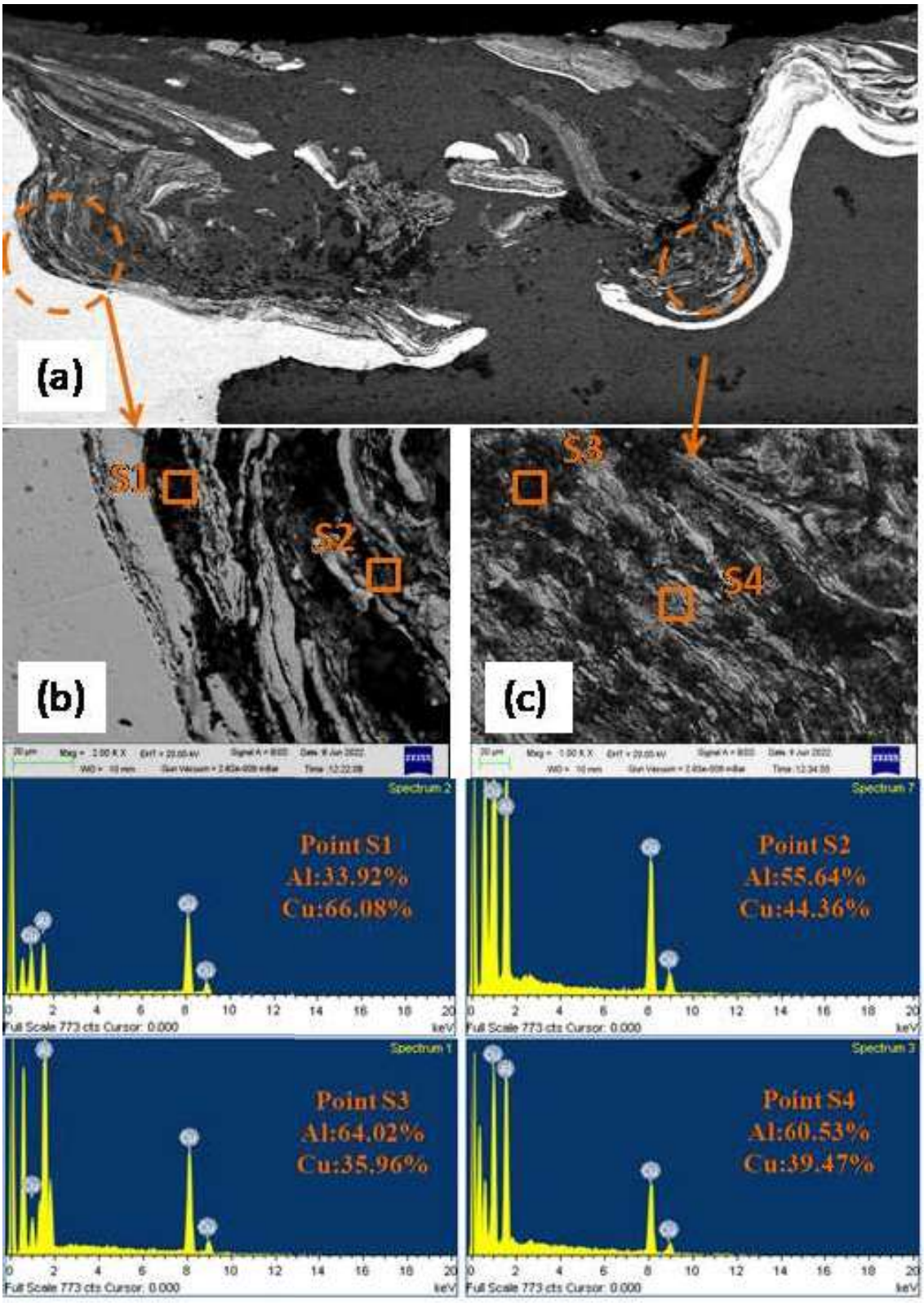

Fig. 4.8 SEM and EDS analysis at 1.2 mm/s for SCT tool

4.6 Effect on Tensile properties and Fractography

Figure 4.9 shows UTS at different traverse speeds for different tools. At 1.2 mm/s, SH tool shows better tensile strength (81.4 MPa) due to present of lamella structure. UTS lowest at 1.2 mm/s for SCT tool (30.1 MPa) comparing SH tool. This drastic reduction in tensile strength is due to material flow defect occurred at stir zone due to improper mixing which caused tool slipping phenomena. Fig4.10a shows failure occurred for SH tool at stir zone for 1.2 mm/s and only cleavage facets were observed in Fig. 4.10b and c. This represents brittle failure occurred at the joint. Fig. 4.11aalso shows the failure also occurred at stir zone for SCT tool at 1.2 mm/sand Cleavage facet also were observed in Fig. 4.11b and c which supports that failure was brittle in nature. The average UTS (SH- 76.7 MPa and SCT- 65.1 MPa) were found for both the tool at 1.5 mm/s. It is due to the large Cu insertion at stir zone results less mixing and reduced bond strength for both the tools. Fig. 4.10d also depicts that joints at 1.5mm/s for SH tool failed stir zone with mix mode of failure in nature as dimple, tear ridges (4.10e) and cleavage facet (4.10f) were observed at fractured surfaces. For SCT tool at 1.5 mm/s the mix mode of facture occurred at stir zone (4.11d) as dimple, tear ridges and cleavage (4.11f) were observed at fractured surfaces. When traverse speed increases to 1.8 mm/s both the tool shows improved tensile strength (SH-93.4 MPa and SCT-80.2 MPa) due better bond strength. It was due adequate heat input and uniform mixing by both the tool. SH tool shows highest tensile strength at 1.8 mm/s. Distribution of fine Cu particles at stir zone due pulsating stirring action of the tool causes better dispersion strengthening effect which increases joint strength. For SH tool at 1.8 mm/s, mixed mode of failure at interface (Fig. 4.10g) where fractography studies show cleavage facet (Fig. 4.10i) and dimples (4.10h) at failed location. For SCT tool also mixed mode of failure occurred at failure region (Fig. 4.11g) where dimples (Fig. 4.11h) and cleavage facet (Fig. 4.11i) were observed and failure was at Al side TMAZ region. Again, traverse speed increases to 2.1 mm/s interfering time between tool and materials has been reduced further which reduces heat generation and stirring time also. This results less material bonding and reduces the joint strength (SH-71.7 MPa and SCT-72.6 MPa) for both the tool. Figure 4.10j shows failure propagated from stir zone to Al side TMAZ. fractography analysis shows cleavage facet (Fig. 4.10k) and dimples (4.10l) were observed at fractured location which states that mix mode of failure occurred at the

joint for SH tool at 2.1 mm/s. Figure 4.11 (j, k and l) shows that the brittle failure occurred at stir zone and cleavage facet have been seen at fracture surfaces for SCT tool at 2.1 mm/s.

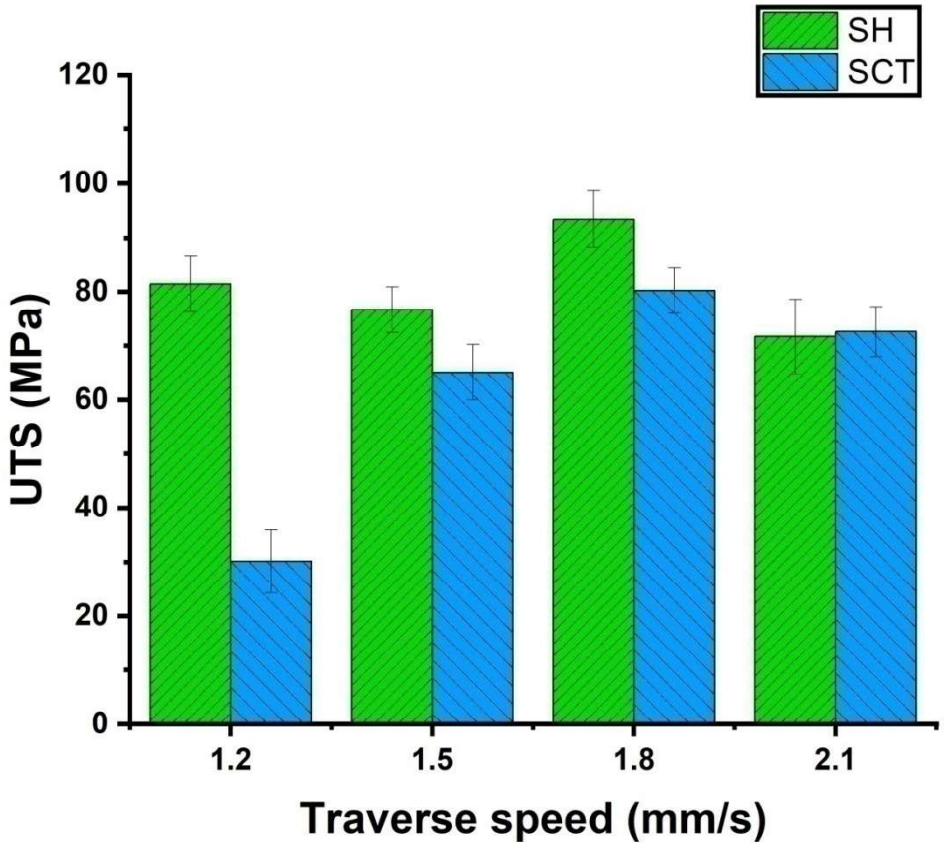

Fig. 4.9 UTS at different traverse speeds for different tools

4.7 Effect on Hardness for Different Tool Pin Geometries at Different Tool Traverse Speeds

Figure 4.12 illustrates the microhardness distribution at weld zone for both tools. Generally, higher hardness has been observed in stir zone because of hard and brittle IMCs formation as well as intense plastic deformation and grain refinement[28][76]. At 1.2 mm/s , formation of lamella structure at stir zone results sudden increase in hardness at stir zone for SH tool with a maximum value of 178HV whereas for SCT tool improper mixing causes formation of large intermetallics at stir zone which increases the hardness nugget for SCT tool with a maximum value of 280 HV. At 1.5 mm/s, hardness for SH tool (maximum-232 HV) increased may be due

to formation large intermetallics for insertion of large Cu particle at stir zone [39], whereas for SCT tool at 1.5 mm/s, hardness is highest among all(maximum-381 HV). It is also due to large insertion of Cu and less material deformation causes large intermetallics and also solid solution hardening in the rest stir zone increases hardness [39][46][77]. At 1.8 mm/s, both tools have small

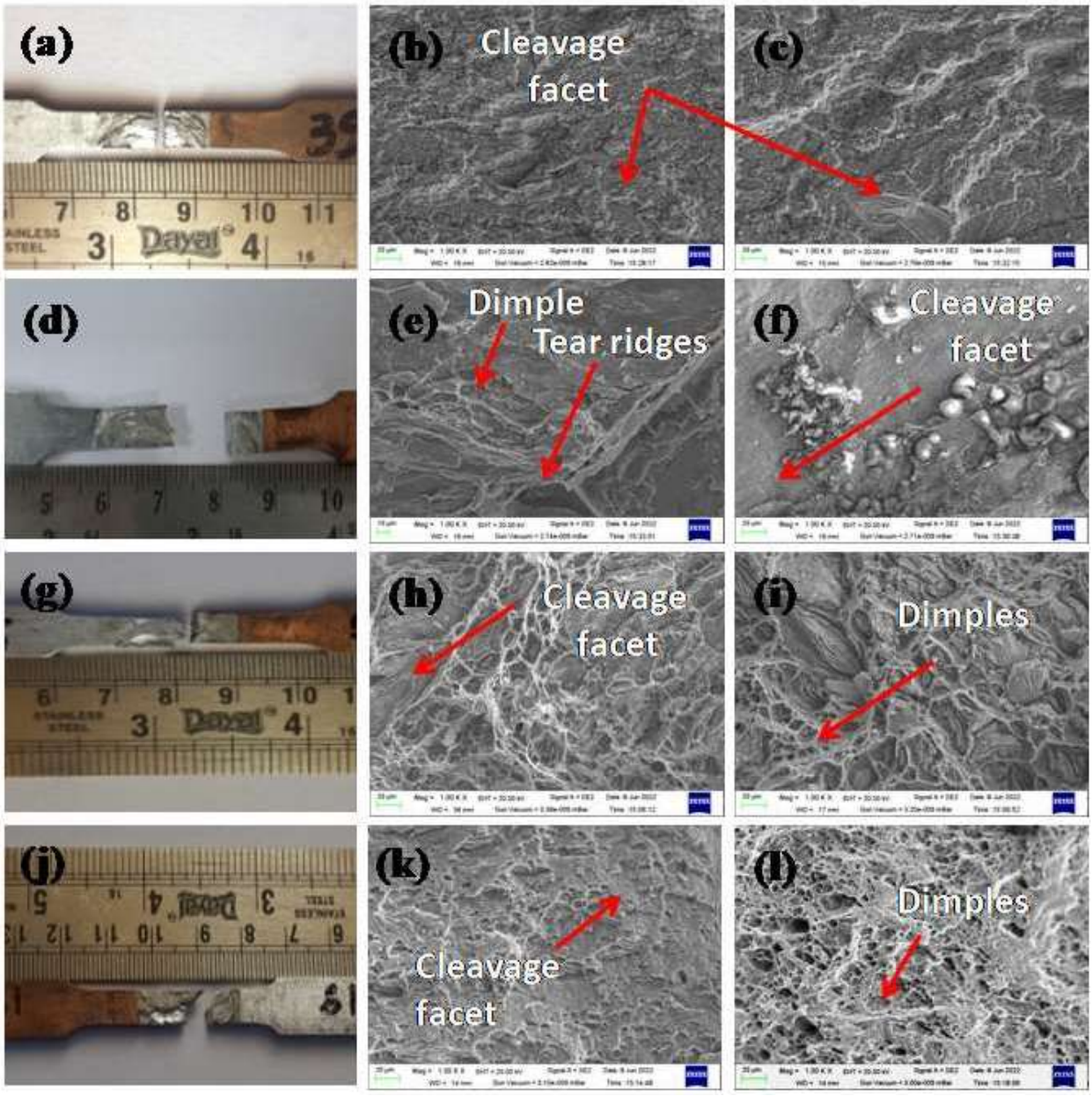

Fig. 4.10 Failure location with fractured surfaces of SH tool at 1.2 mm/s (a, b and c), 1.5 mm/s (d, e and f), 1.8 mm/s (g, h and i) and 2.1 mm/s (j, k and l)

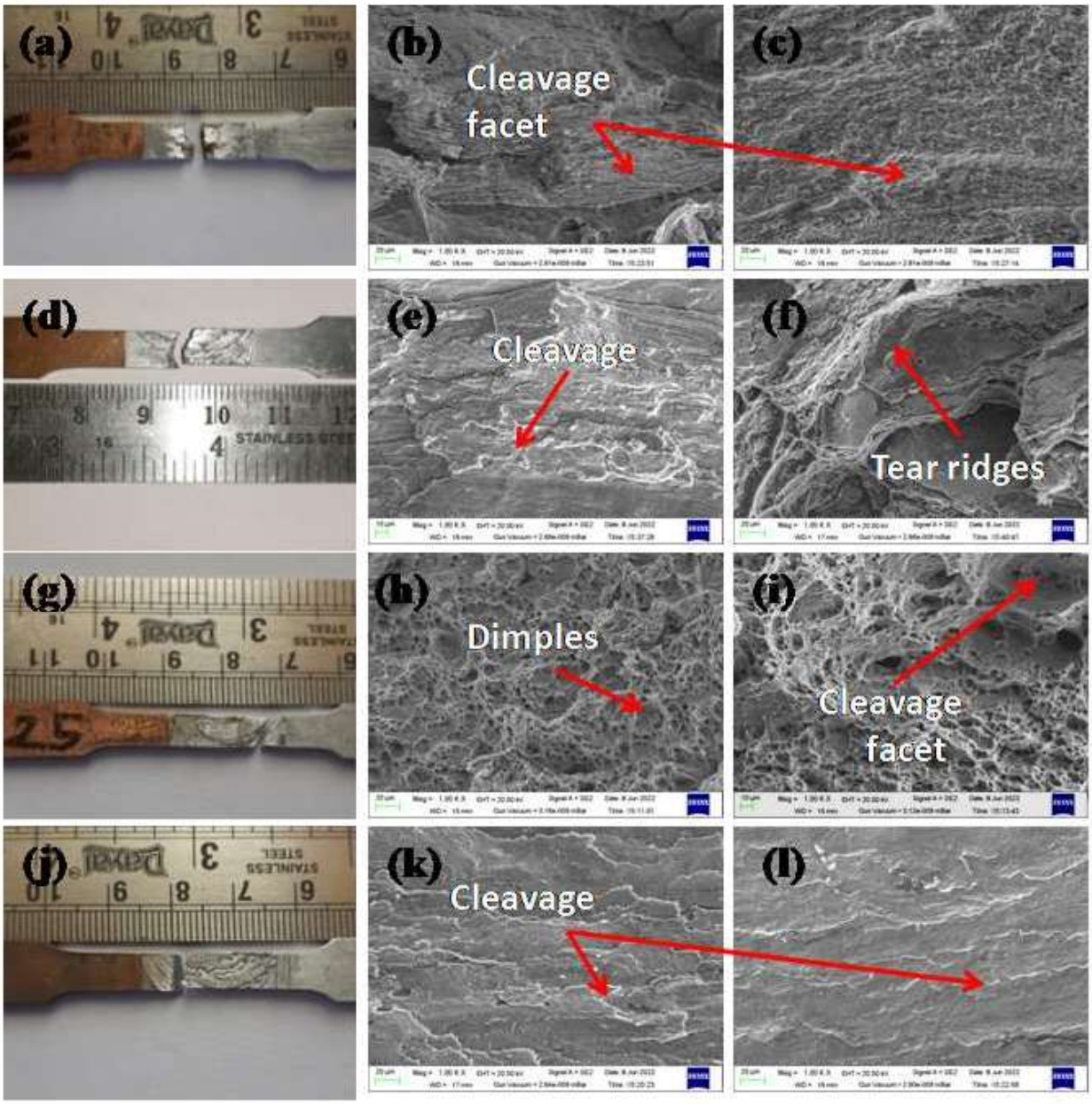

Fig. 4.11 Failure location with fractured surfaces of SCT tool at 1.2 mm/s (a, b and c), 1.5 mm/s (d, e and f), 1.8 mm/s (g, h and i) and 2.1 mm/s (j, k and l)

Cu dispersion in stir zone which results also uniformly distributed IMCs at stir zone which also increases the hardness to a modest amount (maximum SH-174 HV and maximum SCT-274 HV). At 2.1 mm/s, SH tool have good amount of mixing of Aland Cu which also increases dispersion strengthen effect and increases hardness (maximum SH-177 HV) and for SCT tool

comparatively better mixing of Al and Cu found at stir zone which reduces the formation IMCs. This lead to reduces in hardness (maximum SCT-168 HV) in the stir zone than others.

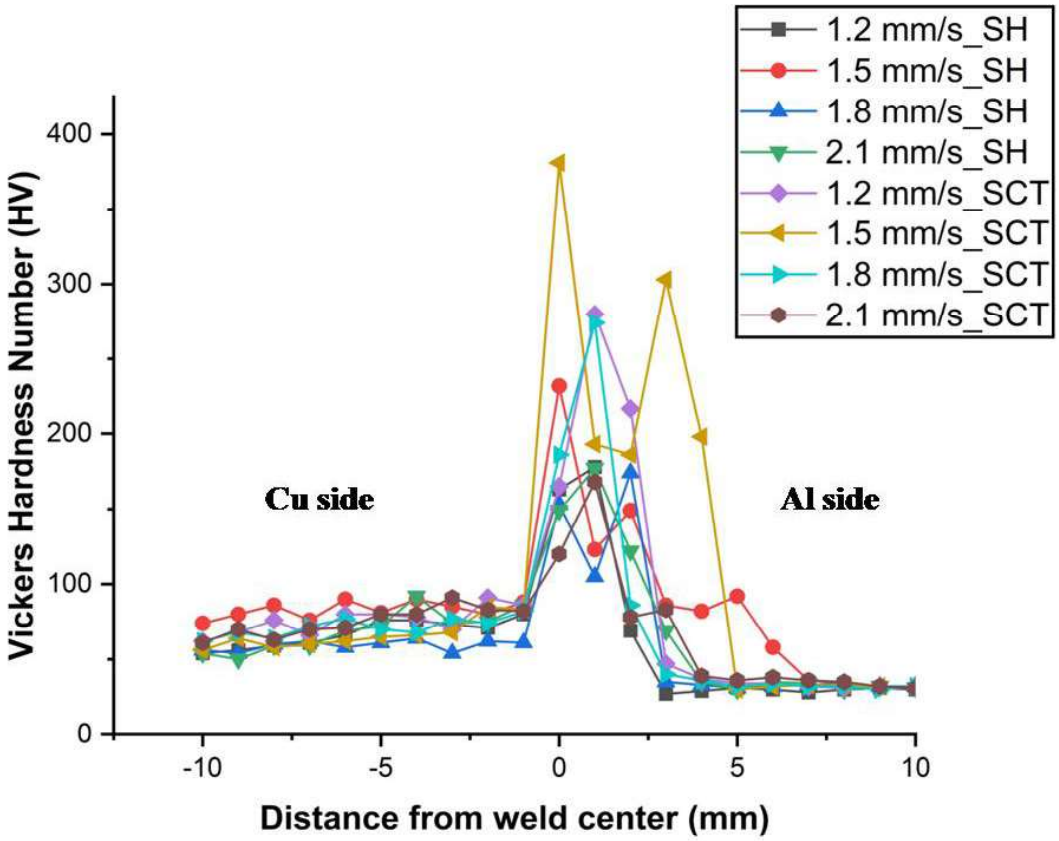

Fig. 4.12 Microhardness distribution for varying traverse speeds

4.8 Out Come of the Present Investigation

The present study focused on the effect of tool geometries on dissimilar Al and Cu joints at varying traverse speeds. The following key findings are summarized:

1. At the lowest traverse speed (1.2 mm/s), variation of tool pin geometries considerably affects the heat input (for SH-786.18 J/mm and SCT-525.18 J/mm), but at the highest traverse speed (2.1 mm/s) tool geometries have irrelevant on heat input (SH-536.04 J/mm and SCT-544.56 J/mm).
2. When the traverse speed is set to the lowest (1.2 mm/s), the surface bead exhibits excessive flash due to the SH tool generating excessive heat. Conversely, the SCT tool

presents surface defects (clusters of voids) due to improper mixing, resulting from low heat input caused by the tool slipping.

3. Tool geometry plays a vital role in mixing. At 1.2 mm/s, the SCT tool demonstrates inadequate mixing at the nugget due to tool slipping, leading to voids in the stir zone. In contrast, the SH tool exhibits better mixing with a lamella structure in the stir zone.
4. The even distribution of small Cu particles in the stir zone occurred at a speed of 1.8 mm/s for both tools enhanced tensile strength by improving bonding strength through dispersion-strengthening mechanism. Additionally, the SH tool demonstrated the highest ultimate tensile strength (UTS) at 93.4 MPa.
5. At 1.2 mm/s, the SCT tool has the lowest tensile strength (SCT-30.1 MPa) due to material flow defects caused by improper material flow at the stir zone.
6. At 1.8 mm/s, optimum heat input and adequate mixing result in the formation of IMC Al_4Cu_9, which increases the tensile strength of the SH tool. Low heat input and improper mixing show an uneven distribution of intermetallics Al_4Cu_9, AlCu, Al_2Cu, and Al_2Cu_3 at the lowest joint strength, at 1.2 mm/s, for the SCT tool.
7. The SCT tool indicates a maximum joint hardness of 381 HV may be due to uneven distribution of IMCs resulting from the insertion of large Cu and solid solution hardening at a speed of 1.5 mm/s.

Chapter 5:

Effect of Tool Geometries on Weld Quality of Al-Cu Dissimilar Joint for Varying Rotational Speed

5.1 Introduction

This chapter presents the study of dissimilar friction stir welding of 3-mm-thick 1100 aluminium alloy and commercially pure copper welded by a straight hexagonal tool and straight cylindrical tool to study the effect of pin geometry on varying rotational speeds. The effect on heat input during welding, bead surface morphology, microstructure, formation of IMCs, joint strength and hardness have included for the study. Present study was conducted with varying rotational speed at three different levels (800 rpm, 1200 rpm, and 1400 rpm) and traverse speed is kept constant (1.5 mm/s).

5.2 Effect of Tool Pin Geometries on Heat Input at Different Rotational Speeds

Heat input for all the welding is evaluated using equations (3.1) and (3.2) and plotted in Fig. 5.1. It was noticed that at 800 rpm heat input for SH tool (593.84 J/mm) was much higher than SCT tool (478.78 J/mm) whereas at 1200 rpm reverse happened (SH-556.91 J/mm, SCT-661.66 J/mm). But both tools show almost equal amounts of heat input at 1400 rpm (SH-641.82 J/mm, SCT-643.57 J/mm). The amount of energy depends on the amount of friction and deformation. The complete reversal of heat input for two different tool designs from 800 to 1200 rpm reflects for SH tool a slip may happen resulting in decreased friction and deformation. However, another significant observation is that at 1400 rpm the heat input remains almost unchanged for both tools. These reflect at higher rotational speed as material is sufficiently heated, the Design of tool pin has very little role to play in terms of deformation and thus resulting in similar heat input. However, for the SCT tool the heat input remains unchanged from 1200 to 1400 rpm. Hence it can be concluded that for SCT tool saturation in heat input may have happened. But as SH tool works on pulsating stirring action, it has resulted in increased energy due to higher pulse at increased rpm.

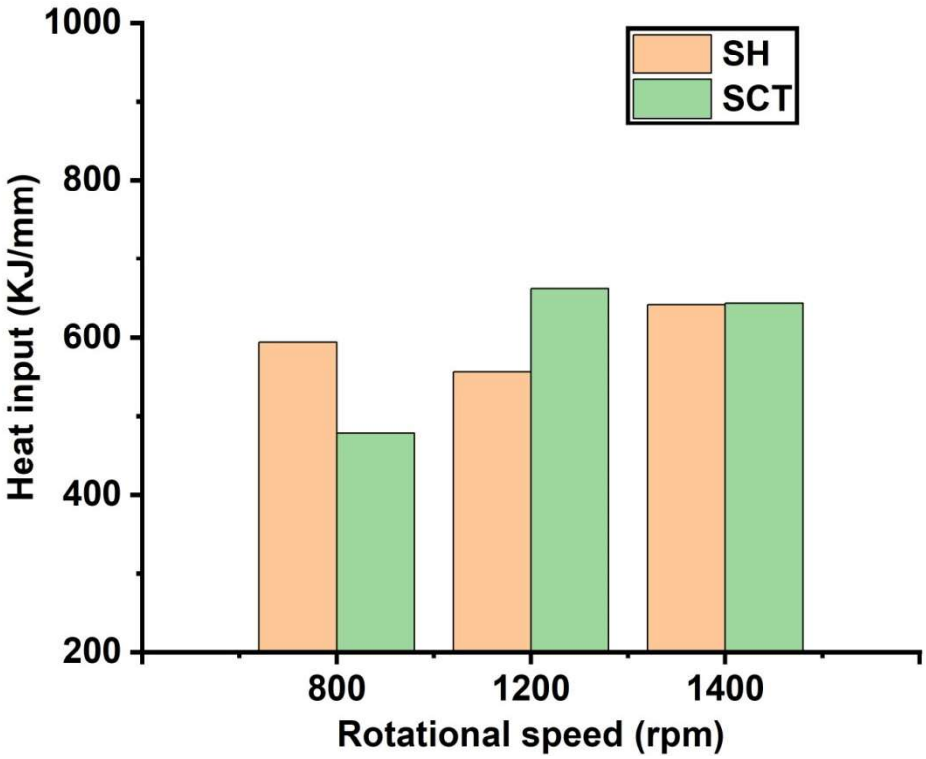

Fig. 5.1 Heat input at different rotational speeds for SH and SCT tool

5.3 Effect of Tool Geometries on Welded Surfaces at Different Rotational Speeds

Figure 5.2 shows the bead appearance for different pin designs at different rotational speeds. Hot flashes were seen at the edges of bead surfaces for both tools but it was more prominent for SH tool. It may be due pulsating stirring action of SH tool. Bead surfaces were poor at low rotational speed due to low heat generation which may resulted in increased flow stress restricting the materials from flowing easily over the bead surfaces [22]. Bead surfaces are getting smoother with an increase in rotational speed for both tools due to ease of material flow as the flow stress was less due to an increase in heat generation and stirring action. Moreover, at higher rotational speed, the weld pitch is low resulting in thinner layer.

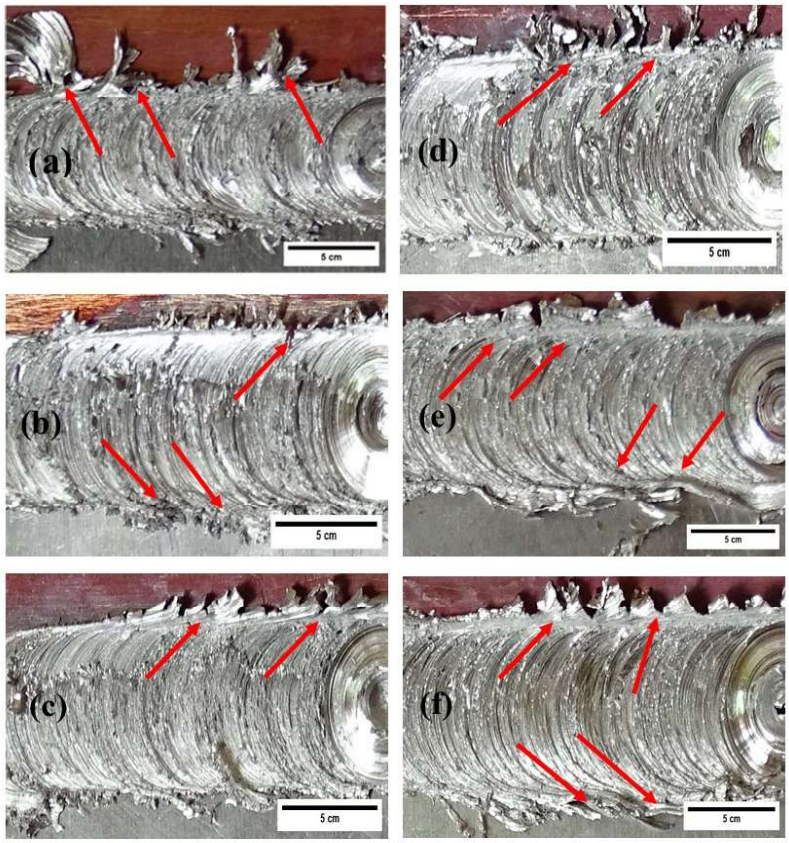

Fig. 5.2 Bead images (a) 800 rpm (b) 1200 rpm (c) 1400 rpm of SCT tool and (d) 800 rpm (e) 1200 rpm (f) 1400 rpm of SH tool

5.4 Effect on weld formation for Different Tool Geometries at Different Rotational Speeds

Microstructure examinations of SCT tool is shown in Fig. 5.3 At 800 rpm bulk Cu insertion (Fig.5.3a, b and c) to the stir zone has been observed for SCT tool. It may be due to less stirring action as well as less heat generation at 800 rpm which may be incapable of fragmenting Cu in small segments. At 1200 rpm incomplete material mixing (Fig. 5.3d,e, and f) was observed at the stir zone where very few Cu particles diffuse to the Al side, creating a clear separation between Cu and stir zone. However, the microstructure of stir zone for 1400 rpm (Fig. 5.3g, h and i) attains a laminated structure of Al-Cu layers with finer Cu particles. This shows an intense plastic deformation had happened at 1400 rpm for SCT tool and also a good mixing.

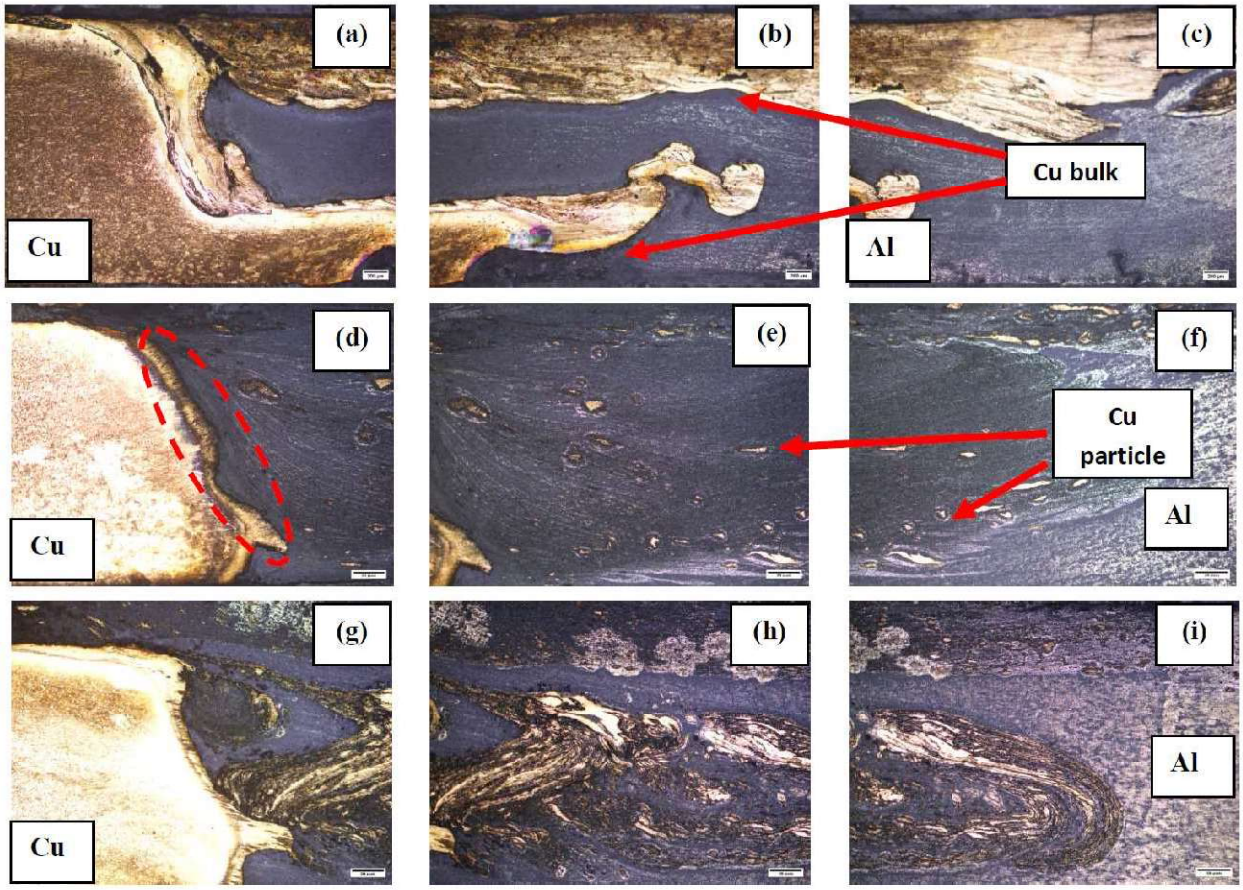

Fig. 5.3 Microstructures for SCT tool at 800 rpm (a, b, c), 1200 rpm (d, e, f) and 1400 rpm (g, h, i)

Microstructure examinations of SH tool are shown in Fig. 5.4. Well laminated Al-Cu layers are evident for SH tool at 800 rpm (Fig.5.4a, b and c) which is not the case for SCT tool at 800 rpm but for 1400 rpm. This shows SH tool is capable of providing good mixing at low rotational speeds. However, at 1200 rpm the mixing is not good and the laminated Al-Cu layers are faded (Fig. 5.4d and e). This represents a lack of shearing of material around the tool pin at 1200 rpm. As rotational speed increases further 1400 rpm the pattern of material flow changes from thin layered laminated structure to bulk Al-Cu diffusion where Cu diffuses at the top and Al diffuses from the bottom of weld (Fig. 5.4f and g).

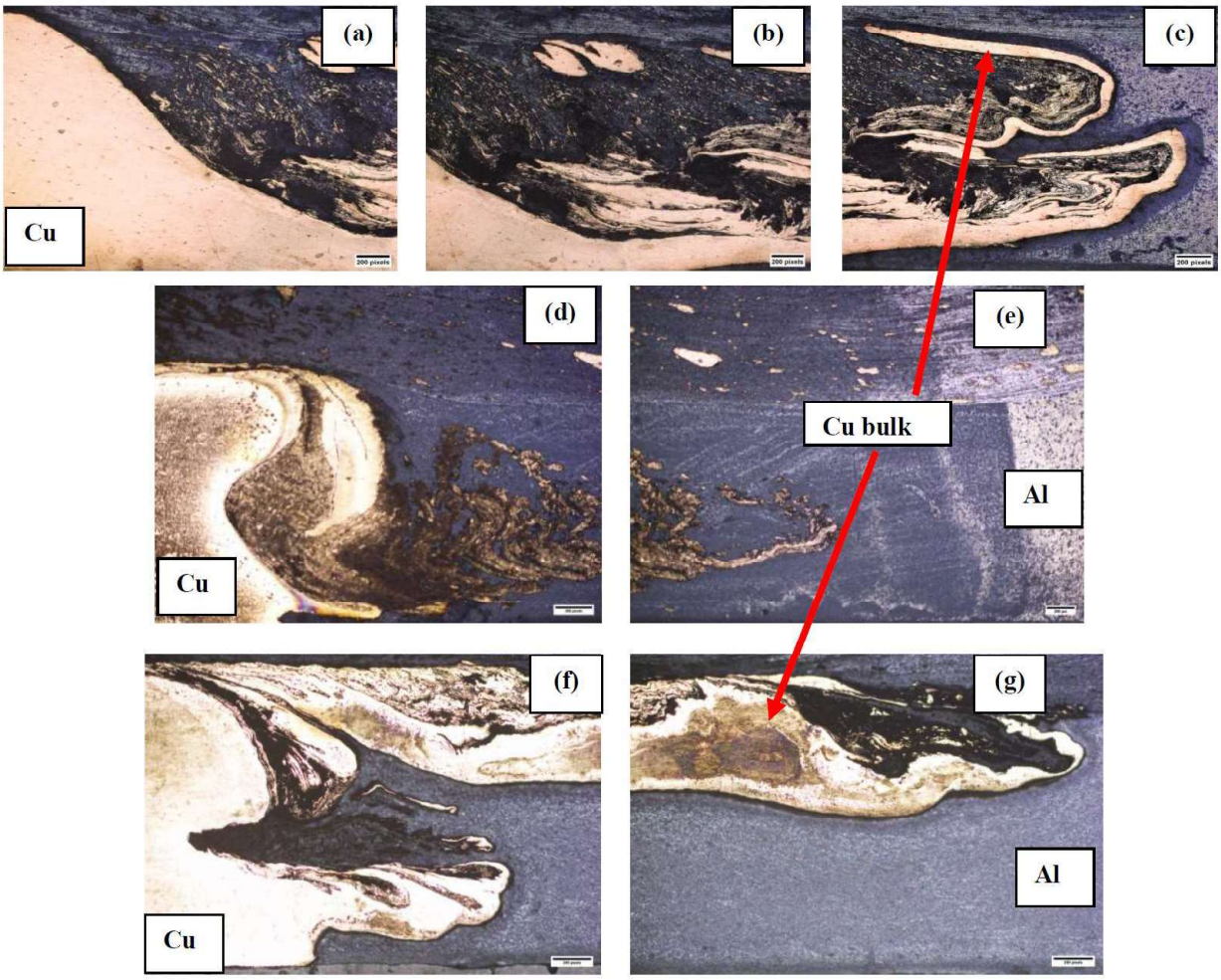

Fig. 5.4 Microstructures for SH tool at 800 rpm (a, b, c), 1200 rpm (d, e) and 1400 rpm (f, g)

5.5 Effect on Microstructure for Different Tool Geometries at Different Rotational Speeds

IMCs are formed due to differences in chemical composition, physical properties, and heat generation produced during welding of Al and Cu. Formation of IMCs can harm joint strength due to higher hardness resulting in brittle structure[26][32][39][20]. Besides the bulk movement of Al and Cu, there exists a small region of Al-Cu lamellae for SH tool at 1400 rpm. This region (Fig. 5.5a) has been focused here further on any formation of IMCs and a fine distribution of Cu particles (Fig. 5.5b, c) was observed. Further, the EDS analysis (Fig. 5.6) at different interfaces within this region shows a uniform presence of $Al+Al_2Cu$[74][75] at P1, P3 and P4 and Al_2Cu

[72][74] at P2 with a finer level. This fine distribution and formation of $Al+Al_2Cu$ and Al_2Cu IMCs may attributed to adequate heat generation and increased pulsating action.

From Fig. 5.7a it can be seen that Cu struggles to flow as thicker Cu lamellae are created but these lamellae are not well separated at 1200 rpm for SH tool. The borders are not very sharp and diffused to the next Cu layer in various positions. In between Cu layers, the Al layers are not very prominent and very scattered. The EDS analysis (Fig. 5.8) reveals a wide category of IMC formation at various points (Fig. 5.7b, c), and those are not very uniformly distributed. At P1 $Cu+Al_4Cu_9$ [72][73] is created which is also a very hard intermetallics. At points, P3 and P4 the atomic weight percentage of Cu and Al show the probable formation of a solid solution of Al[27]. However, there is a presence of $Al+Al_2Cu$ is also observed at point P2. The formation of $Cu+Al_4Cu_9$ is very detrimental as it is one of the hardest IMC [78] of Al-Cu combinations possible.

The flow pattern of SCT tool for 1400 rpm (Fig. 5.9a) consisted of well-separated thin Al-Cu lamellae. These thin lamellae were observed for SH tool at 1400 rpm. But for SCT tool it occupies the whole stir zone whereas for SH tool it is limited to a very narrow region on Cu side (advancing). The EDS analysis (Fig. 5.10) reveals the presence of $Cu+Al_4Cu_9$ at P4 along with $Al+Al_2Cu$ at P1 and P3 and Al_2Cu at P4. The presence of $Cu+Al_4Cu_9$ indicates a possible increase in the hardness of the structure. However, the thin distribution of the lamellae and the equal presence of $Al+Al_2Cu$ and Al_2Cu may counter this.

For 1200 rpm the SCT tool attains a poor mixing between Al-Cu where the stir zone is fully occupied with Al (Fig. 5.11a) and the flow of Cu is restricted to the retreating side by a sharp interface. The EDS analysis (Fig. 5.12) shows presence of AlCu [72][74][75][79] at P1 and $Cu+Al_4Cu_9$ at P2 on the retreating side near Al-Cu interface (Fig. 5.11b). In the mid-stir zone (Fig. 5.12c), the presence of Cu is almost negligible at P3 and P4, making it more vulnerable at the interface between Al-Cu.

EDS analysis shows the predominance of $Al+Al_2Cu$ at 1400 rpm where material mixing was most uniform irrespective of pin design. Again it was also observed that at 1200 rpm mixing was improper for both tools where IMC $Cu+Al_4Cu_9$ was observed at interface for both tools and IMC AlCu was also found at interface for SCT tool which has maximum heat input.

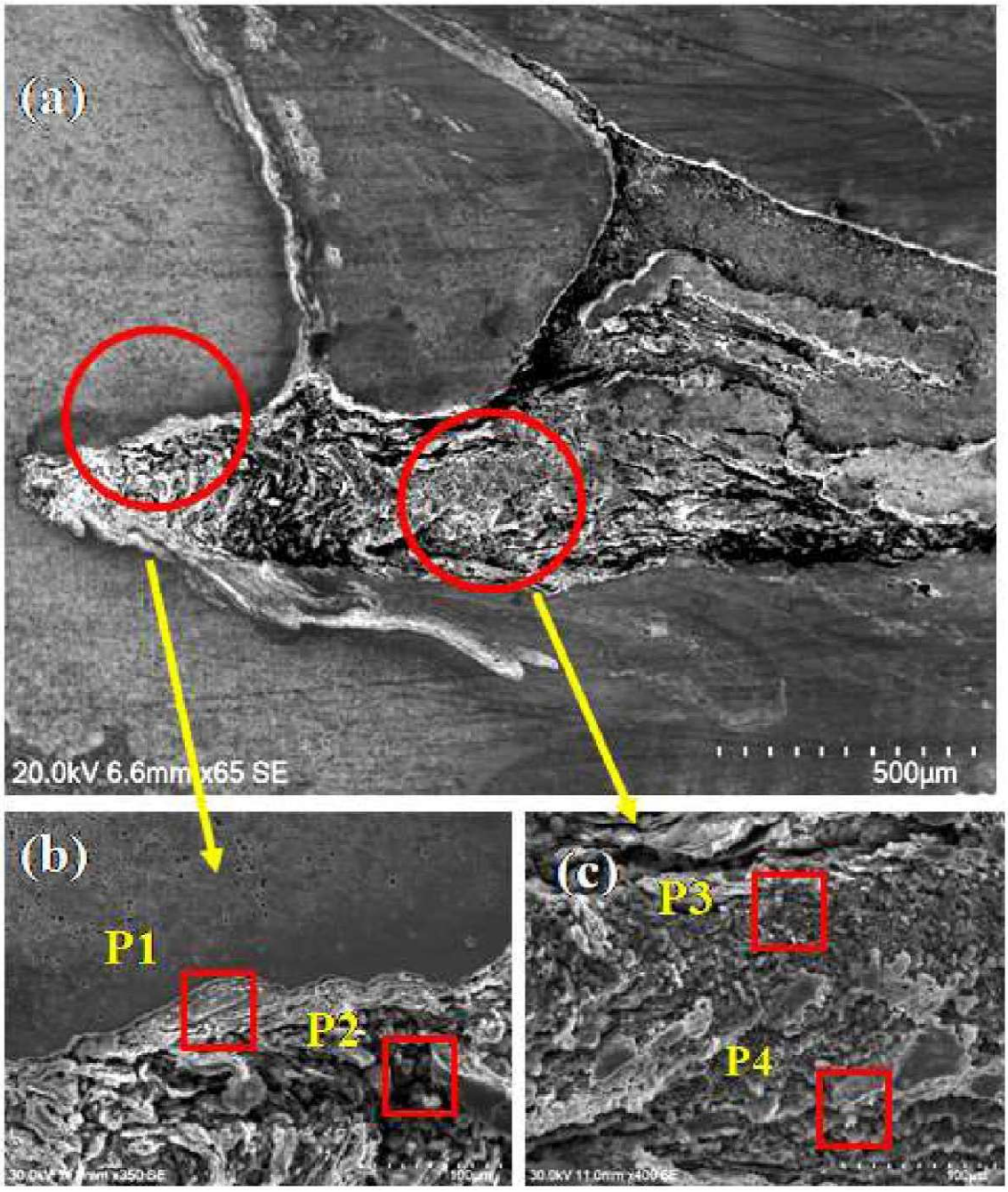

Fig. 5.5 SEM images at 1400 rpm of SH tool

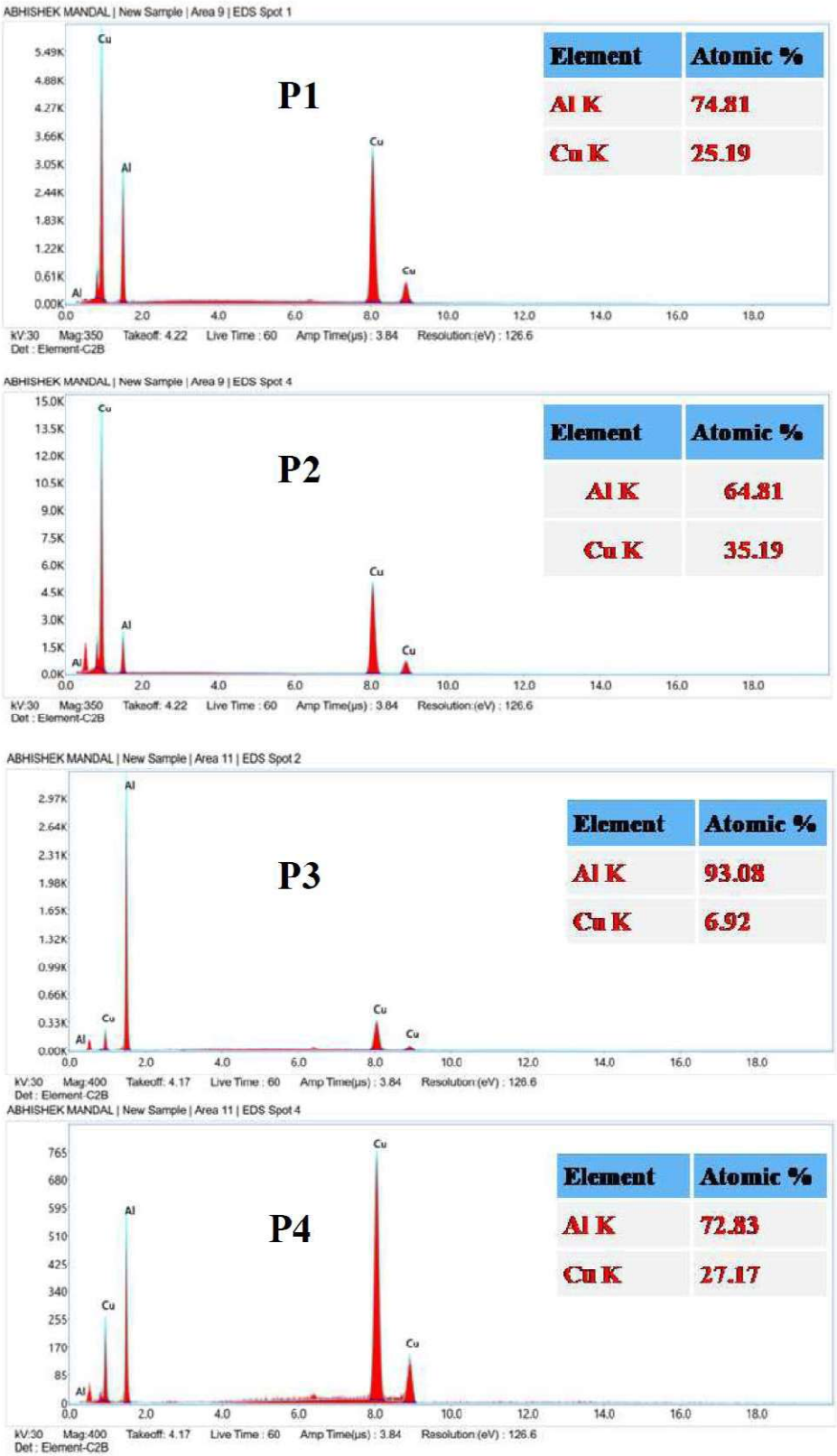

Fig. 5.6 EDS analysis at 1400 rpm of SH tool

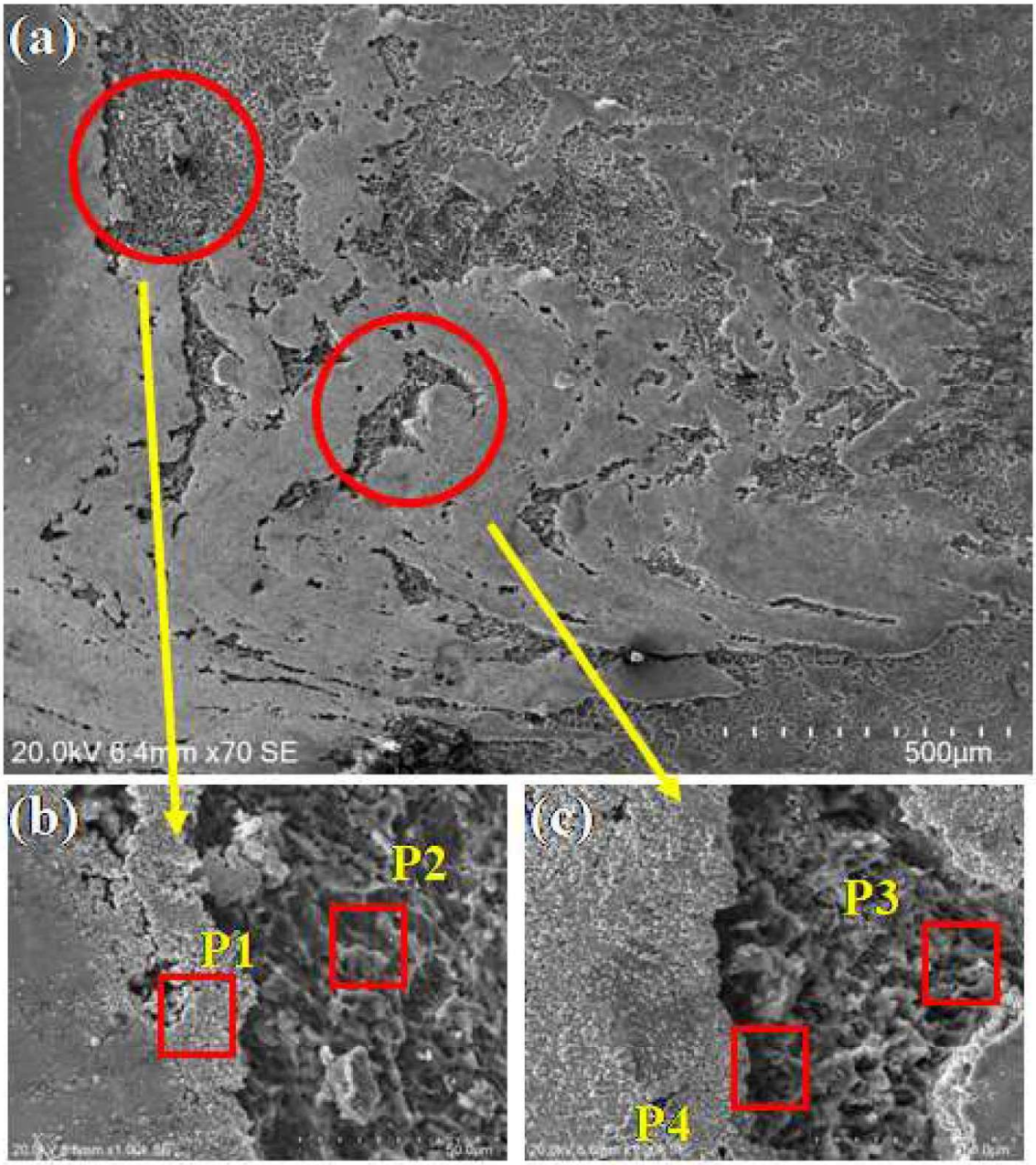

Fig 5.7 SEM images at 1200 rpm of SH tool

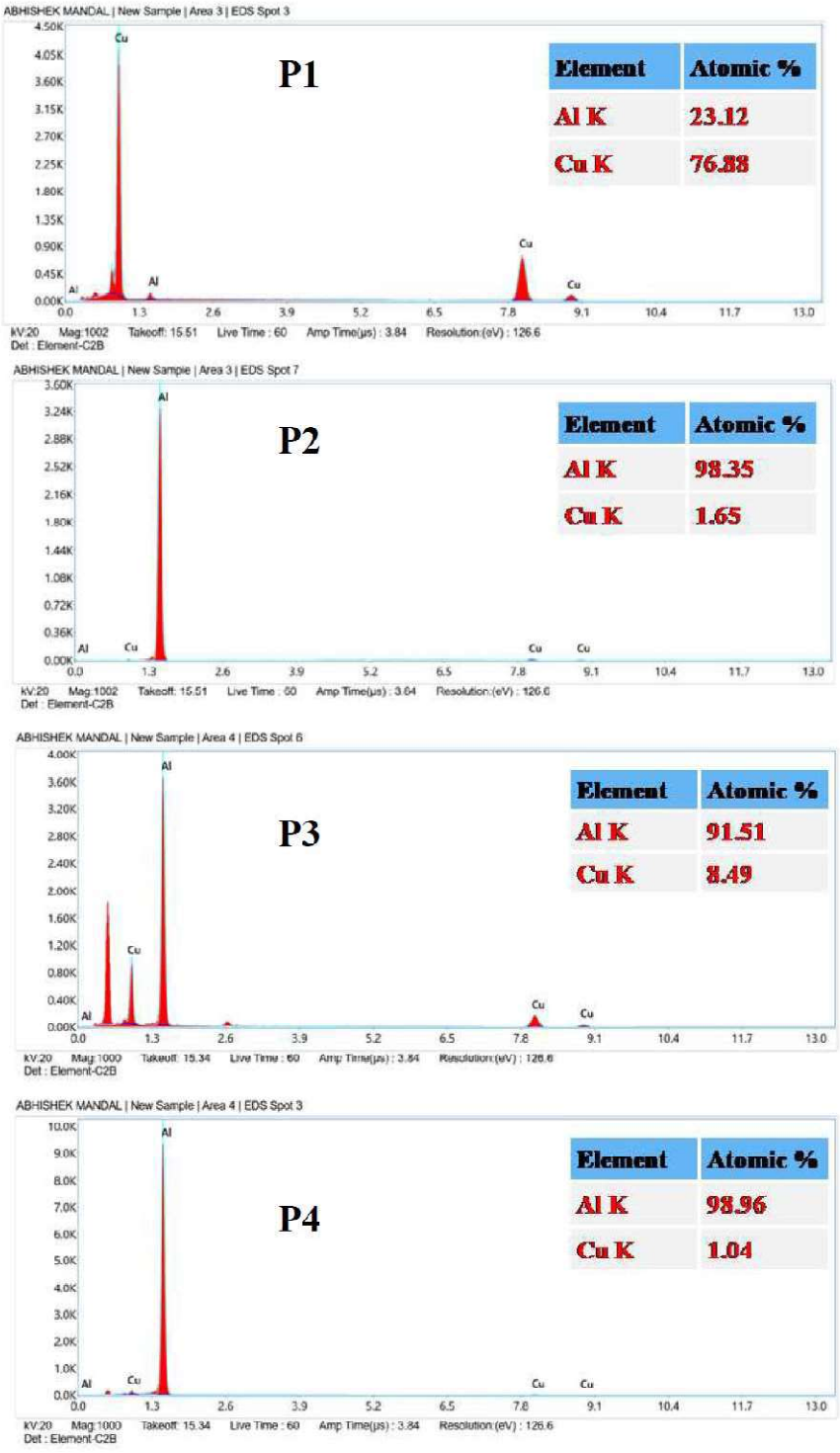

Fig. 5.8 EDS analysis at 1200 rpm of SH tool

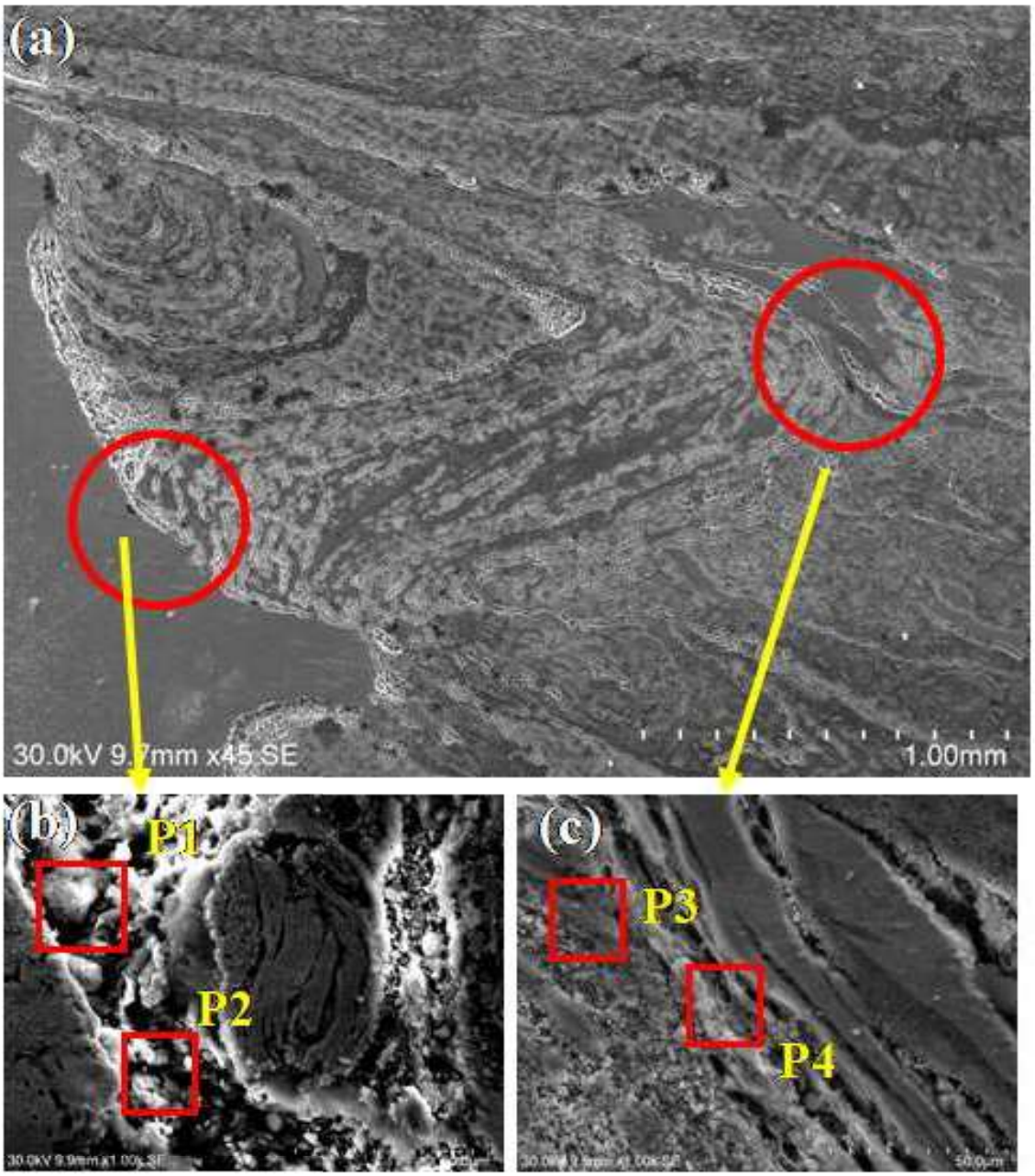

Fig. 5.9 SEM images at 1400 rpm of SCT tool

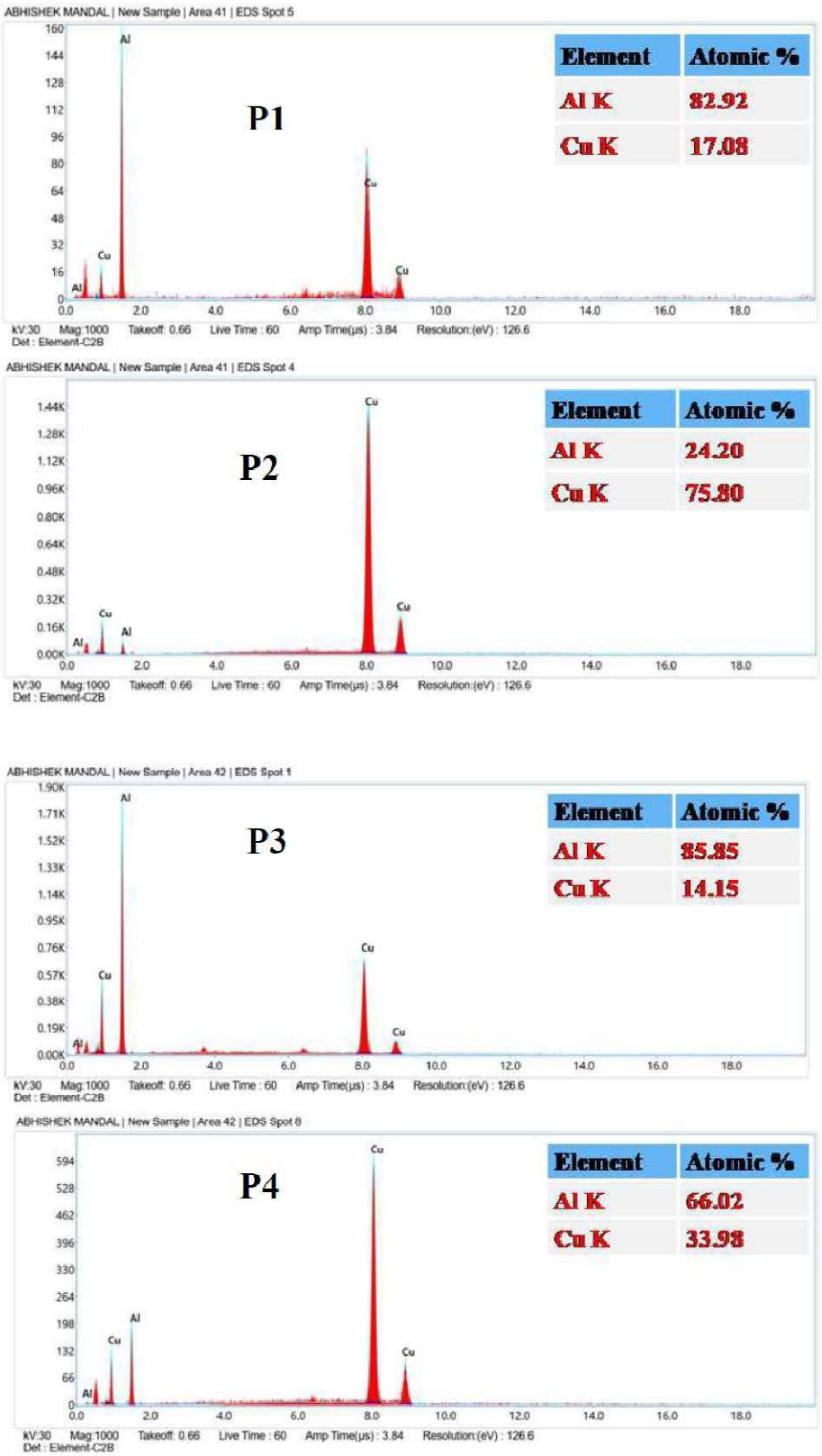

Fig. 5.10 EDS analysis at 1400 rpm of SCT tool

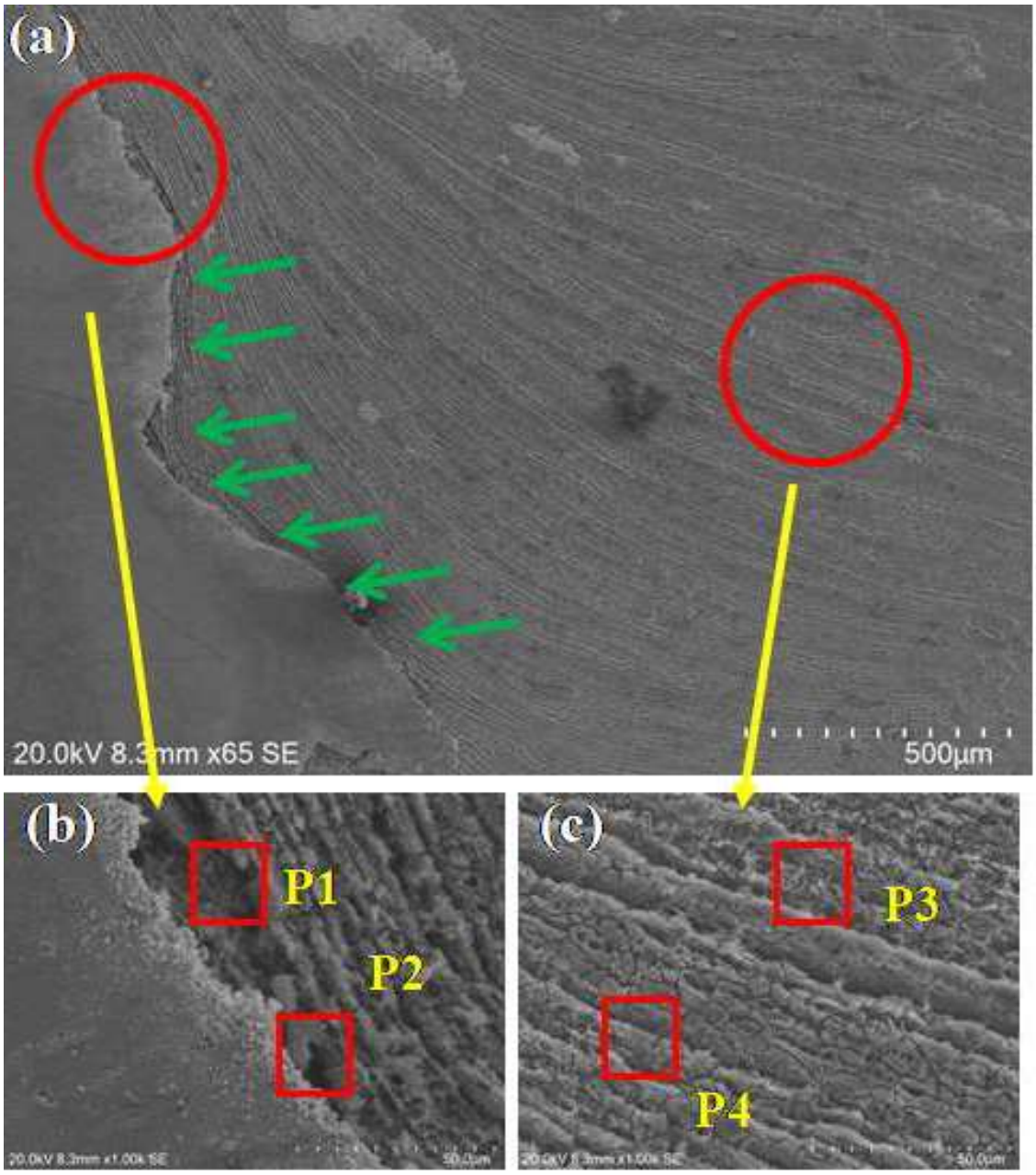

Fig. 5.11 SEM images at 1200 rpm of SCT tool

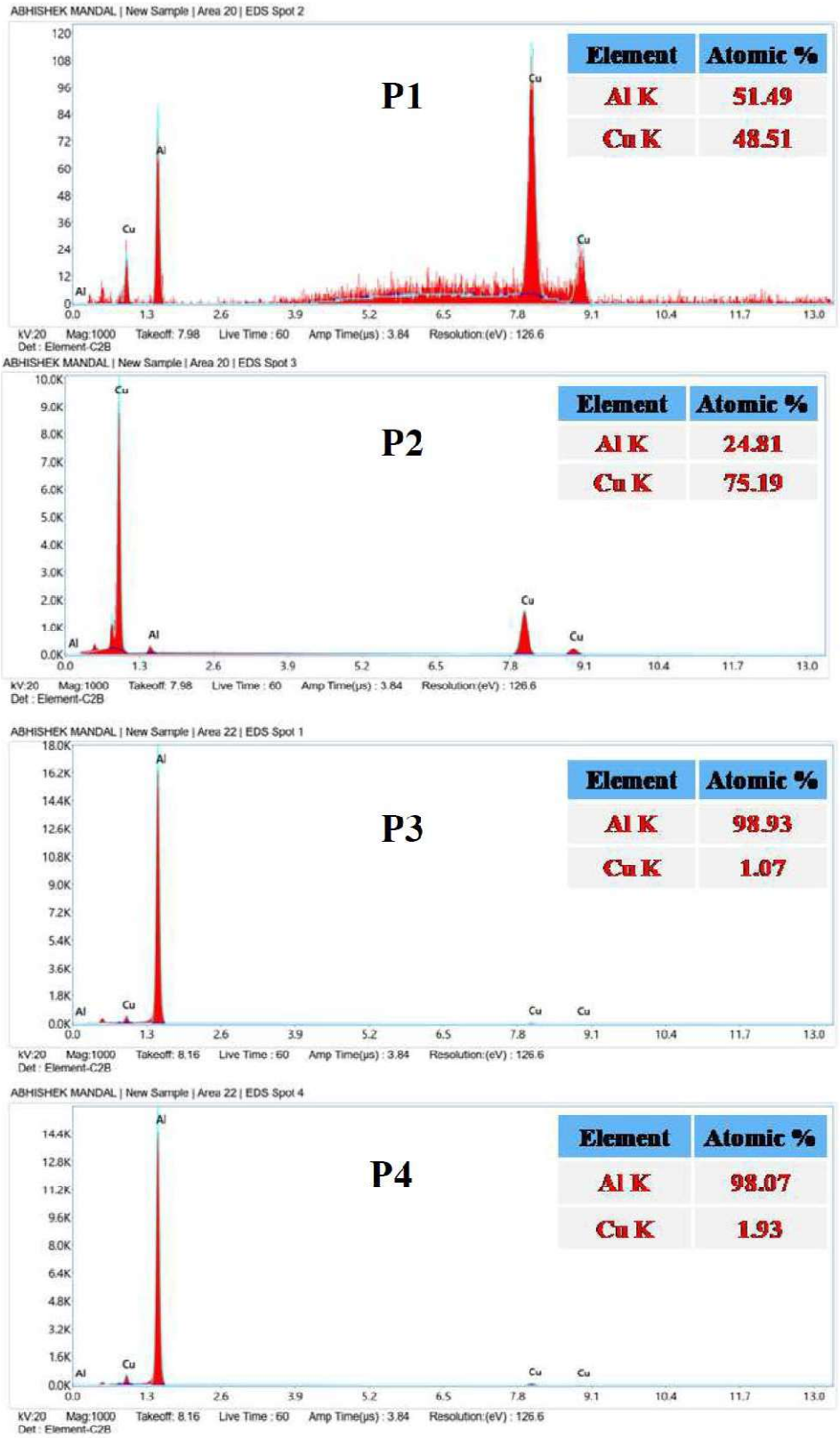

Fig. 5.12 EDS analysis at 1200 rpm of SCT tool

5.6 Effect on Interfacial Layer for Different Tool Geometries at Different Rotational Speeds

The interface layers of Al-Cu which were created due to mixing at high temperatures are the breeding ground of IMCs due to the availability of both elements & it is temperature and time-dependent also[80][81][82]. A line scan of line EDS analysis is considered at the Al-Cu interface to ascertain how frequently the Al-Cu layer exists and their elemental distribution at those interfaces for probable formation of IMCs. The junction between the Al and Cu line depicts the interface and the width of those junction points represents the layer thickness. The frequency of those junctions occurring along the length represents the intensity of mixing and the probability of IMC formation.

At 1400 rpm for SCT tool the span (width of the marked box) of the first meeting point is quite wide and also intersects at several places and continuous elemental fluctuation is observed (Fig. 5.13a). This represents a good mixing but the higher interfacial layer thickness at the beginning increases the probability of IMC formation. At 1200 rpm it is observed that Al-Cu line intersects (Fig. 5.13b) only at a single point and the span of the meeting zone is narrow. Moreover, the elemental fluctuations are also less compared to 1400 rpm. At 1200 rpm heat input is the highest among all, however, the elemental distribution and interfacial layer thickness are less for SCT tool. This represents the mixing of Al and Cu in stir zone is very poor and in stir zone, the formation of IMCs is also less. At 800 rpm the Al-Cu line intersects at fewer points. It was observed that at 800 rpm (Fig. 5.13c) heat generation was lower in SCT tool and also bulk insertion of Cu due to less mixing causing small intermetallic layer thickness and less elemental fluctuation.

Figure 5.14a shows that at 1400 rpm interfacial layer thickness was highest for SH tool as an adequate amount of heat input and stirring forms better mixing of Cu to Al which leads to increased interfacial layer thickness and also continuous fluctuation of elemental distribution of Cu and Al shows sufficient diffusion of Cu into Al. Additionally, these intersecting points depict the stacking of layers creating a lamellar structure, which may improve the strength.

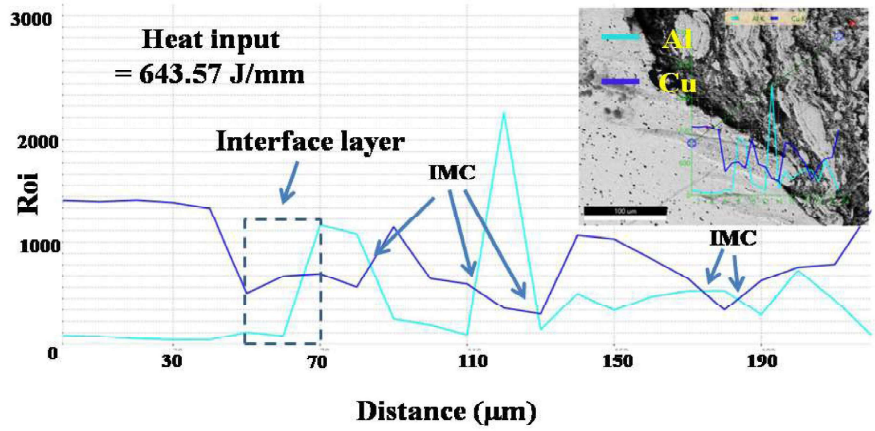

(a)

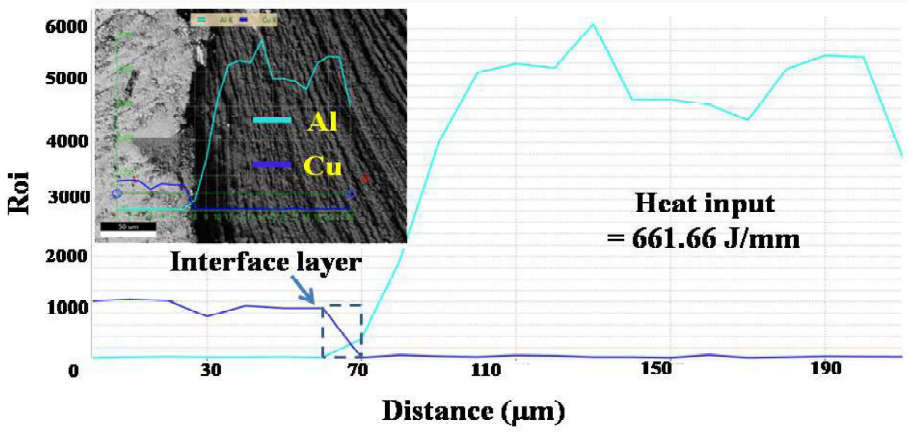

(b)

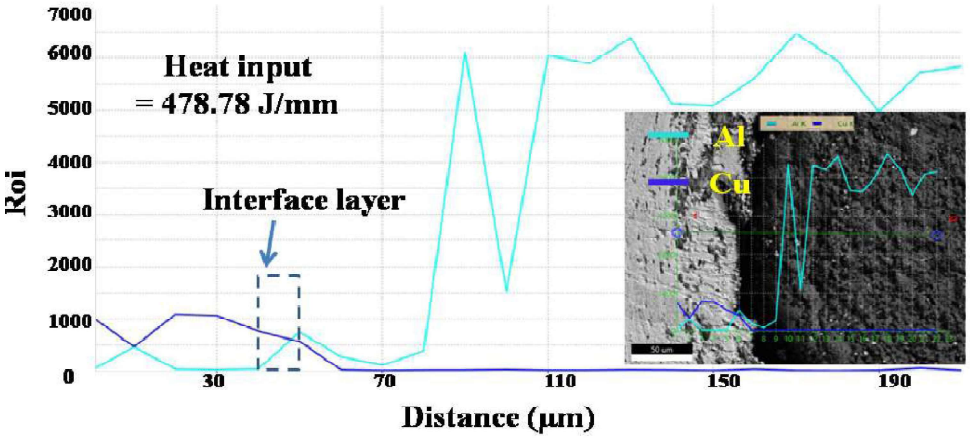

(c)

Fig. 5.13 Line scan at Al-Cu interface of SCT tool at (a) 1400 rpm (b) 1200 rpm (c) 800 rpm

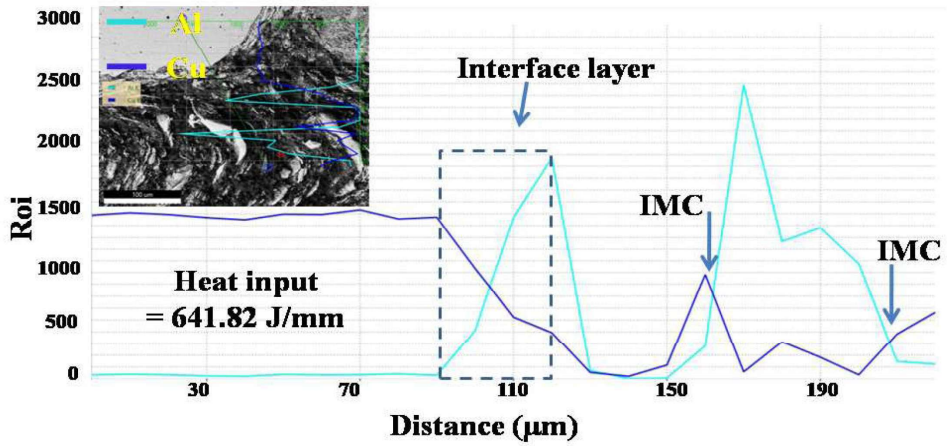

(a)

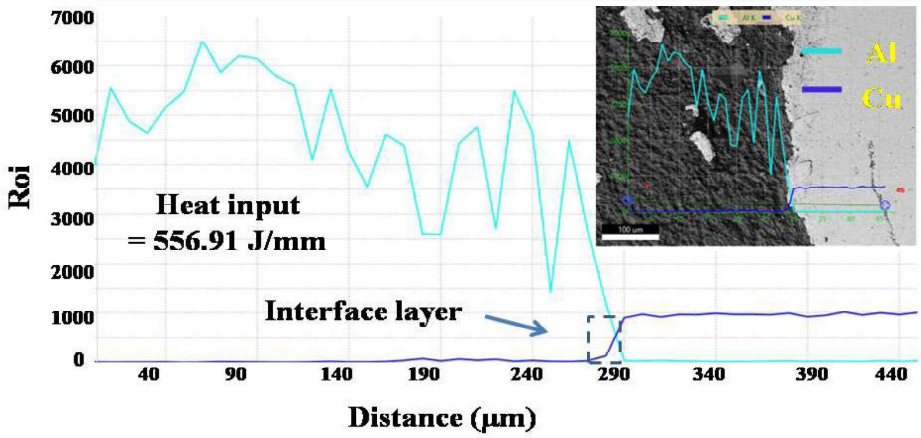

(b)

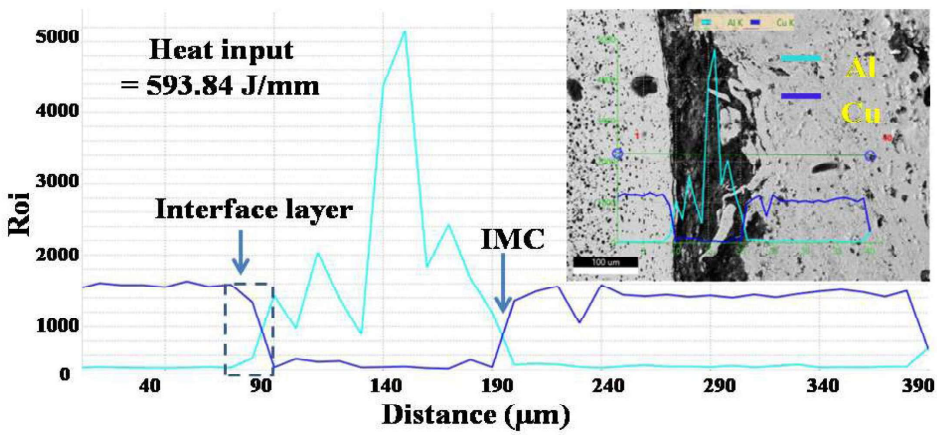

(c)

Fig. 5.14 Line scan at Al-Cu interface of SH tool at (a) 1400 rpm (b) 1200 rpm (c) 800 rpm

Figure 5.14b shows at 1200 rpm interfacial thickness was smaller and there was less elemental fluctuation on Al side which also states that tool struggles to mix material due to less plasticization and improper material mixing. The heat input at 1200 rpm (556.91 J/mm) is comparatively lower for SH tool than 800 rpm (593.84 J/mm) and 1400 rpm (641.8222 J/mm). For SH tool diffusion of Cu into Al was better at 800 rpm (Fig. 5.14c) than 1200 rpm (Fig. 5.14b) which is assisted by higher heat input resulting thicker interfacial layer. In addition, there is an elemental fluctuation in the interface.

5.7 Tensile Strength and Fractography Analysis

Figure 5.15 shows UTS for different rotational speeds for both tools. At 800 rpm both tools have good joint strength (SH- 77 MPa and SCT- 62.9 MPa) but the SH tool shows more strength due to better mixing and the presence of lamella structure (Fig. 5.4a, b, and c). Moreover, the stir zone consists of finer Cu particles. Figure 5.16a shows failure occurred at stir zone for SCT tool. Dimple, tear ridges, flat facet along with microcracks observed in Fig. 5.16b, c. This shows a

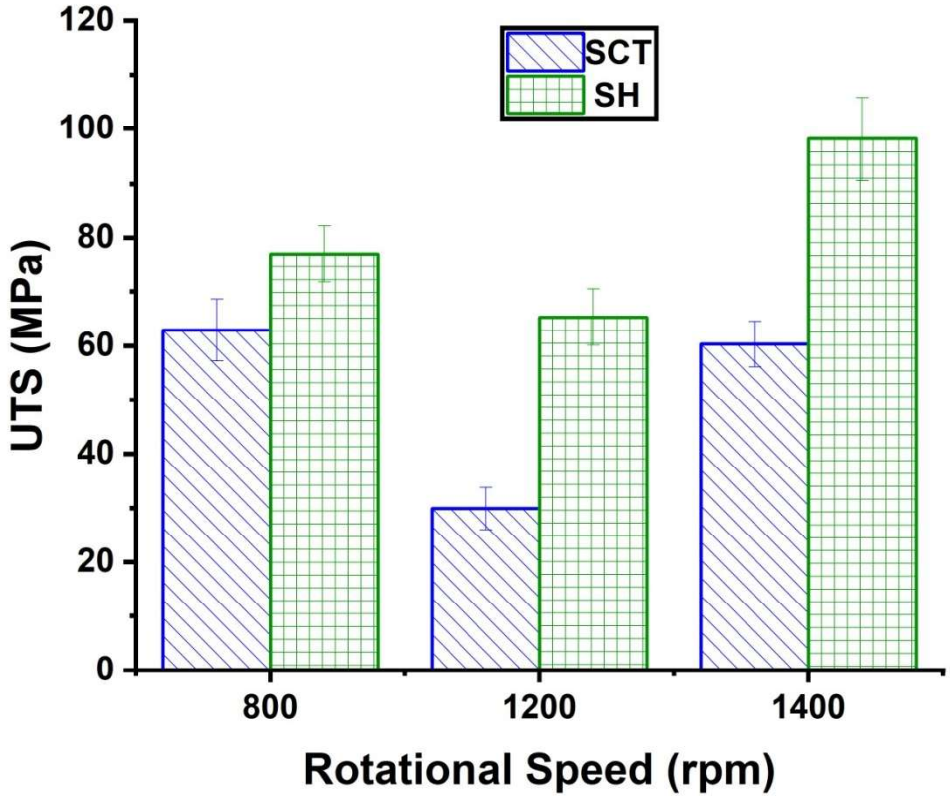

Fig. 5.15 UTS at different rotational speeds for different tools

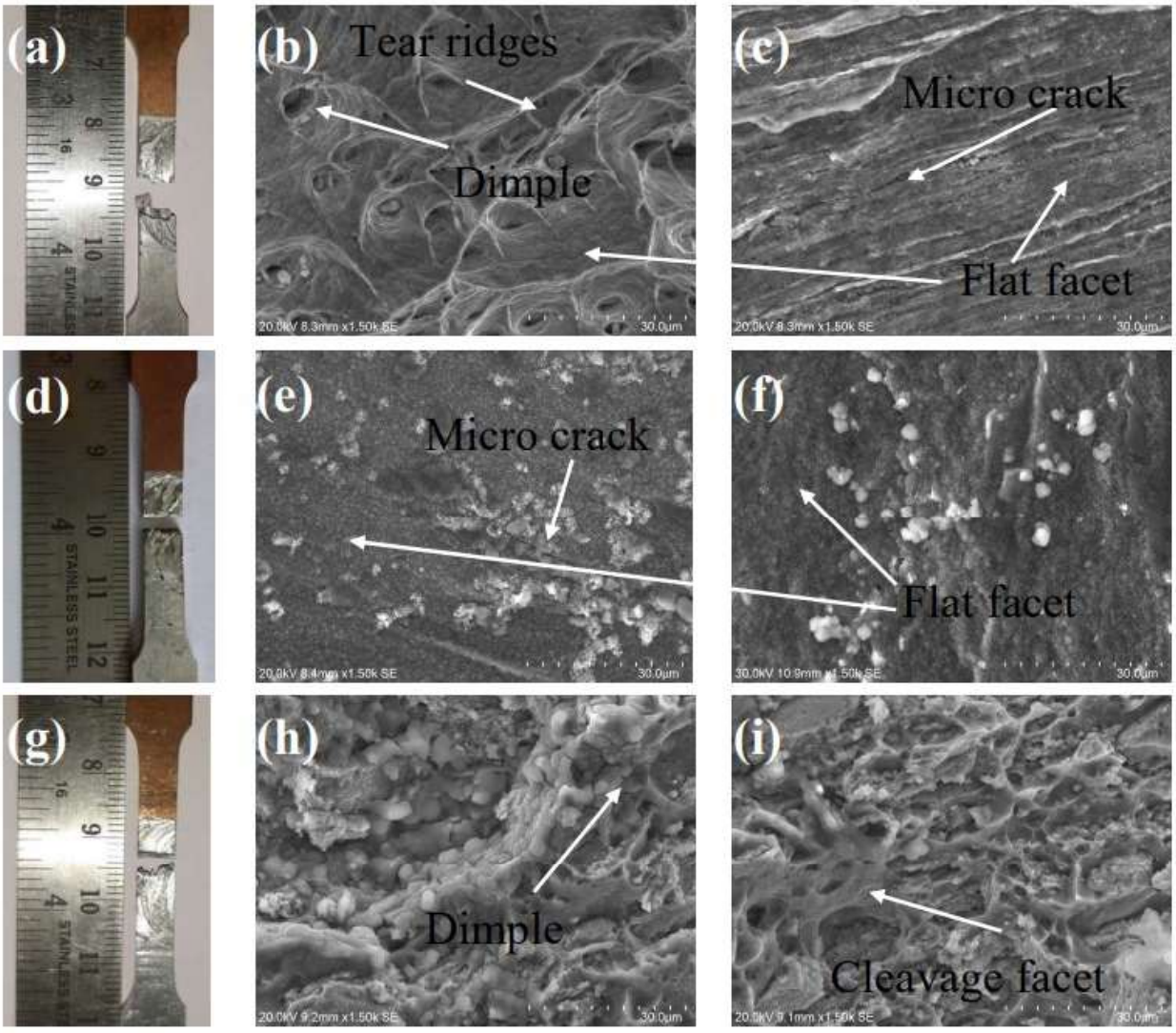

Fig. 5.16 Failure location and fractured surface of SCT tool at 800 rpm (a, b and c), 1200 rpm (d, e and f), and 1400 rpm (g, h and i)

mixed mode of failure had occurred for SCT tool. For SH tool also at 800 rpm a mixed mode of failure at stir zone (Fig. 5.17a) is observed along with the presence of dimple as well as flat facet (Fig.5.17b, c). At 1200 rpm both tools show a decrease in tensile strength (SH- 65.3 MPa and SCT- 29.9 MPa). However, for SCT tool reduction is very drastic due to crack formation. Fig. 5.16d and 5.17d depicts that both tool failed at stir zone. The fractography analysis shows the presence of micro crack and flat facet (Fig. 5.16e,f) for SCT tool and cleavage facet along with micro cracks at fractured surfaces (Fig. 5.17e, f) for SH tool indicating a brittle fracture. For 1400 rpm the tensile strength improves for both the tools (SH-98.2 MPa and SCT- 60.3 MPa).

This may be attributed to the formation of lamella structure (SCT tool, Fig. 5.3g, h and i) and bulk material movement(SH tool, Fig. 5.4f, g). Fig. 5.16g and 5.17g clearly depicts that failure propagated from stir zone to Cu side for SCT tool and TMAZ-Al side for SH tool. The fractography analysis shows a mixed mode of failure as presence of dimple and cleavage facets (Fig. 5.16 h, i) facets for SCT tool and dimple and flat facets the fractured surfaces (and 5.17 h, i) for SH tool.

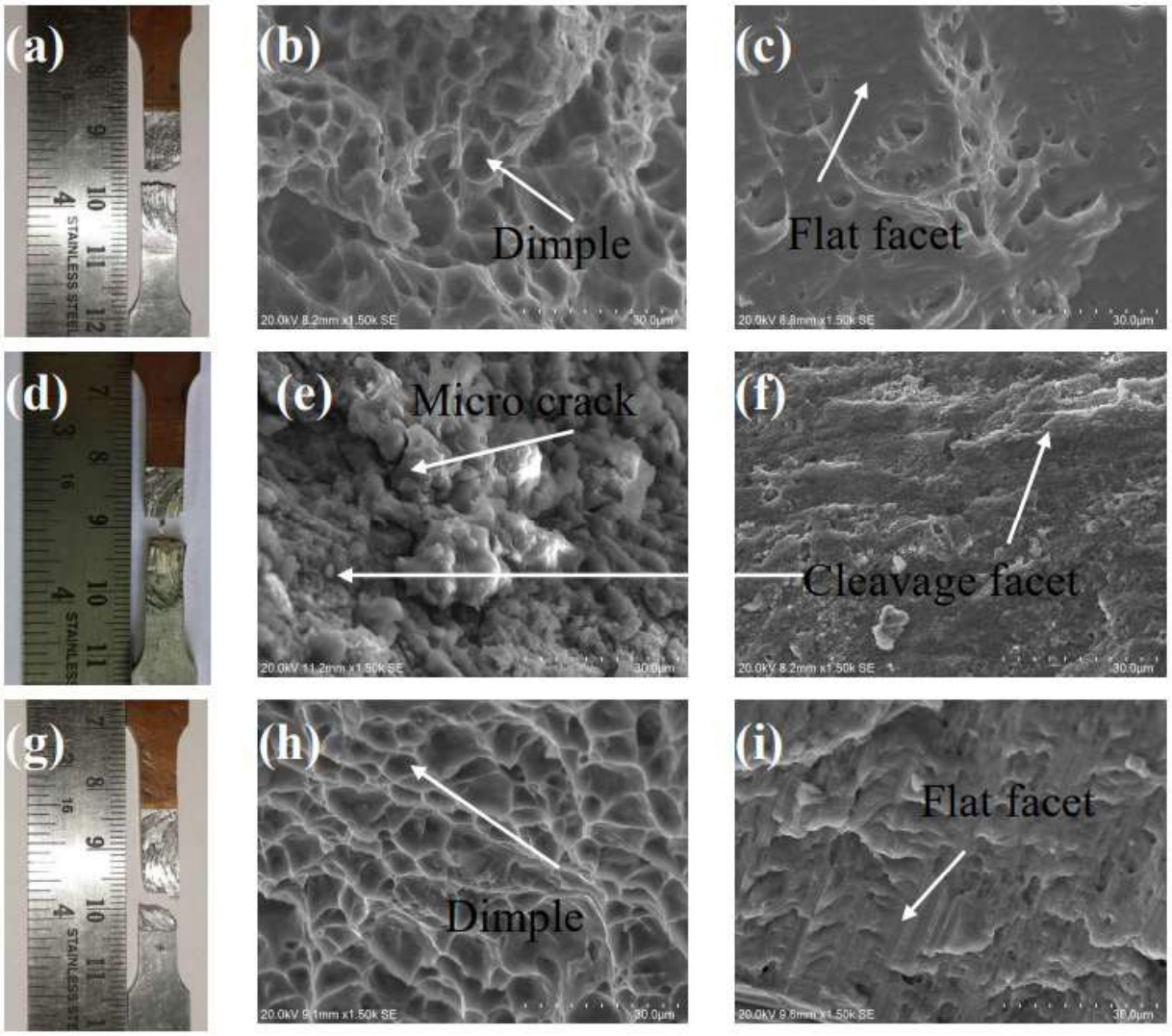

Fig. 5.17 Failure location with fractured surface of SH tool at 800 rpm (a, b and c), 1200 rpm (d, e and f), and 1400 rpm (g, h and i)

5.8 Effect on Hardness for Varying Rotational Speed for Both Tools

Variations in microhardness for different rotational speeds are plotted in Fig. 5.18 for both tools. Hardness values show a sudden increase at stir zone caused by formation of IMCs and plastic deformation [46][83]. A higher heat input and intense plastic deformation cause high amount of IMCs. At 800 rpm, due to formation thick lamellar structure of Al-Cu caused a sudden increase in hardness at stir zone with a maximum value of 133.7 HV for SH tool. For SCT tool the sudden increase in hardness is caused by intense plastic deformation of Cu which causes bulk movement of Cu at stir zone (maximum hardness of 133.4 HV) [46]. At 1200 rpm for SCT tool the heat input is highest (661.66 J/mm) that resulting excessive formation of hard and brittle IMCs (Fig. 13b and 14 P1, P2) at interface resulting highest hardness among all (maximum-172.3 HV). Whereas for SH tool a drastic decrease in hardness is observed at stir zone (maximum-117 HV). This is caused by less mixing and fewer IMCs at stir zone due to low heat input. At 1400 rpm both the tool attains approximately same hardness variation (SH maximum-139.5 HV and SCT maximum-136.5 HV) and it is caused by better material mixing and the approximately same amount of heat input.

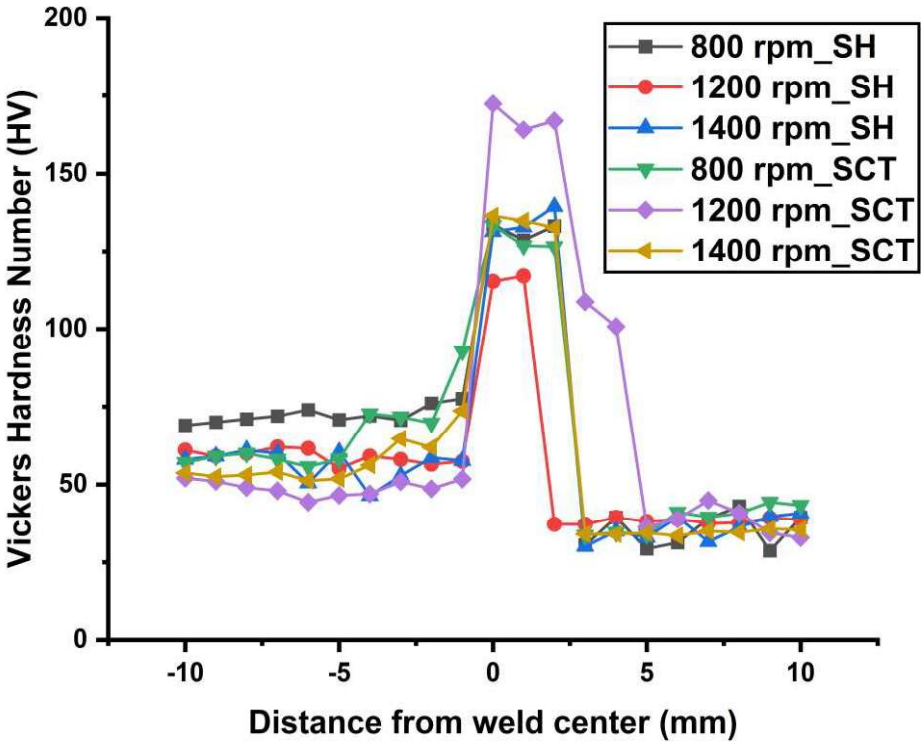

Fig. 5.18 Microhardness distribution of different pin geometries varying rotational speeds

5.9 Outcome of the Present Investigation

The present study focused on the effect of tool geometries on dissimilar Al and Cu joints at varying rotational speeds. The following key findings are summarized:

1. At lower rotational speeds the tool pin profile variation significantly affects the heat input (for 800 rpm SH- 593.84 J/mm, SCT-478.79 J/mm), whereas at higher rotational speed there was no noticeable effect of tool geometries on heat input (SH-641.82J/mm, SCT-643.57 J/mm).
2. The appearance of bead surfaces becomes smoother at high rotational speed (1400 rpm) due to better material flow over the surface, which is caused by adequate heat generation for both tools.
3. At 1200 rpm, incomplete mixing for the SCT tool was observed, with a sharp Al-Cu interface at the advancing side. However, a lamella structure was obtained at the stir zone for the SH tool, where Al-Cu layers are not very well separated.
4. At 1400 rpm, intense plastic deformation with fine particle distribution at the stir zone was achieved for both tools. In addition, a bulk movement of Cu was observed for the SH tool. Well-separated thin Al-Cu lamellae were observed for the SCT tool at the stir zone.
5. Line EDS analysis reveals improper mixing with a thinner interfacial layer for both tools at 1200 rpm. However, the interaction of Al and Cu line from line EDS analysis shows a better mixing of Cu to Al by both tools at 1400 rpm.
6. SH tool attained maximum tensile strength (SH-98.2 MPa) at 1400 rpm and minimum (SH-65.3 MPa) at 1200 rpm, whereas SCT achieved the maximum tensile strength (SCT-59.6 MPa) at 800 rpm and minimum (SCT-29.9 MPa) at 1200 rpm. However, among all the welds, the SH tool provides better tensile strength than the SCT tool, irrespective of rotational speeds.
7. For improved tensile strength, Al+Al_2Cu intermetallics were predominantly observed. An excessive formation of AlCu intermetallics was observed for weaker welds. EDS analysis also revealed that intermetallics Cu+Al_4Cu_9 may be a reason for decreasing tensile strength.
8. The highest hardness value, 172.3 HV, was found at the interface for the SCT tool at 1200 rpm due to the form of excessive IMCs assisted by the highest heat input.

Chapter 6:

Weld Quality Analysis by Signal Characterization

6.1 Introduction

The present work traces the weld quality by analyzing torque and force signals for Al/Cu dissimilar FSW. The captured torque and forces often possess relevant information, which is not always distinguishable from the raw data. Thus, a need for further processing of that raw information arises. Here, original signals were decomposed to approximate and detail signals using discrete wavelet transform (DWT) to find possible relations with different weld properties. The present work has been divided into two parts. In the first part, the investigation was done keeping the rotational speed constant at 1000 rpm, but the traverse speed varies at 1.2 mm/s, 1.8 mm/s, and 2.1 mm/s. In the second part, the traverse speed is kept constant at 1.5 mm/s, but rotational speed varies from 800 rpm to 1400 rpm with an increment of 200 rpm.

6.2 Finding the Best Mother Wavelet Function and Corresponding Level

Best mother wavelet function and their corresponding level for the spindle torque and Z-force was selected from SH tool at 1.8 mm/s and 1000 rpm for vaying traverse speed (1.2 mm/s, 1.8 mm/s and 2.1 mm/s) due to SH tool shows highest tensile strength at 1.8 mm/s. Accordingly, it has been split into detail and approximate signals for multiple levels (Fig. 6.1) with available mother wavelet functions (Coiflet, Daubechies, Symlet). Finally, the highest energy-to-entropy ratio values for different mother wavelet functions at optimum level of decomposition was compared for the maximum. It was found that after decomposition of signals, mother wavelet functionSymlet 6 (sym6) at level 4 for spindle torque and coiflets 1(coif1) at level 4 for Z-force has been found suitable for decomposition applying the “maximum energy to entropy ratio” criteria (Fig. 6.2). Similarly highest tensile strength among all the welding (SH tool - 1400 rpm, 1.5mm/s, 98.2 MPa) considering both the tools has been selected for varying rotational speed. In this study, after decomposition into multiple levels (Fig. 6.3) with various mother wavelet functions, it has been found that wavelet function sym 4 at level 5 satisfies for spindle torque and Daubechies 3 (db 3) satisfies at level 5 for Z-force (Fig. 6.4). A comparison of the maximum energy to entropy ratio of different mother wavelet functions is presented in Fig. 6.3, 6.4. For the final analysis, the approximate signal at the corresponding level is considered, and for the detail signal, all the decomposed levels are added and considered as the sum of detail signal (considering the negative part of the detail signal as positive).

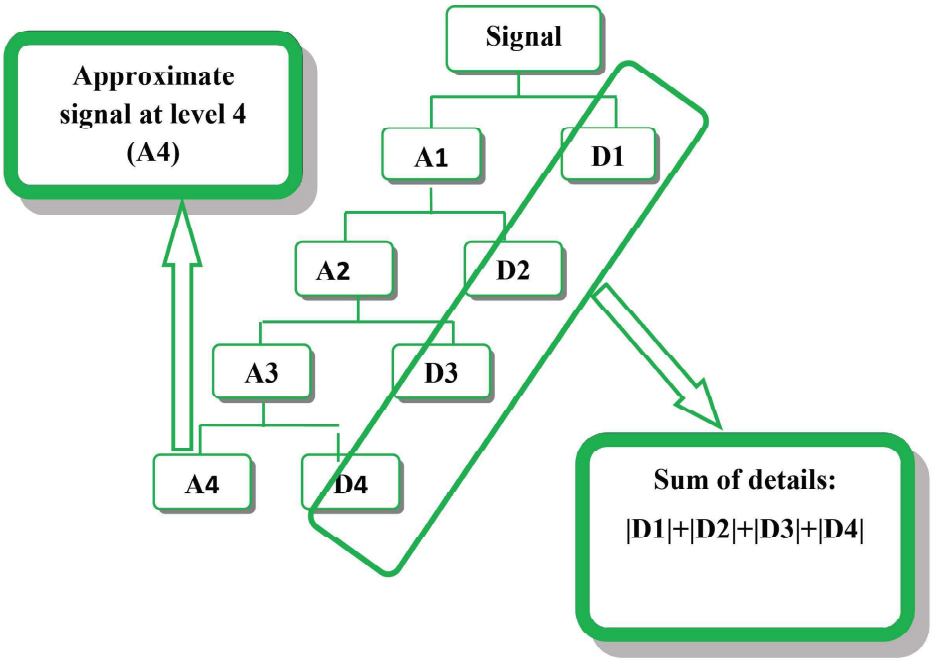

Fig. 6.1 Schematic representation of wavelet decomposition for varying tra verse speed

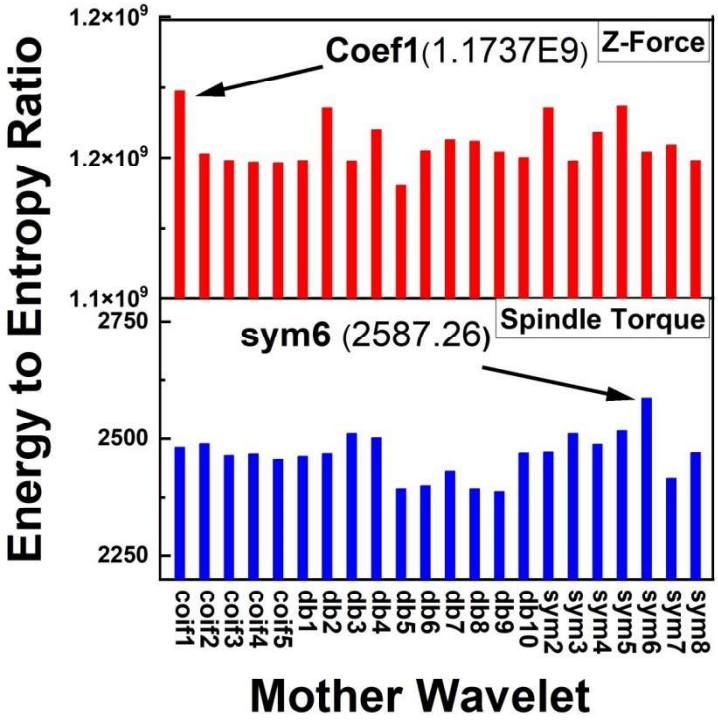

Fig. 6.2 Selection of mother wavelet function for varying traverse speed

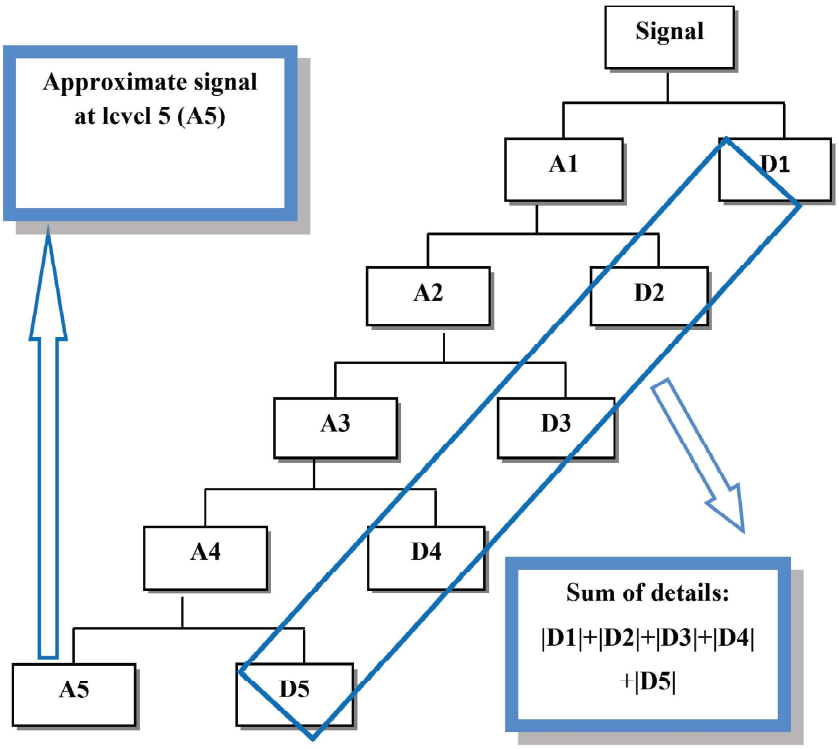

Fig. 6.3 Schematic representation of wavelet decomposition for varying rotational speed

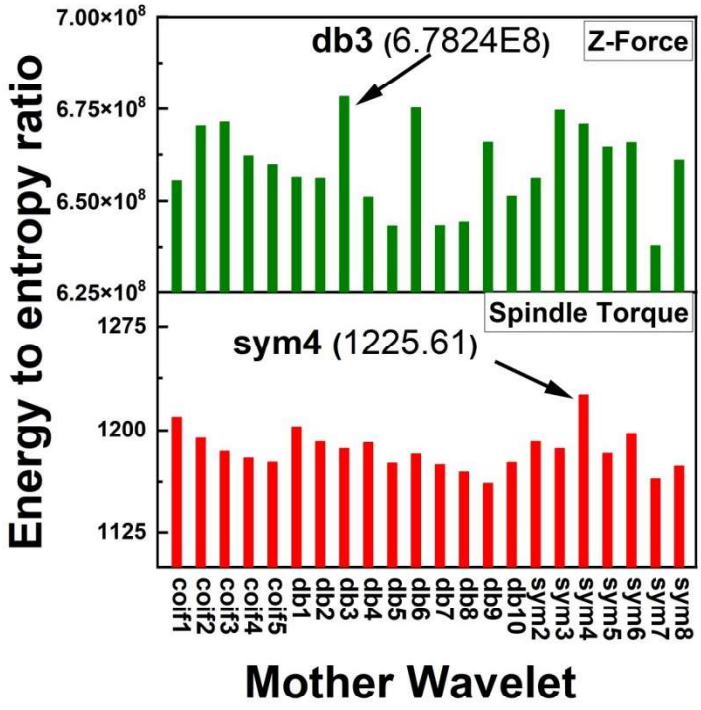

Fig. 6.4 Selection of mother wavelet function for varying rotational speed

6.3 Analysis of Signals for Varying Traverse Speed

6.3.1 Analysis of Spindle Torque

Figure 6.5 presents variation of spindle torque for both the tools with time for different traverse speeds. With changes in traverse speed and tool geometry, variation is very prominent. However, ascertaining a particular pattern is difficult. It can be seen that at 1.2 mm/s the spindle torque distribution resembles a lot of similarity for both the tool though they are of different magnitude. At 1.2 mm/s, spindle torque drastically fall at 7s(approx.) for SCT tool and reaches at 5 Nm (approx.) whereas for SH tool this spindle torque falls near about at 9 Nm(approx.). SCT tool have visible more fluctuating major peaks whereas SH tool's such peaks are comparatively less.

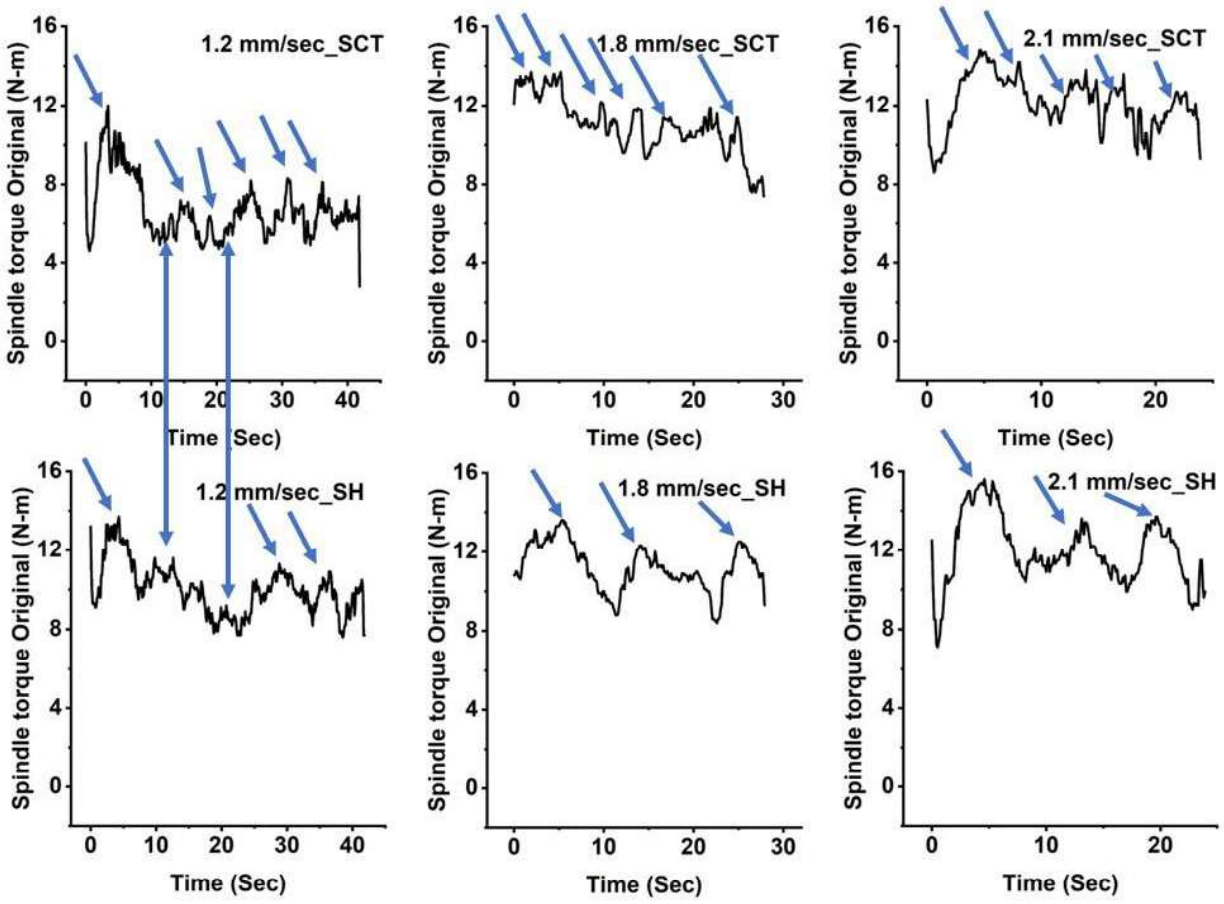

Fig. 6.5 Original spindle torque distribution for varying traverse speed

When traverse speed increases further to 1.8 mm/s, the amplitude of fluctuation for spindle torque signal reduced for SCT tool whereas for SH tool, fluctuation has been reduced with

increase smoothness and periodic nature and also the width of the peaks widens. These reductions of number of peaks shows as traverse speed increases tool–work piece slip reduces and SH tool is capable of providing less slip at increased traverse speed. Hence a more uniform material flow may be achieved by SH tool. Further, the torque distribution of 1.8 mm/sec and 2.1 mm/sec for SH tool have some similarities. The initial peak for 2.1 mm/sec reaches to 16N-m but for 1.8 mm/sec, it is around 13N-m. This happened due to a lack of heat input at increased traverse speed. Moreover from 1.8 mm/sec to 2.1 mm/sec the width of that peak reduces indicating an increasing slipping tendency. However, an important observation for SCT tool at 2.1 mm/s is that again major visible peaks have increased fluctuations showing the incapability of SCT tool to provide uniform torque and frequent slipping may have occurred. For more detail investigation of the disorder in spindle torque, original spindle torque has been divided into approx. signal and detail signal (Fig.6.6 and 6.7).

6.3.1.1 Analysis of Approximate Spindle Torque Signal

Drawing an accurate conclusion from the original torque signal is often difficult as it contains low-magnitude, high-frequency components. Approximate torque signal in Fig. 6.6 provides a clearer picture of high-magnitude torque signals. For the SCT tool, at 1.2 mm/sec, the overall profile of torque distribution shows an initial hike of approximately 10N-m, and after that, peak magnitude remains almost the same, which is around 6-7 N-m. A valley region was observed between the second and third peaks, which is unclear from the original spindle torque (Fig 6.6, around 17-22s). This drastic reduction of torque (from the first peak, 10 N-m, to the rest of the peak, 6-7 N-m) is due to a lack of initial heating at the beginning. At 1.8 mm/sec for the SCT tool, the approximate signal initially goes up to approximately 12 N-m; for 2.1 mm/sec, it is around 14 N-m. As welding proceeds, the subsequent peaks are reduced down to 11 N-m, approximately at1.8 mm/sec and at 2.1 mm/sec; it moves around 12 N-m. An interesting trend observed for the SCT tool is that the torque peaks continuously reduce in magnitude (1.8 mm/sec, 2.1 mm/sec). In contrast, for 1.2 mm/sec other than the first peak, the rest of the peaks are of approximately the same magnitude. The approximate signal for the SH tool at 1.2mm/sec shows more peaks than the SCT tool, with a valley of around 17 to 22 Sec. The overall approximate signal torque signals for the SH tool at 1.2 mm/sec are higher than the SCT tool, which is valid for the rest of the welding. However, the comparison of the approximate signal of

the SH tool with the SCT tool shows that the peak attained by the SH tool is broader than the SCT tool. For 1.8 mm/sec, a valley-like region is observed after the second peak, whereas for 2.1 mm/sec, this valley appeared before the second. These valleys can be observed more prominently in approximate signal than in original torque. For the SCT tool, the initial peak magnitude increases from approximately 12.5 N-m to around 15.5 N-m with an increase in traverse speed. However, the subsequent peaks remain almost of the same magnitude.

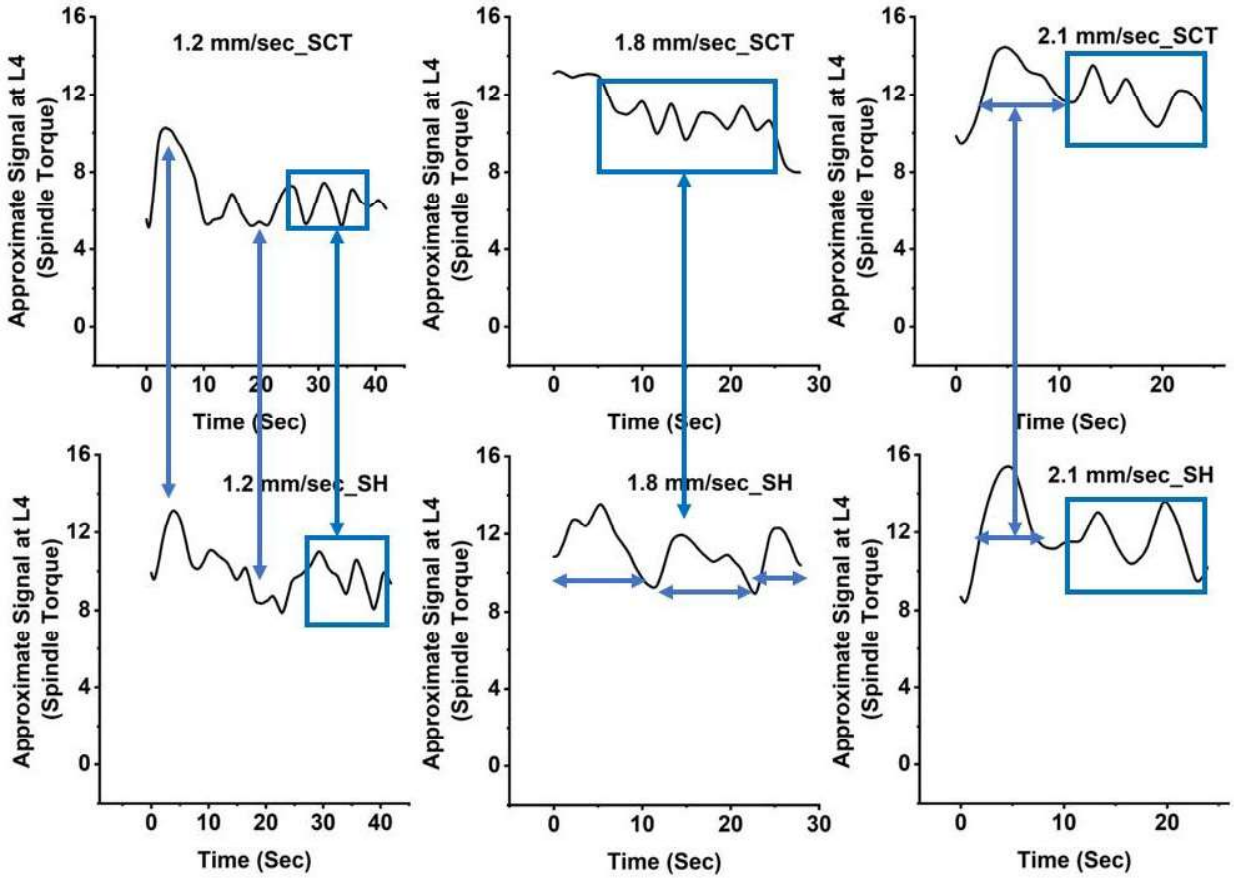

Fig. 6.6 Approximate spindle torque signal at level4 (L4) varying traverse speed

6.3.1.2 Analysis of Sum of Details for Spindle Torque Signal

The analysis of the detail signals of spindle torque shows the fluctuation of high-frequency low-magnitude signal, which was separated from the original torque using DWT. It is evident from Fig. 6.7 that the amplitude of fluctuation for the SH tool is comparatively less than for the SCT tool. This indicates that a more uniform material state has been attained in both advancing and

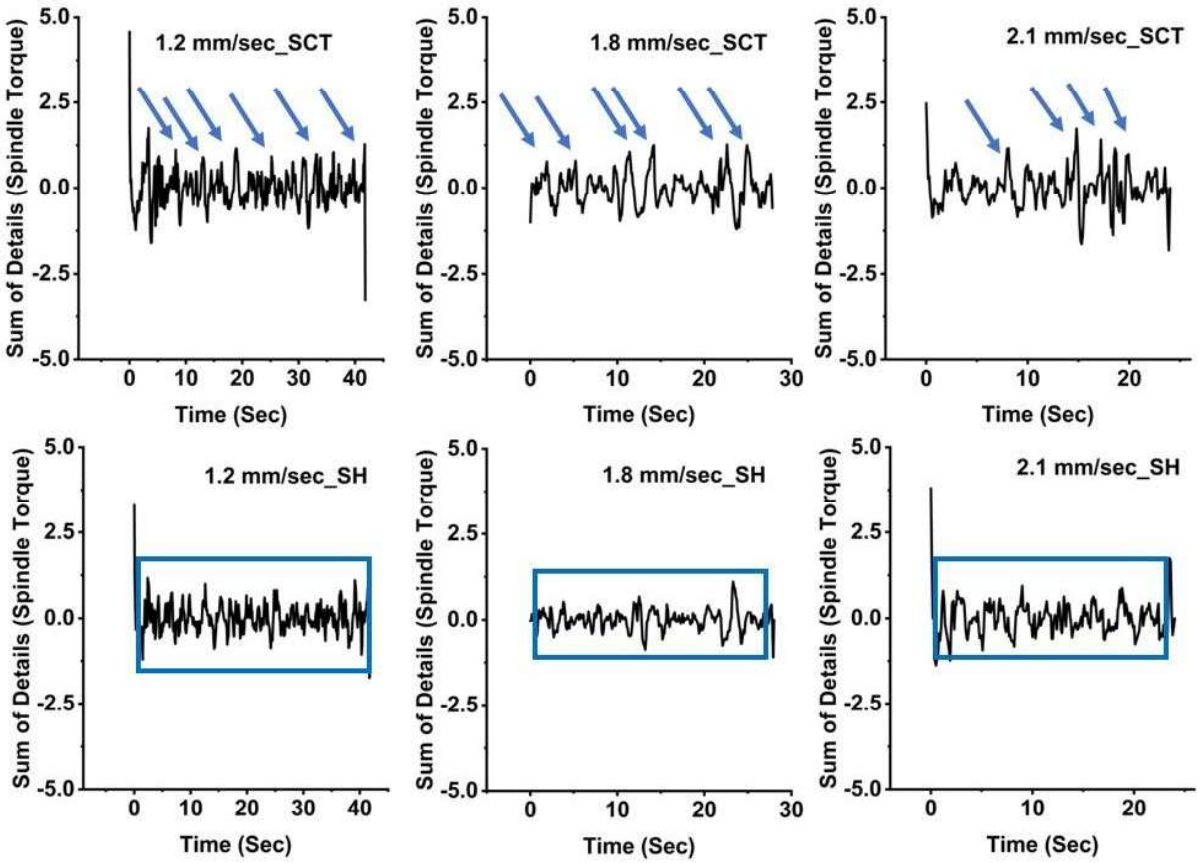

Fig. 6.7 Sum of details signal of spindle torque varying traverse speed

retreating sides by the SH tool, which also indicates less slipping at the tool-workpiece interface. At 1.2 mm/s, the SCT tool shows continuous abrupt changes in fluctuation, which may reflect instability may be due to slipping at the tool-workpiece interface. Compared to all the welding, fluctuation for the SH tool at 1.8 mm/sec (-1 N-m to 1N-m) is the lowest. Such a material state of uniformity is achieved due to optimum heat generation and material mixing.

Figure 6.8 illustrates that the average spindle torque increases as the traverse speed increases. It is due to reduced heat generation from decreased tool-workpiece interaction at higher traverse speeds. Notably, the spindle torque for SH tools rises steadily at a constant rate as traverse speed increases, indicating that SH tools can maintain stable torque at higher speeds. Additionally, regarding the avg. sum of details and the percentage contributed by fluctuations, the avg. sum of details decreases as traverse speed increases. The reduction in percentage contributed of fluctuations is significant at a traverse speed of 1.8 mm/sec. This decline in the contribution

percentage with increasing traverse speed indicates that the detail component of torque (the high-frequency, low-magnitude component) decreases as traverse speed rises.

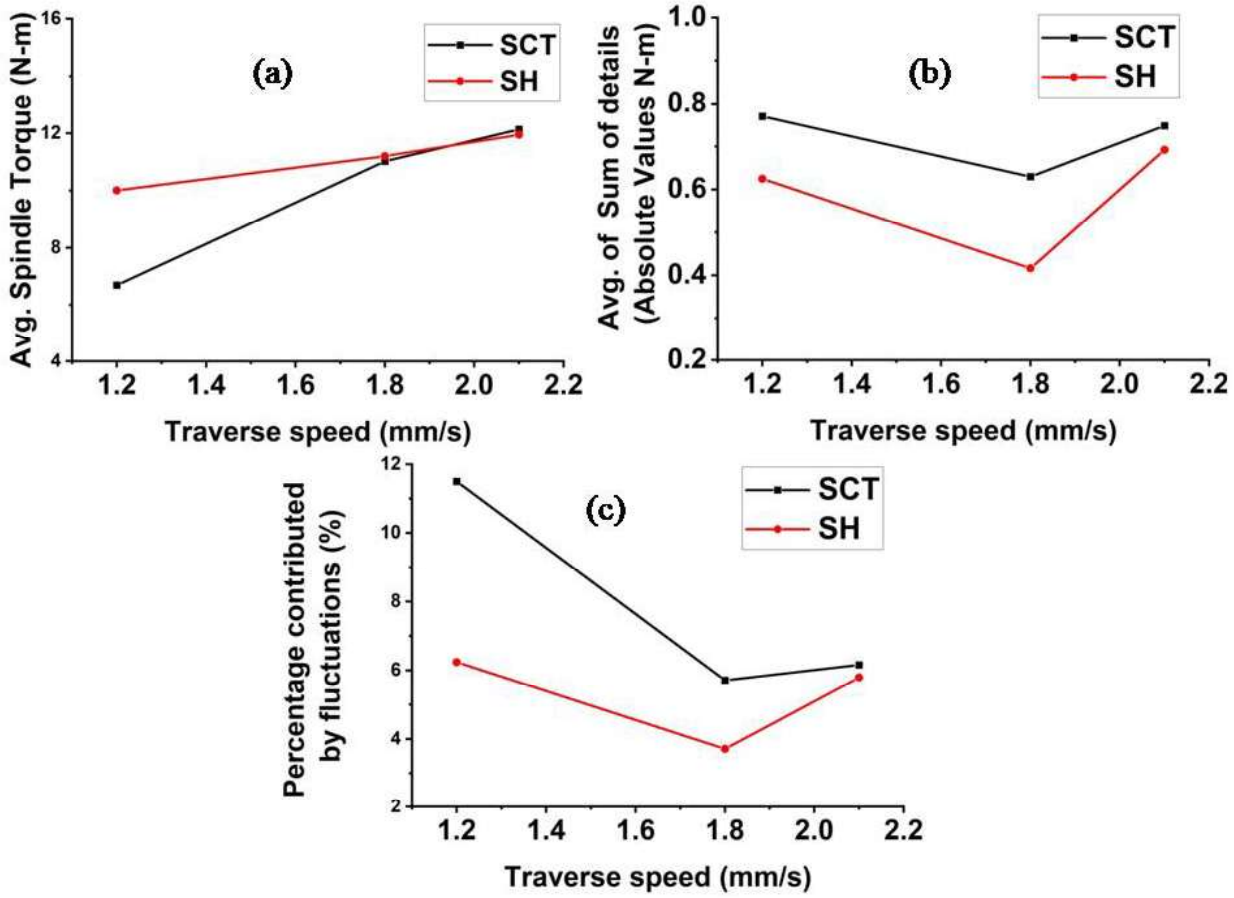

Fig. 6.8 Variation of (a) Avg. spindle torque, (b) Avg. of sum of details (absolute), (c) Percentage contribution by fluctuations for SH and SCT tool with varying traverse speed

6.3.2 Analysis of Z-force

Figure 6.9 shows the original Z-force distribution for SCT and SH tools for varying traverse speeds. At low traverse speed (1.2 mm/sec), the Z-force distribution is accompanied by a higher amount of low-magnitude high-frequency fluctuations for both tools, especially in the SCT tool. Such observation may result from inconsistency in material flow [54][84]. However, as traverse speed increases (1.8 mm/sec, 2.1 mm/sec), these low-magnitude high-frequency fluctuations decreases, and the fluctuations become high magnitude (multiple hundreds of Newton) and occur for a broader period (ranging from 5 to 10 seconds approximately). This wider fluctuation results

in waviness in Z-force distribution, showing a periodic rise and fall of the Z-force, which indicates enhanced dynamic interactions between the tool and the workpiece[85][86]. This waviness becomes prominent at 2.1 mm/sec. These low-magnitudes, high-frequency fluctuations indicate stability between the tool and workpiece, while high-magnitude, low-frequency fluctuations account for material softening.

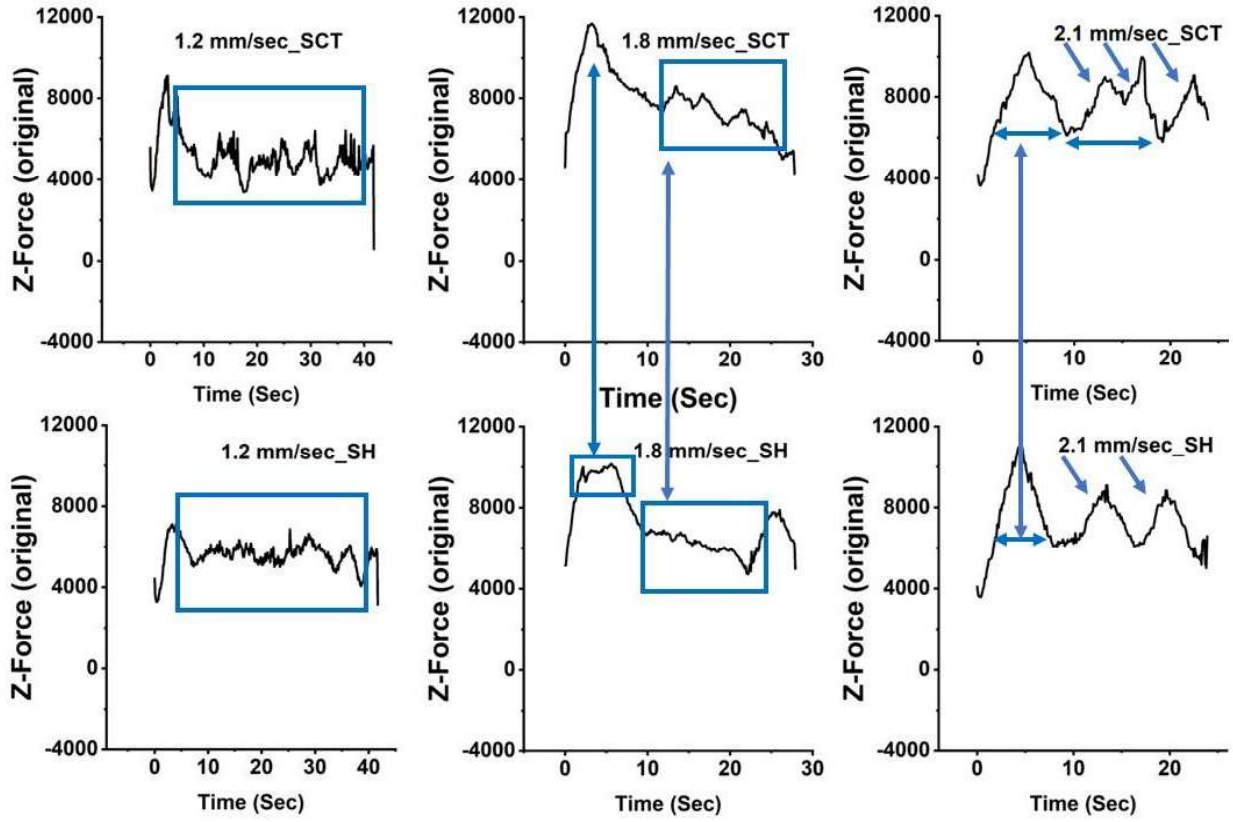

Fig. 6.9 Original Z-force distribution varying traverse speed

6.3.2.1 Analysis of Approximate Z-force Signal

The high magnitude low-frequency part of the Z-force distribution is plotted in Fig. 6.10 (approximate signal) derived using wavelet decomposition. This gross trend of the Z-force distribution shows that the low-frequency high-magnitude fluctuations exist for SCT and SH tools at lower traverse speeds. However, the range of their magnitude is less at 1.2 mm/sec, whereas it increases drastically at 2.1 mm/sec. At 1.8 mm/sec, this waviness is comparatively less than 1.2 mm/sec and 2.1 mm/sec, indicating an optimal traverse speed that enhances thermal and mechanical stability [87][88]. Another important observation is that for 1.8 mm/sec, the

approximate Z-force signal shows a gradual decreasing trend, where the mean trend follows approximately zero slopes for 1.2 mm/sec and 2.1 mm/sec for SCT tool. The gradual decrease in approximate Z-force and less waviness for 1.8 mm/sec shows the material getting softer as the tool traverses further. It may be due to the preheating effect, as FSW is a relatively slower welding process [89]. Meanwhile, as traverse speed increases (2.1 mm/sec), the waviness becomes severe due to a lack of tool-workpiece interaction, increasing the tendency of slipping. This waviness indicates that after a specific period, the tool shoulder loses the grip from the deformed material (approximate signal reduces) and then grips and moves the material from the starting (approximate signal rises). Now, for 1.8 mm/sec, the approximate signal shows the much smoother transition of Z-force for the SH tool, with initially a blunt head. In the SCT tool, the Z-force shows a sharp transition at the beginning of the tool's movement. It shows the SH tool can give a smoother transition at the beginning of the weld, which is attributed to pulsating stirring action and causing much softer material.

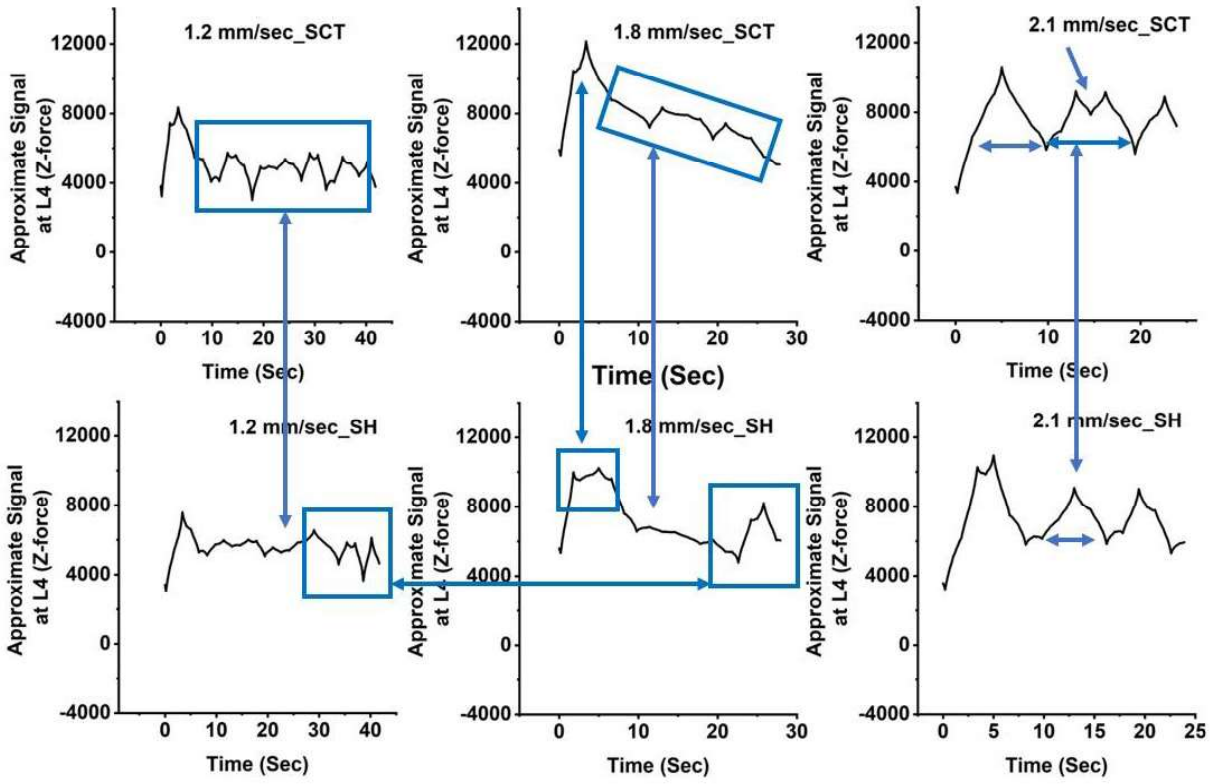

Fig. 6.10 Approximate signal of Z-force at level 4 (L4) varying traverse speed

6.3.2.2 Analysis of Sum of details for Z-Force

For the study of the low magnitude high-frequency components of Z-force, all the detail signals up to four levels were added and presented here in Fig. 6.11. As discussed earlier it is more evident that the high-frequency low magnitude components (detail signal) are higher for lower traverse speed (1.2 mm/sec) for both tools and reduces at 1.8 mm/sec. But when traverse speed rises to 2.1 mm/sec, the details signal further increases. The fluctuation amplitude also follows the same trend, where at 1.8 mm/sec, the amplitude is minimum for both tools. This shows that more uniformity in material state is attained in the weld's advancing and retreating sides for 1.8 mm/sec. Compared to the SCT tool, the SH tool's performance is better, where it attains a lower amplitude of fluctuations irrespective of traverse speed.

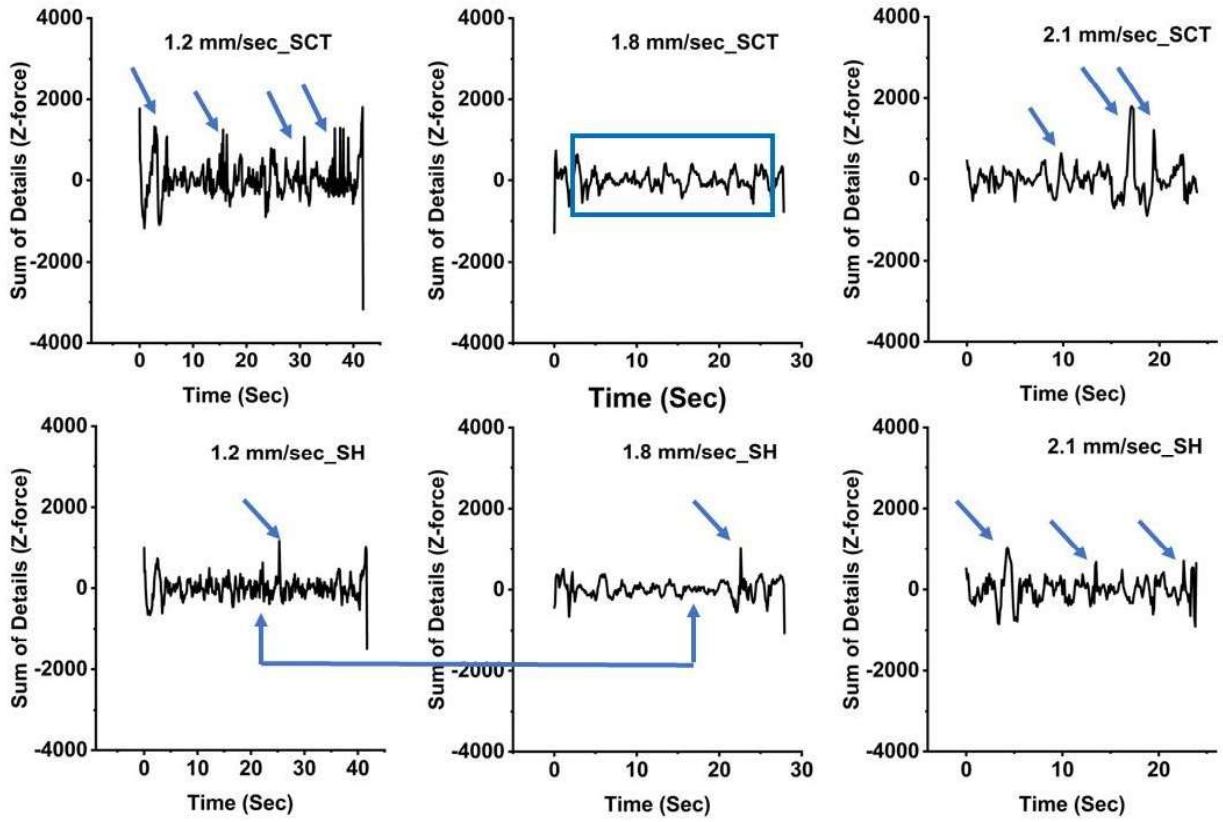

Fig. 6.11 Sum of details signal for Z-force varying traverse speed

Fig. 6.12 represents the avg. values of Z-force, sum of details, and percentage contributed by fluctuation for Z-force. The overall trends are almost similar to the observation for spindle torque (Fig. 6.8) with a gradual rise, and a similar phenomenon is also pertinent here. Z-force deformed

the material in a vertical direction and consolidated the material below the tool shoulder. At 1.8 mm/s, avg. sum of details and its percentage contribution by fluctuation (Fig. 6.12b, c) have been lowest for both the tools and also no abrupt change in the avg. original Z-force is observed which also indicates the uniform deformation below the tool shoulder due to low slipping tendency. Further, it can be seen that at 1.8 mm/s effect of pin geometries has an insignificant effect.

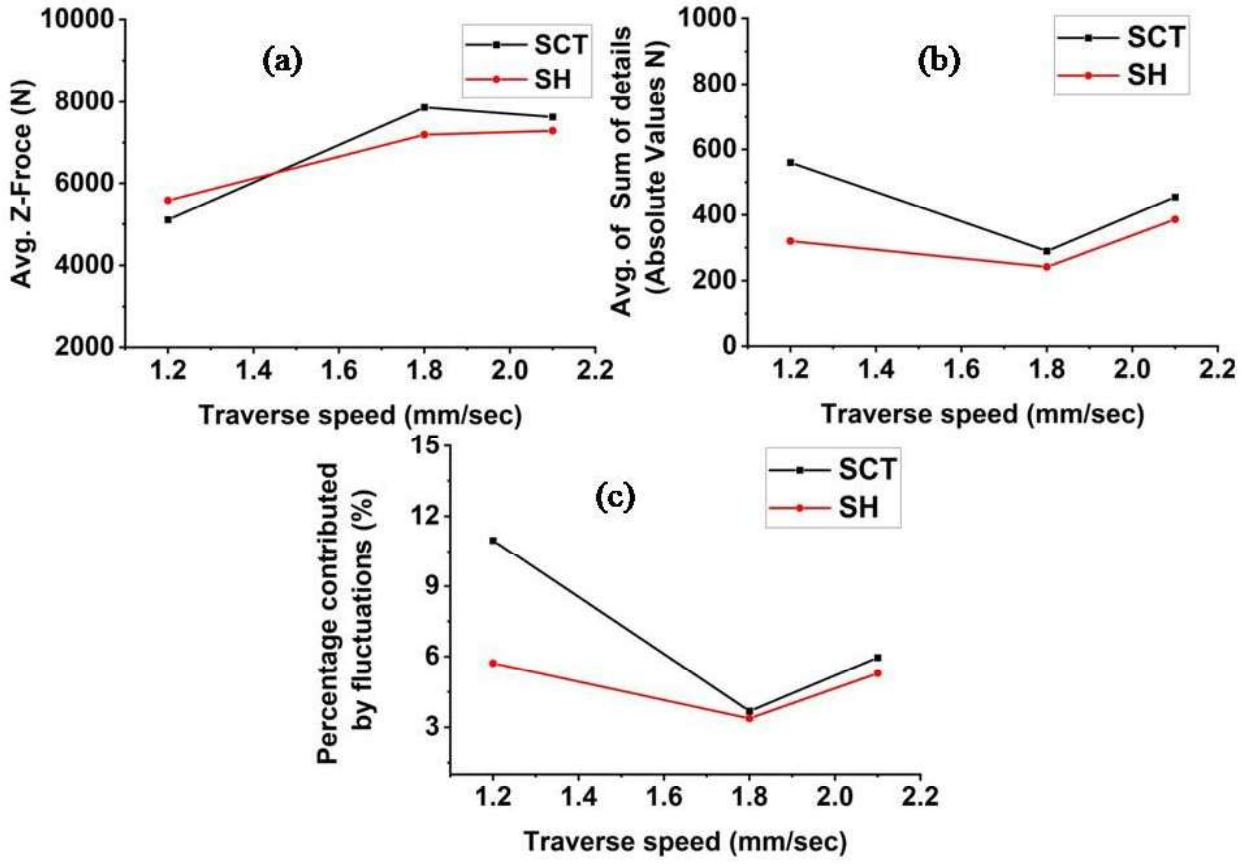

Fig. 6.12 Variation of (a) Avg. Z-force, (b) Avg. of sum of details (absolute), (c) Percentage contribution by fluctuations for SH and SCT tool with varying traverse speed.

6.3.3 Bead Surface Analysis

Fluctuations in sum of details of spindle torque and Z-force may be an indicator of bead surface morphology for welding as shown in Fig. 6.13 and Fig. 6.14. At a low traverse speed, both tools show higher fluctuations, which directly correlate with the rough surface of the bead. This is especially true for the SCT tool (1.2 mm/s), where the sum of details signals shows excessive fluctuations with sudden hikes, and the bead surface shows a poor texture with surface voids.

Furthermore, signals with comparatively low amplitude fluctuations show better surface texture for both tools (1.8 mm/s and 2.1 mm/s). Figures 6.13 and 6.14 also show that fluctuations for the SH tool are lower than for the SCT tool, and the SH tool also shows a better surface finish than the SCT tool. The SH tool has minimum fluctuations at 1.8 mm/s, possibly due to better material flow over the top surface and shows a better surface finish. Observations are more precise in Fig. 6.15, where a magnified view of surface beads is shown.

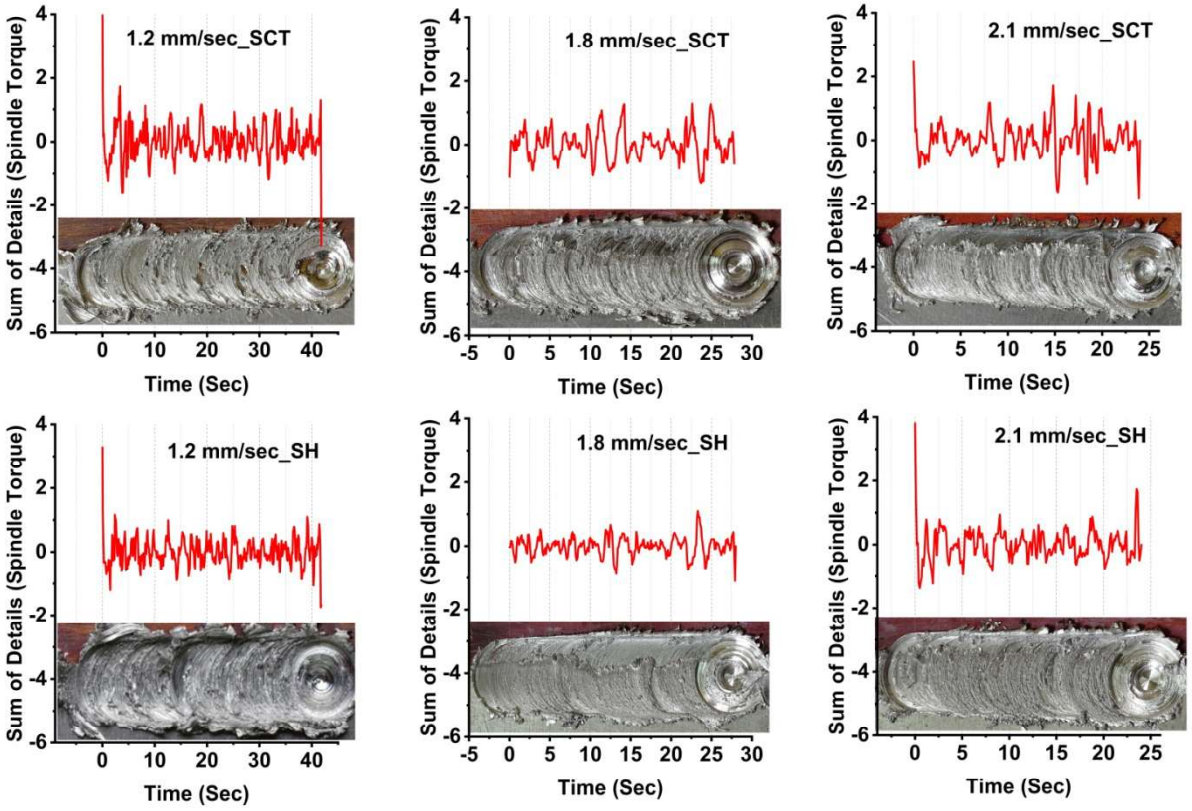

Fig. 6.13 Variation in weld bead appearance with respect to Sum of details (spindle torque) for SCT and SH tool varying traverse speed

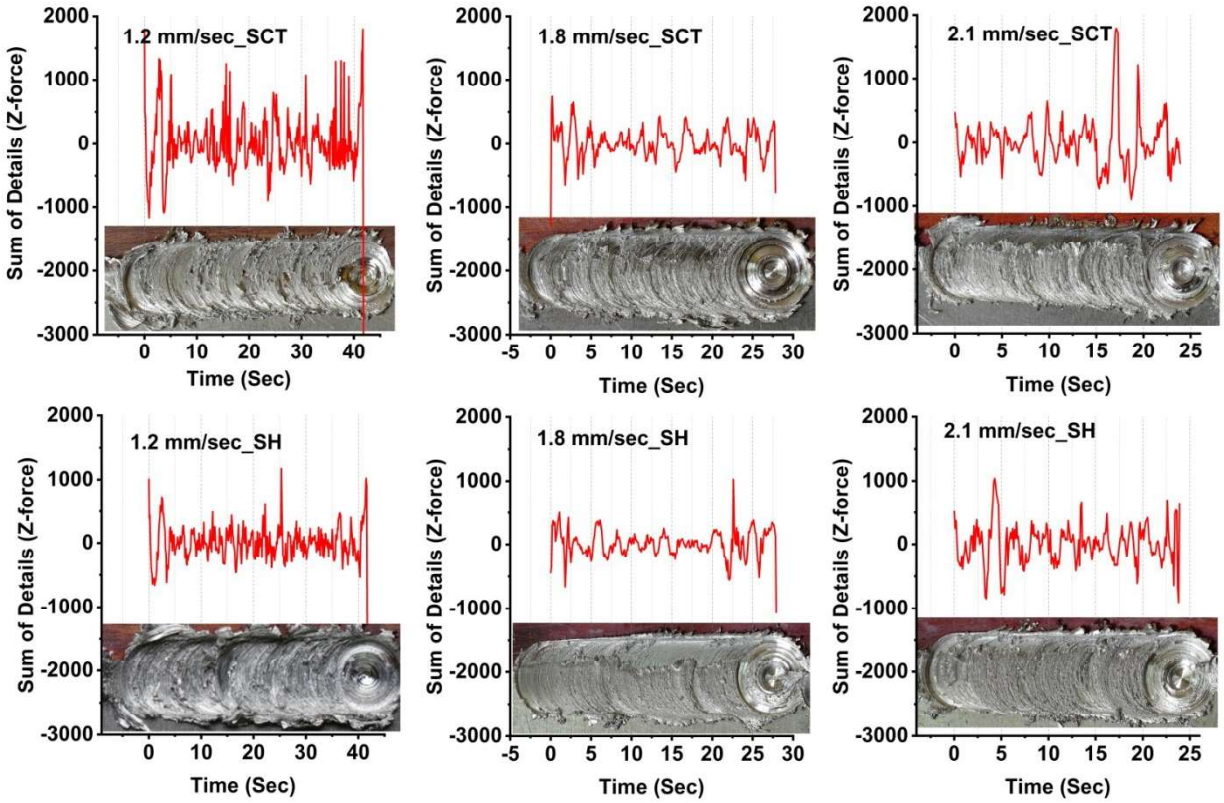

Fig. 6.14 Variation in weld bead appearance with respect to Sum of details (Z-force) for SCT and SH tool varying traverse speed

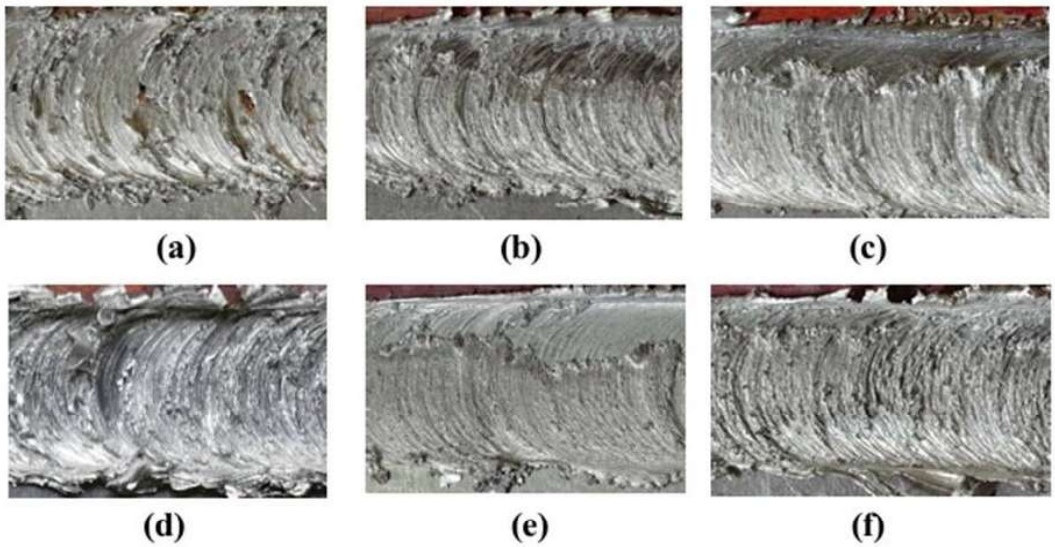

Fig. 6.15 Magnified view of surface beads of varying traverse speed- SCT tool (a) 1.2 mm/s (b) 1.8 mm/s (c) 2.1 mm/s and SH tool (d) 1.2 mm/s (e) 1.8 mm/s (c) 2.1 mm/s

6.3.4 Macrostructure Analysis

The macrostructure of a cross-section of the welding joint has revealed the different material flow for SH and SCT tools in Fig. 18, 19. At 1.2 mm/s, SCT tool shows (Fig. 6.16a) few Cu infused at stir zone and void due to poor material mixing. It is attributed due to excessive slipping at tool-workpiece interface. The signal distribution shows a sudden drop of approximate signal at 1.2 mm/s (Fig. 6.6 and Fig. 6.10), which can be measured by less material flow at the stir zone, and abrupt fluctuations at the sum of details (Fig. 6.7 and Fig. 6.11) can directly relate to this improper material mixing phenomenon. At 1.8 mm/s, the SCT tool shows (Fig. 6.16b) better material mixing where Cu was infused into a stir zone in the form of small particles due to better mechanical and thermal stability at stir zone [27][25], which can be correlated with stability in approximate signal and reduction in the fluctuation of sum of detail signal. At 2.1 mm/s, the SCT tool also shows (Fig. 6.16c) good material mixing at the stir zone, and almost a pattern of signal distribution in approximate signal and detail signal was observed, like 1.8 mm/s of traverse speed.

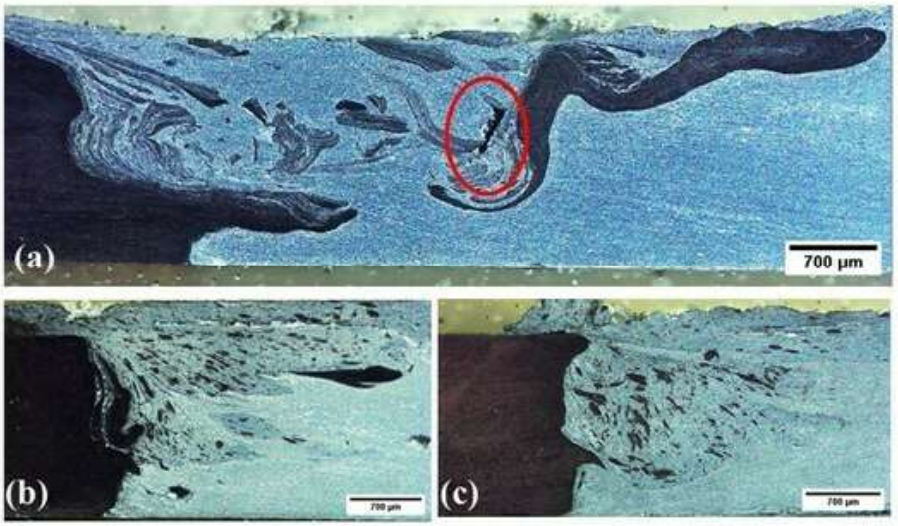

Fig. 6.16 Macrostructure of stir zone for SH tool (a) 1.2 mm/s, (b) 1.8 mm/s (c) 2.1 mm/s

However, for SH tool, at 1.2 mm/s, lamellae (Fig. 6.17a) were observed with a few Cu chunks at stir zone, which signifies better material mixing. It was also observed that signal at 1.2 mm/s shows an initial drop of magnitude of approximate signal. However, it is much less than the SCT tool. Stability in approximate signals and less fluctuation than SCT tool in the sum of details

signals indicate better material flow and homogeneity in the stir zone. At 1.8 mm/s, the macrostructure shows (Fig. 6.17b) a fine distribution of Cu particles because of adequate heat generation and pulsating stirring action by the SH tool at stir zone SH tool [48]. It can also be understood well by the signal distribution, where the approximate signal of spindle torque and Z-force shows smoothness in signal pattern and no abrupt signal fluctuations. Furthermore, the sum of details shows the minimum amplitude of fluctuations. At 2.1 mm/s, macrostructure observation revealed (Fig. 6.17c) better material deformation mixing where small Cu was infused uniformly at the stir zone. Almost similar trends of 1.8 mm/s are observed in the approximate and detail signal distributions, ensuring improved mixing and stability in the stir zone.

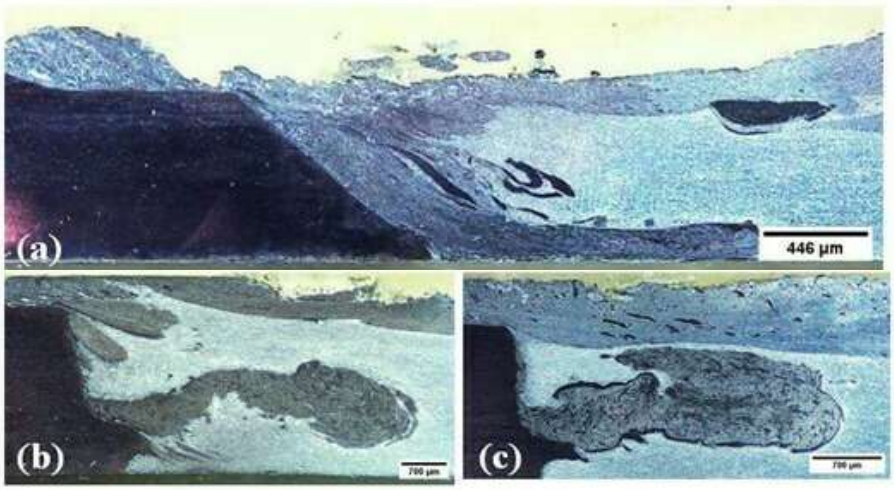

Fig. 6.17 Macrostructure of stir zone for SCT tool (a) 1.2 mm/s, (b) 1.8 mm/s (c) 2.1 mm/s

6.3.5 Tensile Strength and Failure Analysis

Figure 6.18 presents variations of UTS, YS and percentage of elongation for varying traverse speed. Table 6.1 shows the UTS and YS for varying traverse speed for two different tools. From the pattern, a more stip increase in tensile strength is achieved from 1.2 mm/s to 1.8 mm/s for the SCT tool, though an increase is also observed for the SH tool, but comparatively less stip. This shows the SH tools can provide comparatively higher tensile strength even at lower traverse speeds. Tensile strengths are governed by material mixing, grain size, formation of intermetallics, etc. [23][42][48]. At 1.2 mm/s, the macrostructure of weld cross section of SCT

tool shows poor material mixing with void at the stir zone, drastically affecting tensile strength (30.1 MPa). A significant amount of tool-workpiece slipping occurred at a speed of 1.2 mm/s for the SCT tool, resulting in incomplete material movement during welding. It was analyzed by the drop in approximate signal and abrupt fluctuations in detail signals (Fig. 6.6, 6.7 and 6.10, 6.11). It was also observed that the percentage contributed by fluctuations (Fig. 10 and 14) at 1.2 mm/s, was the highest for SCT tool. However, in the case of the SH tool at 1.2 mm/s, a different observation is made; a better tensile strength was achieved (81.4 MPa) due to a good amount of material mixing, showing a lamellar structure at the stir zone (Fig. 19a). It was also observed that the percentage of fluctuations is significantly lower than in the SCT tool. When the traverse speed reaches 1.8 mm/s, UTS for the SCT tool drastically increases (80.2 MPa) as the SCT tool due to better material mixing at the stir zone. Furthermore, The SH tool demonstrates the highest tensile strength (93.4 MPa) among all the welding at 1.8 mm/s because of the fine distribution of Cu particles at the stir zone. This indicates a good amount of mixing because of adequate heat generation and effective stirring action by the tool. It was also noticed that percentage contributed by fluctuations lower for both the tools whereas SH tool exhibited lowest compared to all welding. At 2.1 mm/s, both tools show a better mixing at the stir zone (Fig. 18c and 19c) which results decent tensile strength for both tools (SH-71.7 MPa and SCT-72.6 MPa). Whenever the tensile strength increases or decreases, it may be due to better mixing or may be excessive slipping; the percentage contributed by fluctuations shows an exciting trend. At 1.8 mm/s, the SH tool shows the highest UTS, where this is minimal. On the contrary, the SCT tool exhibits the lowest UTS at 1.2 mm/s, where the percentage of fluctuations is the highest. Based on this discussion, the percentage contributed by fluctuations in signals may be a good indicator of weld quality.

Table 6.1 Yield strength (YS) and ultimate tensile strength (UTS) for different traverse speeds

Exp. No.	Tool	Traverse speed (mm/s)	Rotational speed(rpm)	YS (MPa)	UTS (MPa)
1	SH	1.2 mm/s	1000	81.4	81.4
2	SH	1.8 mm/s	1000	93.4	93.4
3	SH	2.1 mm/s	1000	69.9	71.7
4	SCT	1.2 mm/s	1000	16.32	30.1
5	SCT	1.8 mm/s	1000	79.2	80.2
6	SCT	2.1 mm/s	1000	69.1	72.6

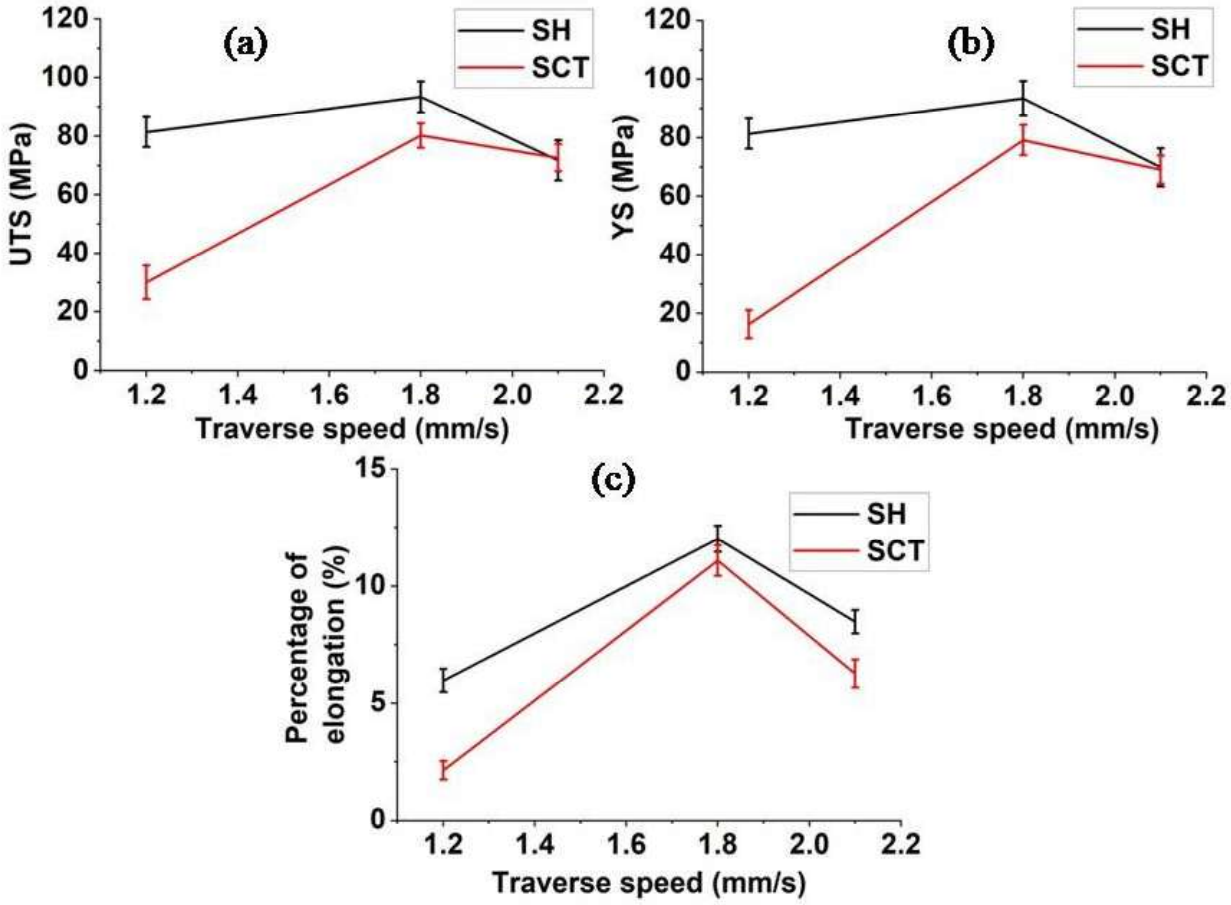

Fig. 6.18 Variation of (a) UTS, (b) YS and (c) percentage of elongation with traverse speed for SH and SCT tool

6.4 Analysis of Signals for Varying Rotational Speed

6.4.1 Analysis of Spindle Torque

Figure 6.19 represents the change of spindle torque for SH and SCT tools with time. Figure 6.19 shows that the spindle torque distribution is getting more uniform with a rise in rotational speed. However, the extent of uniformity achieved for the SH tool compared to the SCT tool is different. At 800 rpm SH tool initially shows a more uniform and higher torque (approximately 14 N-m); however, in traverse of around 15 seconds, it loses the uniformity and shows significant fluctuations. In contrast, the SCT tool shows significant fluctuations from the beginning to the end of welding. As the tool rotational speed increases to 1000 rpm, the SH tool

attains a non-uniform spindle torque with periodic hikes, showing that the SH tool tries to achieve stable spindle torque. The trend for the SCT tool remains more or less similar, with some fewer spikes, which may be attributed to increasing heat due to an increase in rotational speed. At 1200 rpm, the extent of non-uniformity reduces for both tools (Fig. 6.19a, b). At 1400 rpm, both tools attain a significant uniform torque distribution, which may be attributed to enhanced

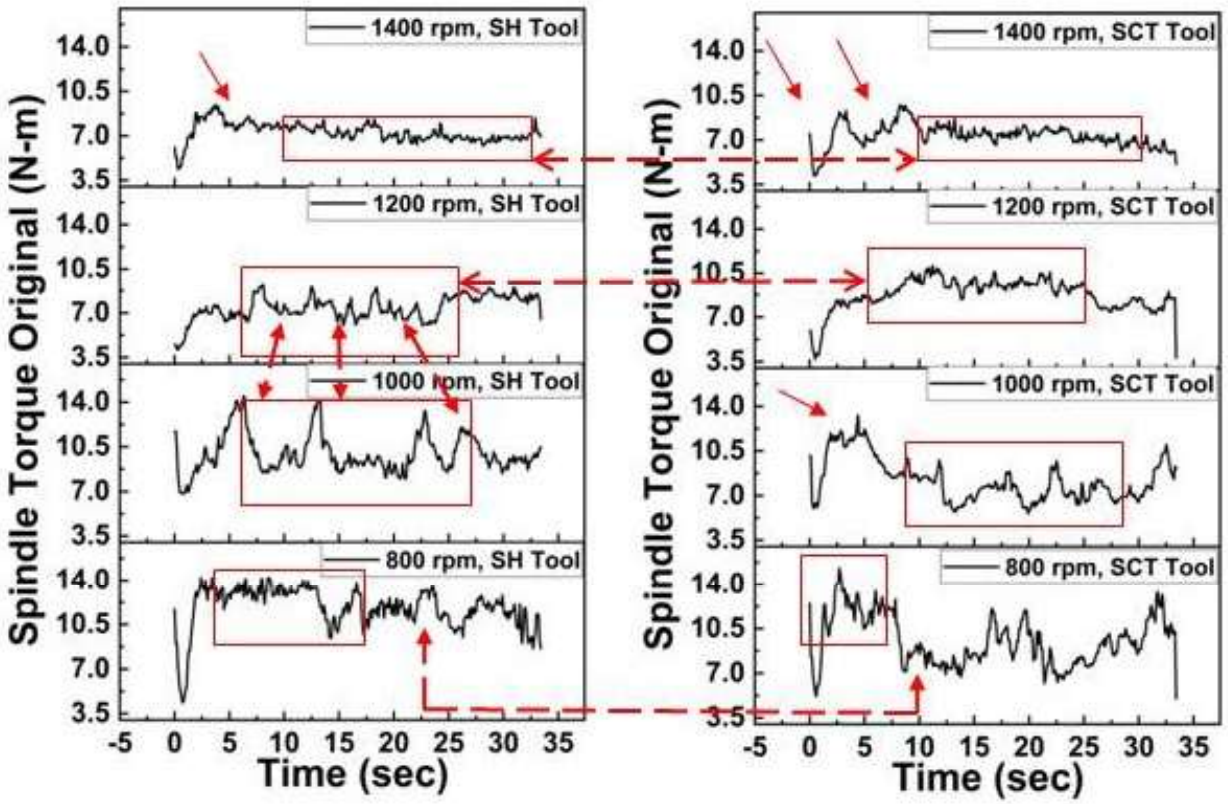

(a) (b)

Fig. 6.19 Original spindle torque distribution (a) SH tool, (b) SCT tool

deformation, which causes higher heat generation. However, the SCT tool shows some fluctuations initially, as marked compared to the SH tool. So it can be stated that the SH tool attains a more consistent spindle torque than the SCT tool for a given rotational speed. For further analysis of spindle torques, the relevant information has been extracted as approximate and detailed signals with the help of DWT.

6.4.1.1 Analysis of Approximate Spindle Torque Signal

The approximate signal (Fig.6.20) represents a gross pattern of the spindle torque for both tools. At 800 rpm, the approximate spindle signal for the SCT tool shows a very non-uniform distribution with a 'W' shape pattern formed due to the gradual fall of the approximate spindle torque signal periodically. At 1000 rpm, also approximate spindle torque signal for the SCT tool shows an almost similar pattern but with a low magnitude of the 'W' pattern. However, for the SH tool, the 'W' shape pattern's magnitude increases and shifts its position to the middle, as marked in Fig. 6.20a. This shows increasing rotational speed from 800 rpm to 1000 rpm, the distribution of overall spindle torque gets disturbed. This may be attributed to the tool slipping due to increased pulsating action at comparatively lower heat input and deformation for the SH tool. At 1200 rpm the approximate spindle torque signal is more uniform with a little exception

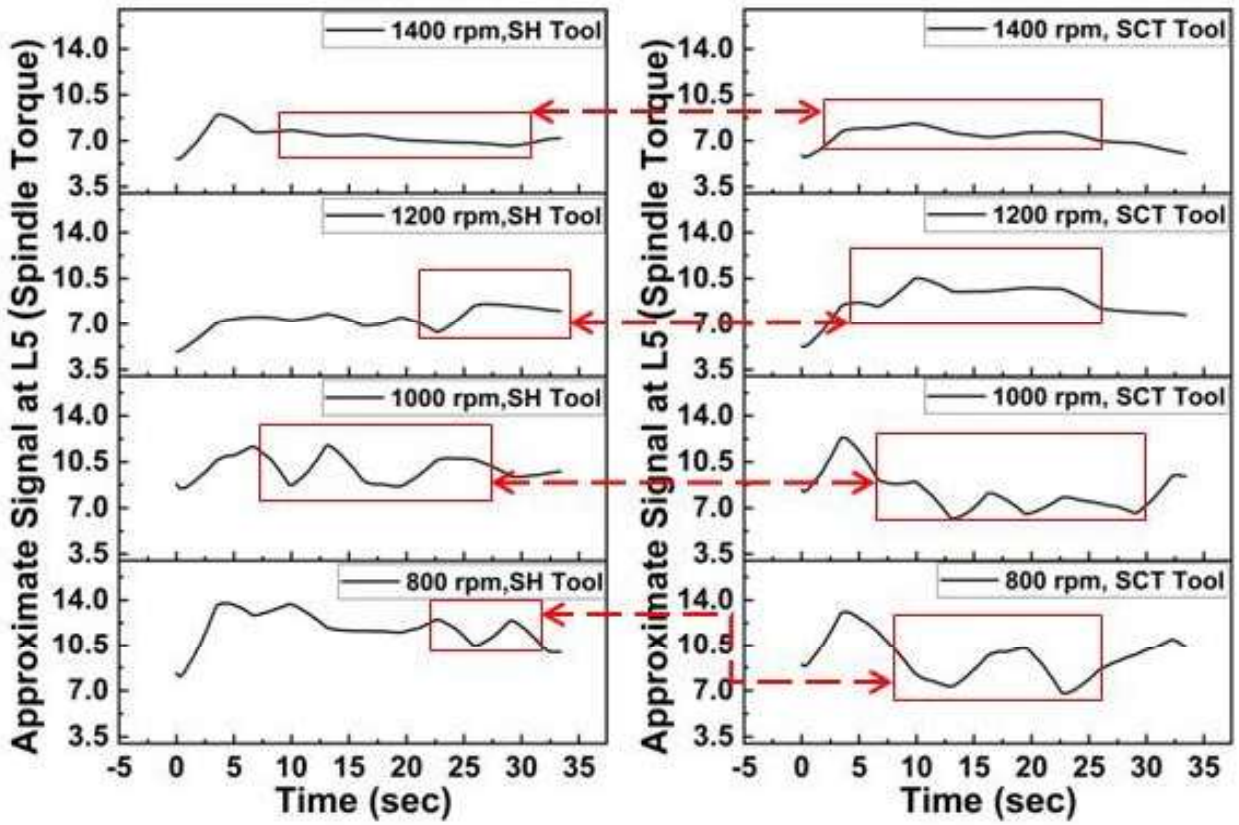

(a) (b)

Fig. 6.20 Approximate signal for spindle torque at level 5 (L5) (a) SH tool, (b) SCT tool

at the end, where a slight increase has been seen. At 1400 rpm, a further uniform approximate signal is obtained for the SH tool. This uniformity at higher rotational speed (1200 rpm, 1400 rpm) for the SH tool can be attributed to a higher pulsating action and increased frictional heat input. A similar observation has also been made for the SCT tool, where the approximate spindle torque signal is more uniform at 1200 rpm and 1400 rpm. However, at 1200 rpm the increase in approximate signal has been more for the SCT tool than for the SH (10.5 N-m approximately) tool, implying the deformation of the stir zone achieved by the SH tool is greater.

6.4.1.2 Analysis of Sum of Details for Spindle Torque Signal

In detail spindle torque signal, an effort is made to capture the frequent changes in spindle torque. Fig. 6.21shows that the frequency amplitude decreased as rotational speed increased for both tools, and it can be caused by enhanced heat input. Moreover, such a decrease also indicates that at higher tool rotational speed, more similarity is achieved by the advancing and retreating side in terms of material state [90]. So, it means higher fluctuation may be stated as a disorder in spindle torque distribution. However, at 1400 rpm approximate signal is more uniform, and also, fluctuations in the sum of details are close to uniform. So, it may cause better mixing as well as higher tensile strength at 1400 rpm.

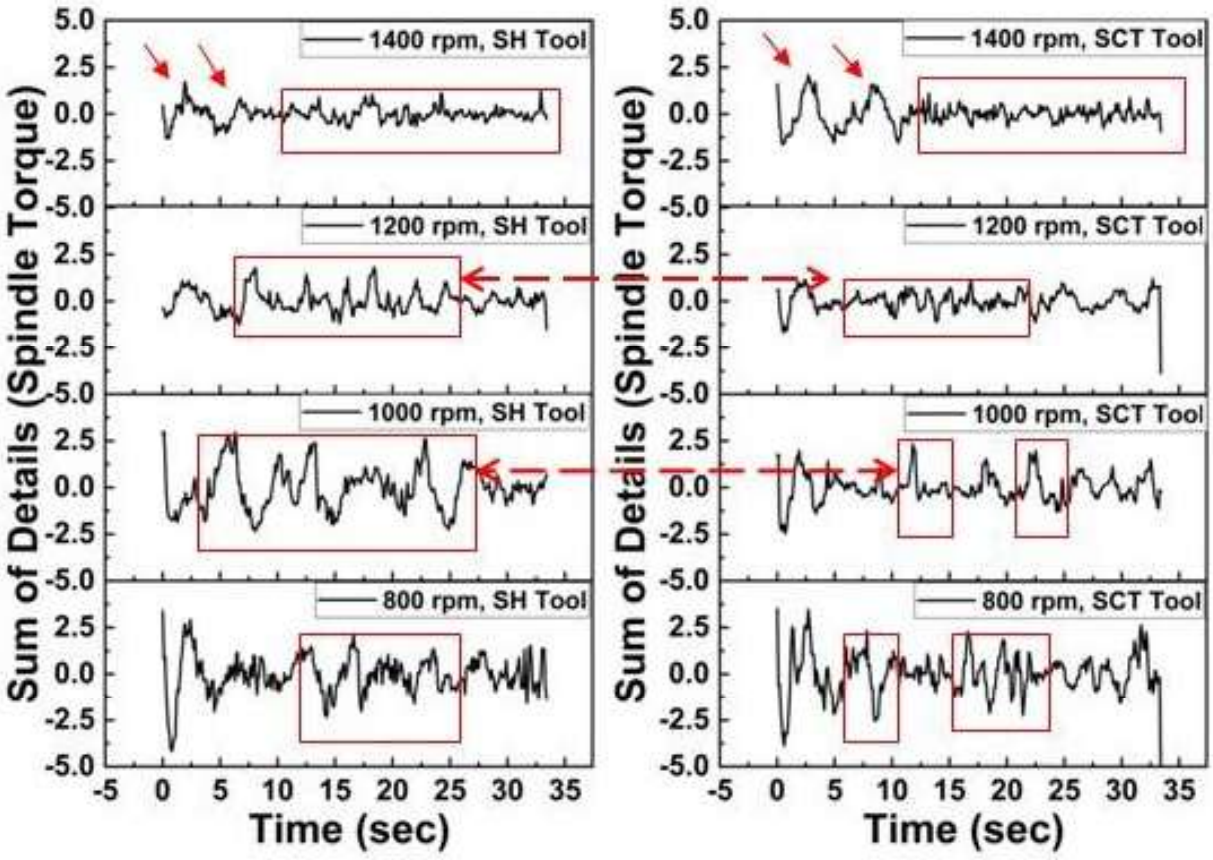

(a) (b)

Fig. 6.21 Sum of details signal for spindle torque (a) SH tool, (b) SCT tool

Figure 6.22 represents the avg. values of spindle torque, sum of details and percentage contribution by fluctuation. The overall trend of all these quantities shows a decreasing trend as rotational speed increases and can be endorsed by the increased heat input and deformation. However, in Fig. 6.22a at 1200 rpm a sudden rise in spindle torque is observed for the SCT tool. Similarly, a sudden increase has been seen at 1000 rpm for avg.sum of details and its percentage contribution by fluctuation (Fig. 6.22b, c) for the SH tool also. Any increase in spindle torque values in any form represents a higher resistance to angular deformation by the workpiece. However, this may have different implications on welding as the sum of details is a smaller fraction of total spindle torque. At 1400 rpm, the avg. spindle torque for both tools shows no difference, implying that the contribution of pin geometry variation to avg. spindle torque has been nullified at a higher rotational speed. It may be due to the workpiece being highly

plasticized at higher rotational speed [24]. However, the difference in sum of details is quite evident here. At 1400 rpm the sum of details for SH tool reduces gradually, whereas the SCT tool shows an increment.

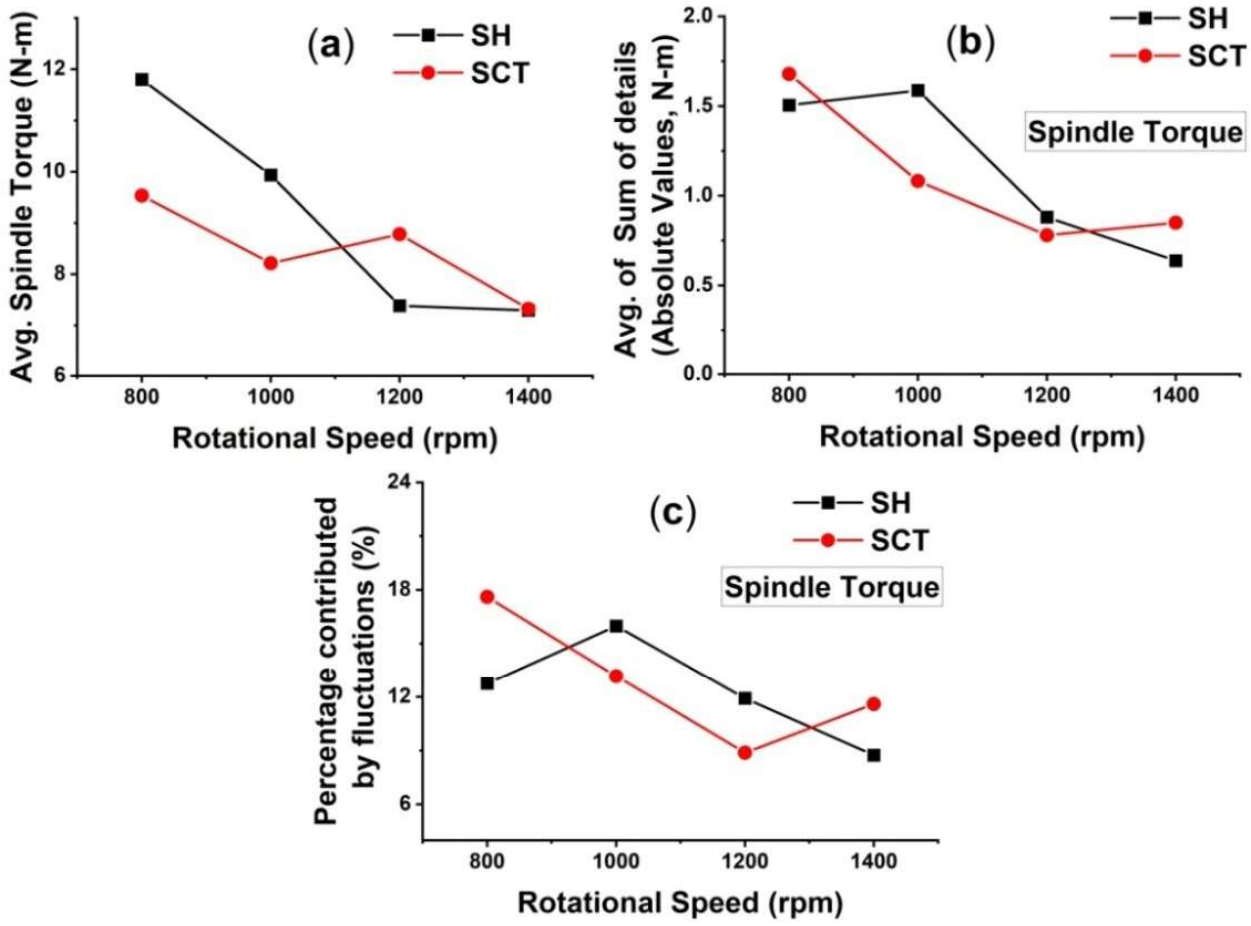

Fig. 6.22 Variation of (a) Avg. spindle torque, (b) Avg. of sum of details (absolute), (c) Percentage contribution by fluctuation for SH and SCT tool with rotational speed

6.4.2 Analysis of Z-Force

From the above Fig. 6.23, it has been seen that instability has decreased gradually with rise in tool rotational speed for both tools except 1200 rpm for the SCT tool, as similar phenomenon is observed for spindle torque also. At 800 rpm, both tools show a significant instability in Z-force distribution. However, for the SCT tool, the fluctuations are encountered with spikes. A similar pattern is also observed for 1000 rpm for SCT tool. However, only instability has increased for the SH tool at 1000 rpm. This may be attributed to the tool slipping due to an increase in

pulsating action with an increase in rotational speed. Whereas for 1200 rpm the magnitude of such fluctuations decreased significantly, which has also been seen for 1400 rpm for the SH tool. But for the SCT tool, a gradual increase is attained for a significant period at 1200 rpm before it reaches some stability for a short period. This shows the inability of the SCT tool to provide a consistent Z-force though the rotational speed has increased significantly. Moreover, the amount of Z-force achieved for SCT tool is 9000 N, whereas it is only around 6000 N for the SH tool. At 1400 rpm, the distribution of Z-force pattern follows a more or less similar pattern. However, a few spikes have been observed as marked for the SCT tool.

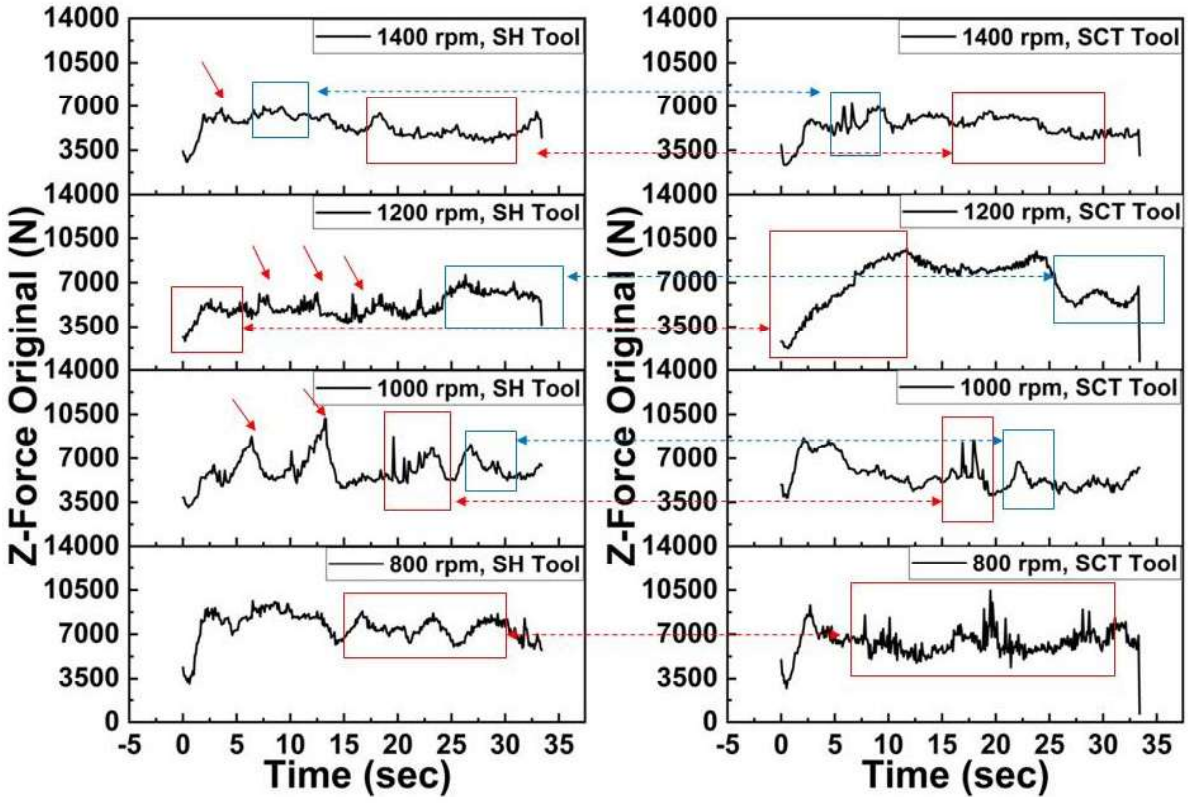

(a) (b)

Fig. 6.23 Original Z-force distribution (a) SH tool, (b) SCT tool

6.4.2.1 Analysis of Approximate Z-force Signal

The observation for approximate Z-force signal (Fig. 6.24) is more or less similar, except it shows a more evident Z-force trend. The above diagram shows that none of the tools have a

stable Z-force distribution other than SH tool at 1400 rpm. At 1400 rpm SH tool shows a regular trend of Z-force distribution with an initial hike and gradual decrease in Z-force, which can be attributed to plate preheating [16].

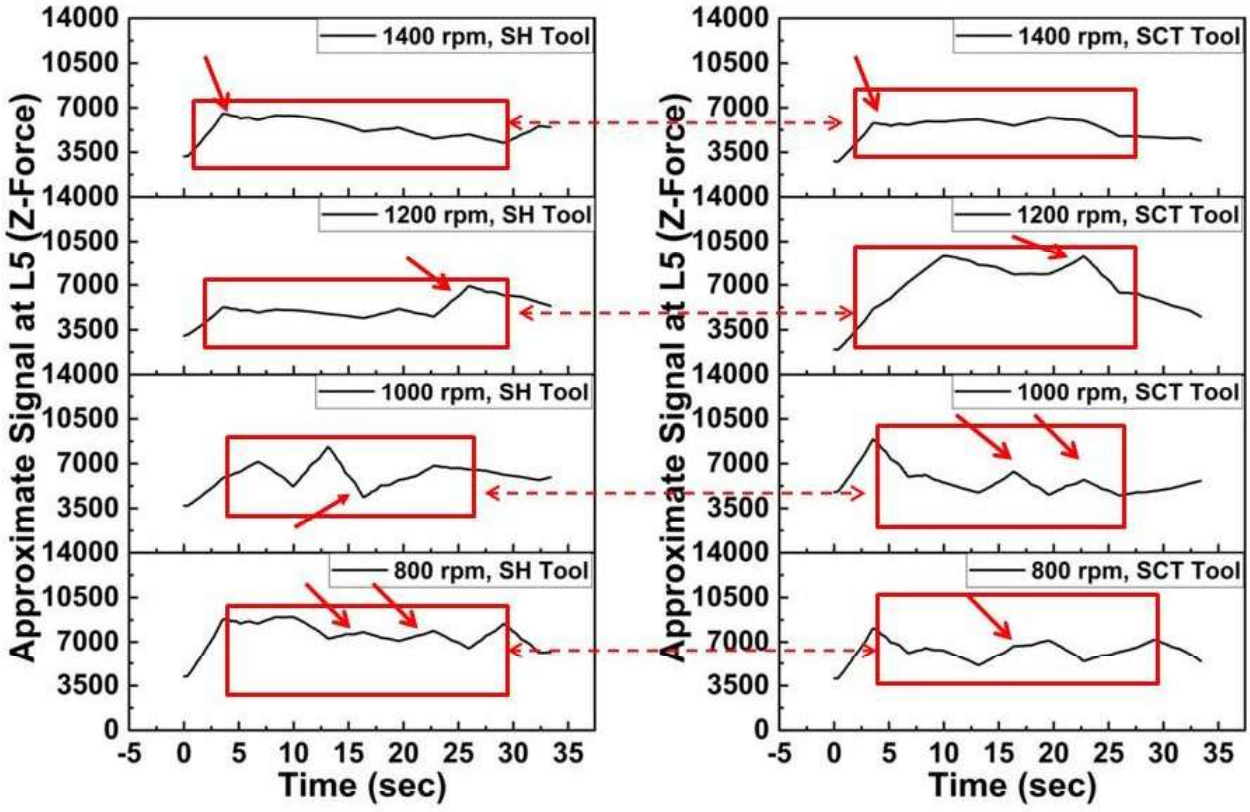

(a) (b)

Fig. 6.24 Approximate signal for Z-force at level 5 (L5) (a) SH tool, (b) SCT tool

6.4.2.2 Analysis of Sum of Details for Z-force

The fluctuations in Z-force distribution have been captured separately in Fig. 6.25 as the sum of details of Z-force. It resembles that as tool rotational speed increases, the fluctuation in Z-force reduces. The magnitude of fluctuation for SH tool is more compared to SCT tool and can be attributed to the pulsating action of the flat faces [48] of the SH tool. At 800 rpm, the SCT tool shows spikes with fluctuations, whereas only fluctuations are observed for the SH tool. As rotational speed increases to 1000 rpm, the SH tool also shows the spikes behavior. The SCT tool shows an approximately similar distribution at 1000 rpm as that for 800 rpm with moderate

spikes and may be attributed to increased heat input. Slip at the tool-workpiece interface may affect such high fluctuations at a lower rotational speed. At 1200 rpm, the SCT tool attains less fluctuation, whereas the SH tool still attains a significant fluctuation at regular intervals. At 1400 rpm both tools attain least amount of fluctuations. The SCT tool initially shows some fluctuations with small spikes, which diminish to least significant later. A moderate amount of fluctuation has been continued for the SH tool throughout welding. The spindle torque is the resistance offered by workpiece under consideration of angular deformation incorporated by the tool. Whereas the Z-force is the resistance by the workpiece to the deformation in a vertical direction [71]. The tool shoulder mostly employs Z-force on the workpiece at tool shoulder-workpiece interface. Hence a detailed analysis of different components (approximate and detail signals) of Z-force and torque may reveal important aspects of microstructure formation.

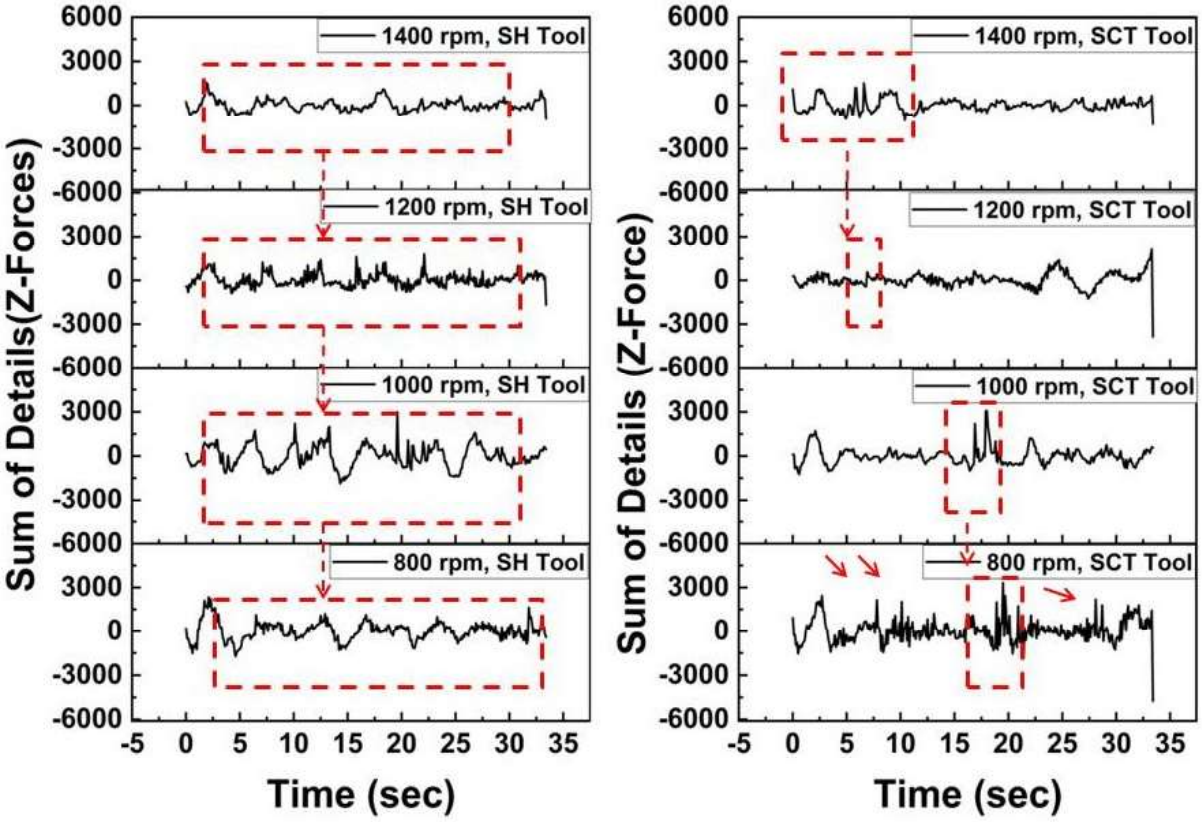

(a) (b)

Fig. 6.25 Sum of details signal for Z-force (a) SH tool, (b) SCT tool

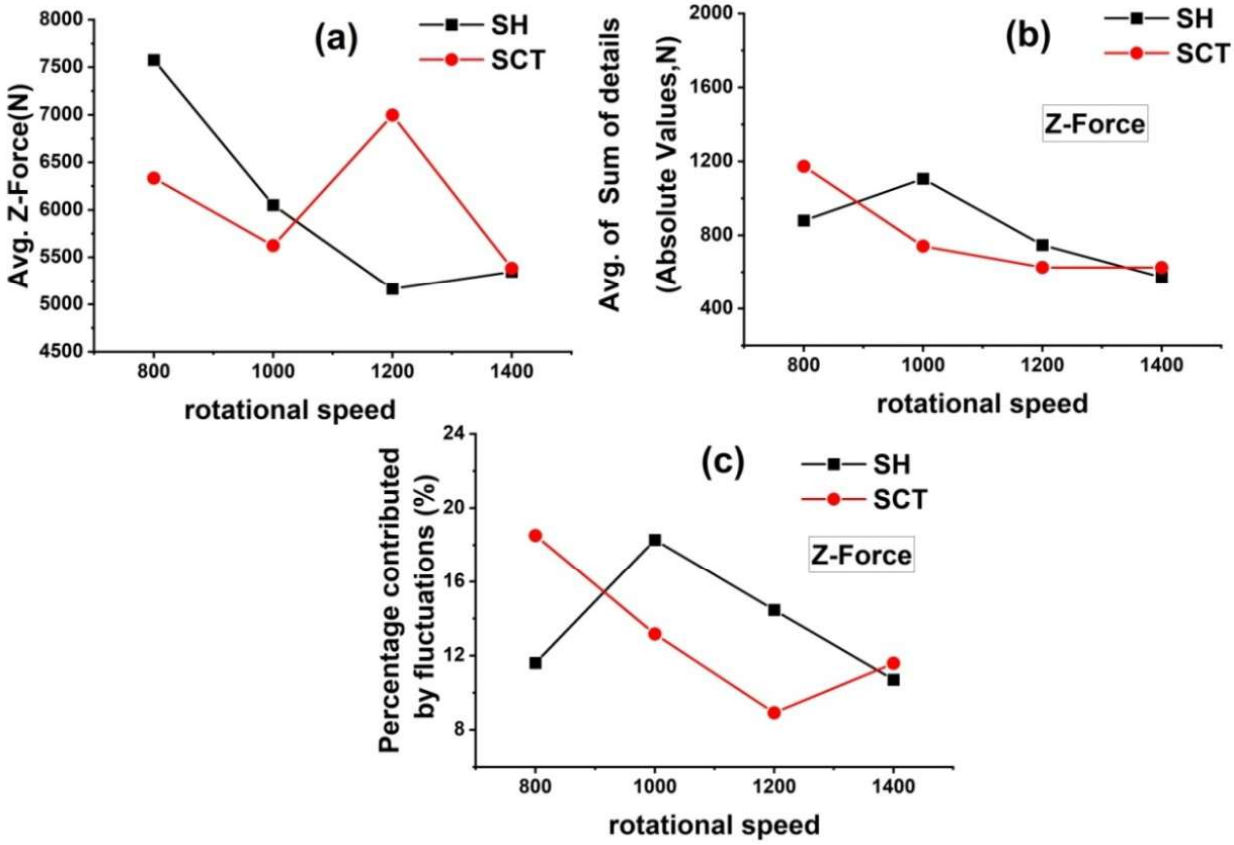

Fig. 6.26 Variation of (a) Avg. Z-force, (b) Avg. sum of details (absolute), (c) Percentage contribution by fluctuation for SH and SCT tool with rotational speed

Fig. 6.26 represents the avg. values of Z-force, sum of details, and percentage contribution by fluctuation for Z-force. The overall trends are almost similar to the observation for spindle torque (Fig. 6.26) with a gradual decrement, and a similar reason is applicable here. At 1200 rpm, a sudden increase in Z-force has been observed for the SCT tool (Fig. 6.26a). Similarly, with SH tool, a sudden increase is seen at 1000 rpm on Avg. sum of details and its percentage contribution by fluctuation (Fig. 6.26b, c). The tool shoulder usually contributes a significant portion of the Z-force at the shoulder weld plate interface. Z-force is responsible for the deformation of the material in vertical direction as well as the consolidation of material behind the tool beneath the shoulder. This will form a sound stir zone and the bead surface texture. A sudden increase in Z-force values represents a difficulty in material deformation. At 1400 rpm, the avg. Z-force, percentage contribution by fluctuations, and avg. sum of details is almost the

same, which depicts that the variation of pin geometry has no significant effect at higher rotational speed.

6.4.3 Bead Surface Analysis

The extracted information in terms of 'sum of details' of spindle torque and Z-force is superimposed on the images of bead surface for different welding and presented in Fig.6.27 and 6.28. It can be observed that the vibrations of these detail signals (frequent change in signal values within a very small time domain) and surface irregularities of the bead are directly related. At the lower rotational speed, signal vibration is higher; bead surfaces also attain a rough texture.

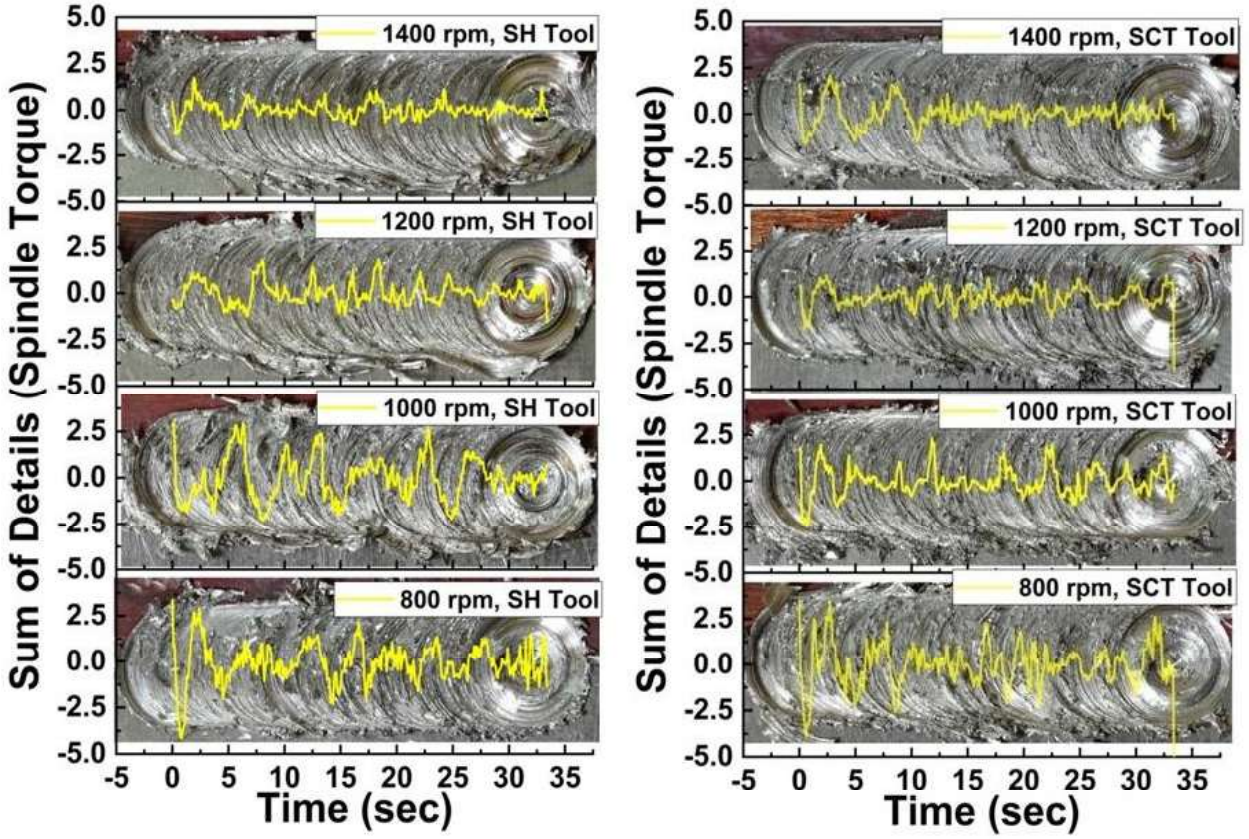

(a) (b)

Fig. 6.27 Variation in weld bead appearance with respect to Sum of details (spindle torque) (a) SH tool, (b) SCT tool

But as rotational speed increases (1200 rpm, 1400 rpm), the signal vibration decreases, and the degree of smoothness of the bead surface increases for both tools. The observation is more prominent in Fig. 6.29 where the magnified view of surface texture for SCT 800 rpm and SH 800 rpm, 1000 rpm reveals a significant irregular texture with high diffusiveness in mixing. At 1400 rpm, the bead surface texture for SCT tool is comparatively smooth with less diffusiveness in mixing. Whereas, for the SH tool at 1400 rpm, the usual semicircular patterns formed due to material extrusion beneath the shoulder surface [23][91] are more distinct, with negligible diffusiveness in material mixing. It reveals the distribution of chatter on the original signal affects the surface quality. This irregular signal pattern reflects abrupt changes in torque and forces at the tool-workpiece interface required for material extrusion and mixing.

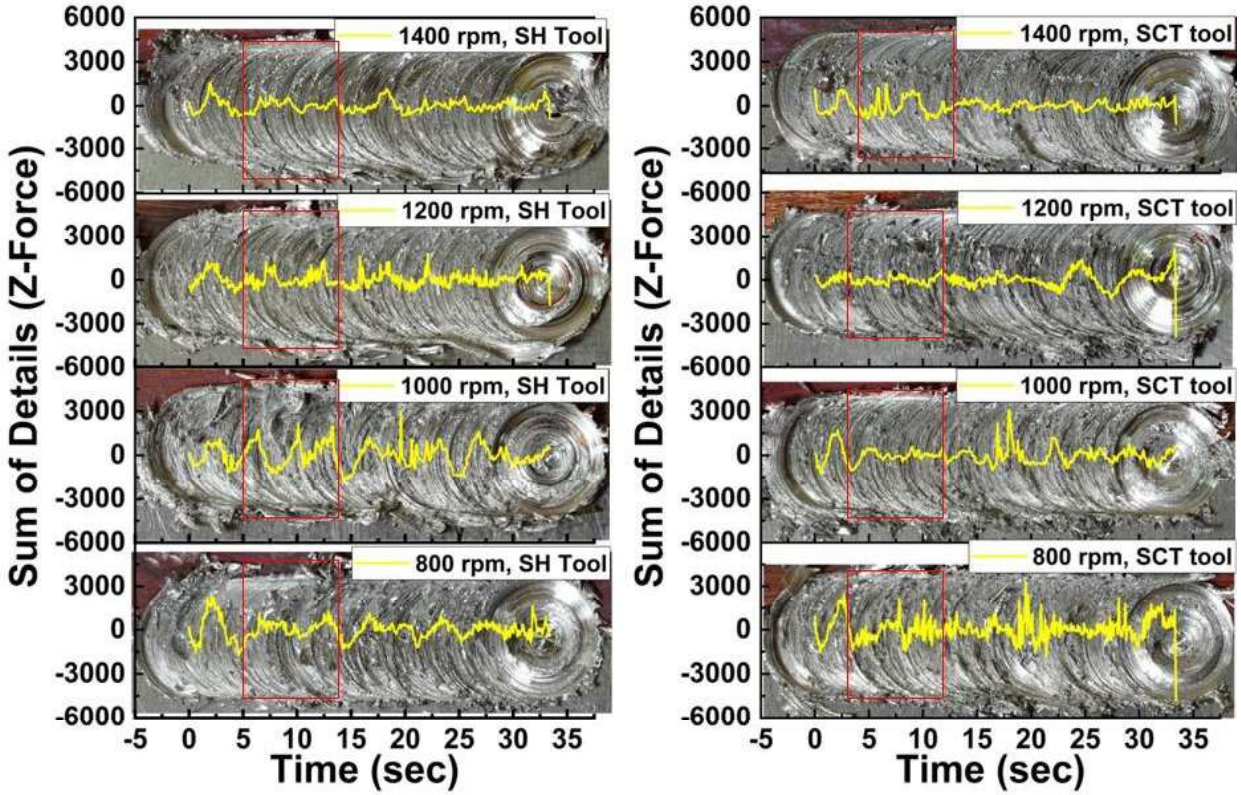

(a) (b)

Fig. 6.28 Variation in weld bead appearance with respect to Sum of details (Z-force) (a) SH tool, (b) SCT tool

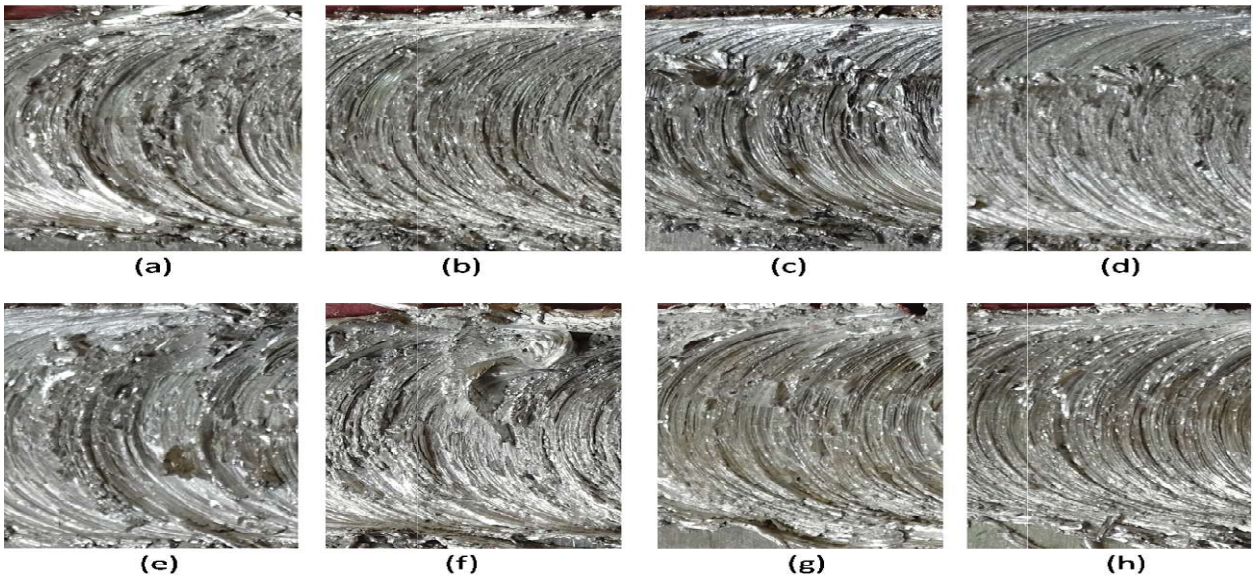

Fig. 6.29 Magnified view of weld bead appearance- SCT tool (a) 800 rpm, (b) 1000 rpm,(c)1200 rpm,(d) 1400 rpm and SH tool (e) 800 rpm,(f) 1000 rpm, (g) 1200 rpm,(h) 1400 rpm

6.4.4 Macrostructure Analysis

The optical images of Al-Cu stir zone for both tools (Fig.6.30) reveal that for SH tool at 800 rpm and 1000 rpm a large chunk of Cu is infused towards the Al from the center of the stir zone. Similarly, the infusion of Cu towards the Al is also observed at 800 rpm and 1000 rpm for SCT tool. It can be stated that at 800 rpm and 1000 rpm both tools have instability in approx Z-force signal which causes unable to deform large Cu and results in large Cu insertion in the mixing zone due to low heat input. Besides slipping occurred at tool work interface at 800 rpm and 1000 rpm for both the tools can be correlated with approximate spindle torque signals and also from sudden changes in the fluctuations of sum of details spindle torque signal. But when rotational speed rises to 1200 rpm, the infusion of Cu to the Al was reduced to a great extent for both SH and SCT tools (Fig. 6.30c, g).

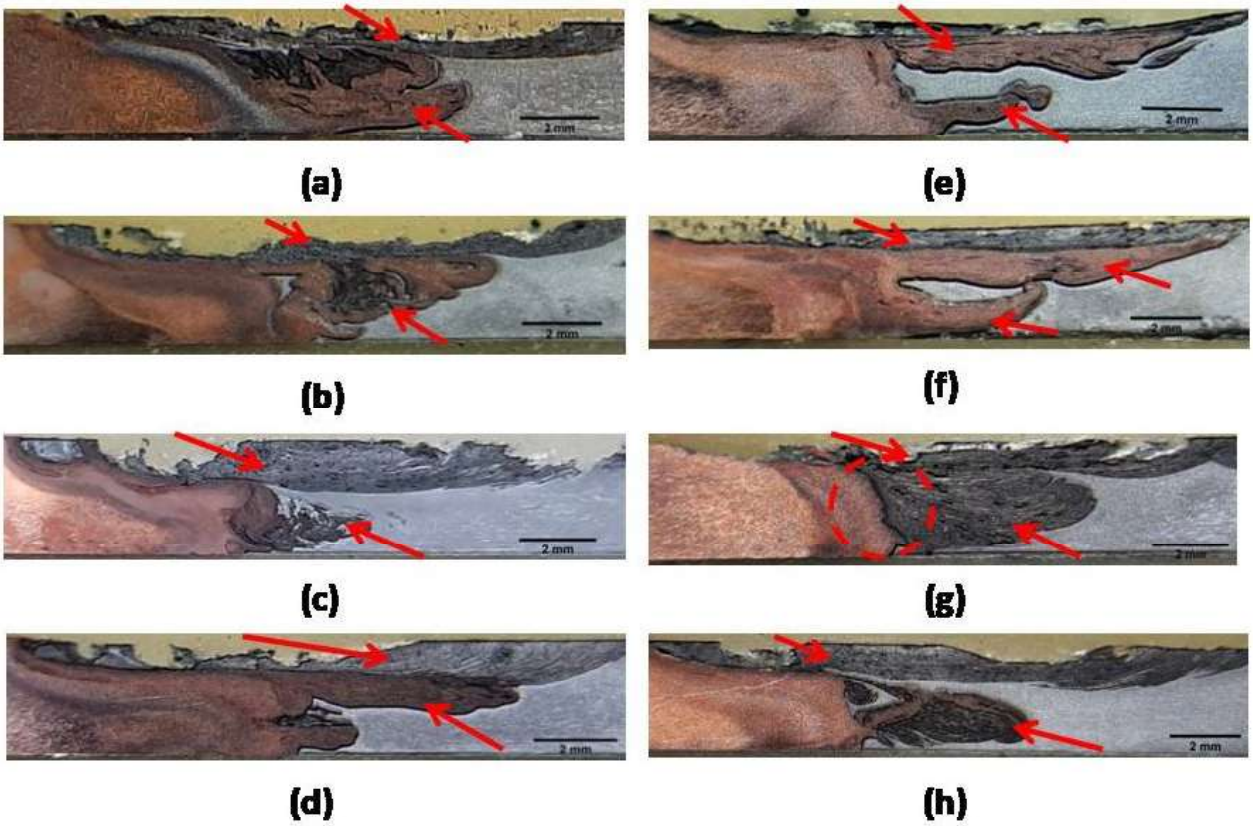

Fig. 6.30 Macrostructure of stir zone - SH tool (a) 800 rpm, (b) 1000 rpm, (c) 1200 rpm, (d) 1400 rpm and SCT tool (e) 800 rpm,(f) 1000 rpm, (g) 1200 rpm,(h) 1400 rpm

The instability of spindle torque approximate signal and Z-force approximate signal also decreases for SH tool. Moreover, an improper mixing between Al and Cu for SCT tool at 1200 rpm formed a defect where sharp discontinuation is seen between Al and Cu at the advancing side. It may be due to higher hard and brittle intermetallics formation at this combination of rotational and traverse speeds [92].This also indicates for SCT tool at 1200 rpm, the deformation of Cu is comparatively less, resulting in the highest increase in spindle torque approximate signal (Fig. 6.20b) and Z-force approximate signal (Fig. 6.24b). At 1400 rpm for SH tool (Fig. 6.30d), large amount of Cu infusion is seen, along with a lamella structure due to adequate heating and pulsating stirring action for SCT tool also lamellae were observed at mixing zone at 1400 rpm. It can also be correlated with better mixing by stability of approximate spindle torque signal and approximate Z-force signal and uniform material mixing by sum of details spindle torque signal and sum of details Z-force signal.

6.4.5 Tensile Strength and Failure Analysis

Fig. 6.31 represents the change of the UTS, YS, and Percentage of elongation for both tools with tool rotational speed (Table 6.2). The trends for all the tensile properties are almost similar, wherewith a rise in tool rotational speed from 800 rpm to 1000 rpm, a very marginal change has been observed. Both tools also observed a sudden drop and a sudden increase in tensile properties at 1200 rpm and 1400 rpm respectively. Material mixing, grain size, formation of the intermetallics, and their distribution are a few critical factors that dictate dissimilar joint strength [48][23][42]. An increase in tool rotational speed typically results in more heat due to increased interaction between the tool and the workpiece [14]. An increased heat contributes to more plasticization of the workpiece thus, improved material mixing is attained. However, increased

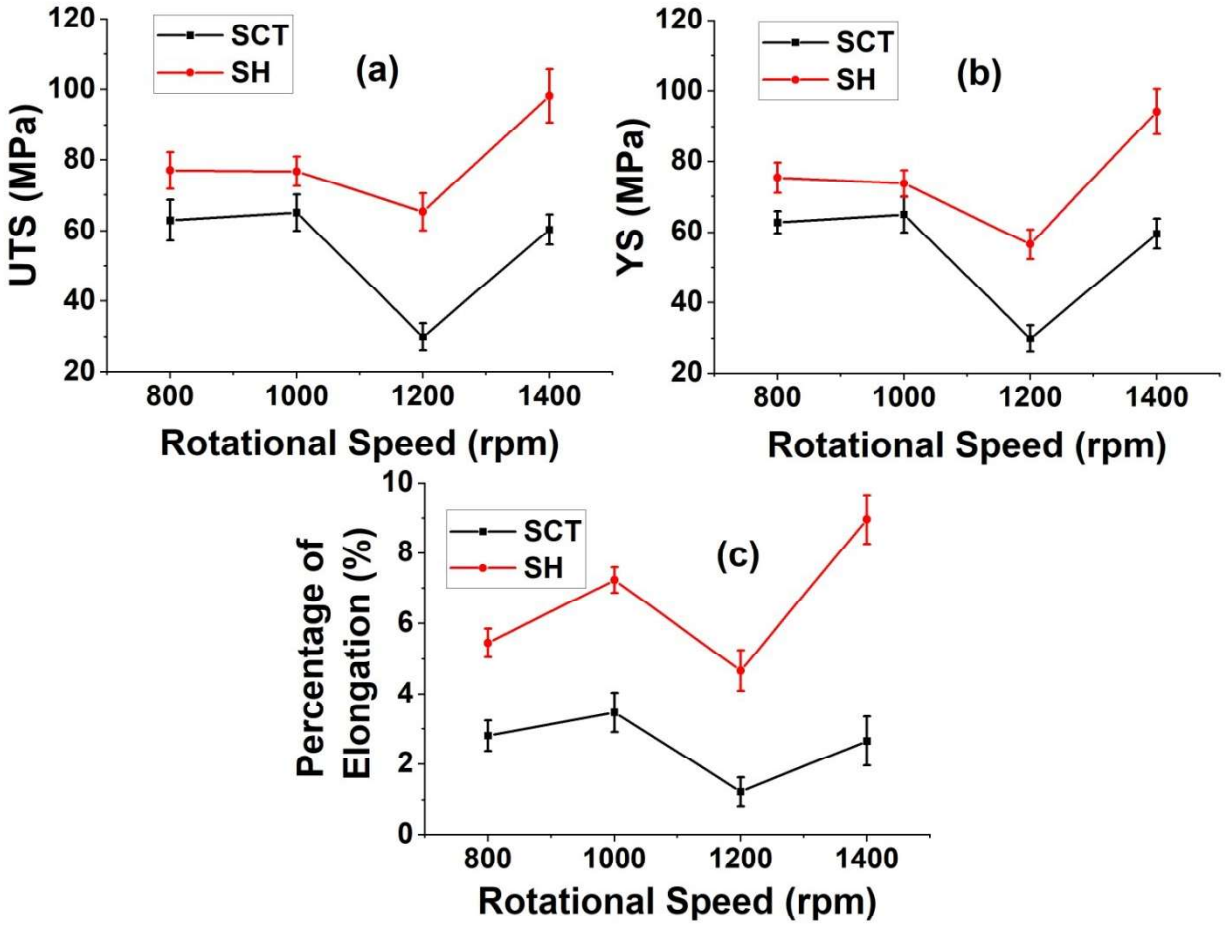

Fig. 6.31 Variation of (a) UTS, (b) YS, and (c) Percentage of elongation with a rotational speed for both tools

heat also contributes more intermetallics generation and coarse grain formation, which are detrimental to mechanical properties in general [93]. It can be seen that SH tool attains increased tensile properties compared to SCT tool, irrespective of the tool's rotational speed. It is due to the generation of continuous fluctuations due to pulse stirring of the SH tool, which facilitates higher deformation and movements of materials in bulk, evident from Fig. 6.30 (other than 1200 rpm SH tool) [48]. The SCT tool shows inferior tensile strength than the SH tool. This can be attributed to the separated material flow along the weld depth (Fig. 6.30) due to thread-incorporated material flow. Another important observation is that at 1200 rpm, the tensile properties for both tools drop suddenly. From Fig.6.30, it can be seen that there is almost negligible amount of mixing between Al and Cu. Moreover, a prominent discontinuity can be observed in the advancing side of the Al-Cu interface for SCT tool.

Table 6.2 Yield strength (YS) and ultimate tensile strength (UTS)for different Rotational speeds

Exp. No.	Tool	Welding speed	Rotational speed(rpm)	YS(MPa)	UTS(MPa)
1	SH	1.5 mm/s	800	75.4	77
2	SH	1.5 mm/s	1000	73.7	76.7
3	SH	1.5 mm/s	1200	56.6	65.3
4	SH	1.5 mm/s	1400	94.2	98.2
5	SCT	1.5 mm/s	800	62.8	62.9
6	SCT	1.5 mm/s	1000	65	65.1
7	SCT	1.5 mm/s	1200	29.9	29.9
8	SCT	1.5 mm/s	1400	59.6	60.3

The continuous growth in both spindle torque and Z-force approximate signal at initial phase of welding (Fig. 6.20and 6.24) also supports the difficulty in deformation at 1200 rpm for SCT tool. It may be due to formation of hard and brittle IMC for SCT tool. For SH tool at 1200 rpm, the disorder is more than SCT tool which can be assessed by fluctuation of sum of details signals. It signifies may be slipping which causes less flow material and deformation and also formation of large intermetallics results decrease in tensile strength. However, at 1400 rpm no such abrupt behavior for both approximate and detail signals of spindle torque (Fig. 6.20 and 6.24) and Z-force (Fig. 6.21 and 6.25) has been observed. The material flow also seemed adequate, reflecting its effect on improved tensile properties. This may be caused by attaining an optimum combination of traverse and rotational speeds [88].

6.6 Outcome of the Present Investigation

The present study analyzed real-time force and torque signals to assess the weld quality for two different tool pin geometries for Al/Cu dissimilar FSW. Signals were decomposed into approximate and detail signals using DWT. The "Maximum energy to entropy" ratio of the highest tensile strength has been considered for selecting the best mother wavelet function for both cases. The essential outcomes are made below.

1. The sym mother wavelet function at level 4 was suitable for analyzing spindle torque signals, and the coif 1mother wavelet function at level 4 is deemed suitable for decomposing the Z-force signal based on the energy to entropy ratio criterion for varying traverse speed. In contrast, the db 3 at level 5 for analyzing spindle torque, and the sym 4 at level 5 is suitable for decomposing the Z-force signal on the energy to entropy ratio criteria for varying rotational speed.
2. The SH tool exhibits fewer fluctuations than the SCT tool for approximate signal of spindle torque and Z-force. It is seen that fluctuations decrease from 1.2 mm/s to 1.8 mm/s but again increase at 2.1 mm/s. It has also seen fluctuations decrease with increasing rotational speed, with a few exceptions for spindle torque (SH 1000 rpm and SCT 1000 rpm) and Z-force (SH 1000 rpm and SCT 1200 rpm).
3. The sum of details signals best reflects the bead surface texture. At 1.2 mm/s, fluctuations in the sum of detail are very high, which shows a rough bead surface with surface voids for the SCT tool. In contrast, at 1.8 mm/s, both tools have fewer

fluctuations, which show a smoother bead surface. Again, when the fluctuations in the sum of details are more at lower rotational speeds (800 rpm, 1000 rpm), the surfaces are seen to attain a rough texture. However, at increased tool rotational speed (1200 rpm, 1400 rpm), the fluctuation decreases, and the smoothness of the bead surface for both tools increases.

4. Macrostructure investigations reveal improper material mixing and the presence of defects like voids at 1.2 mm/s for the SCT tool. A Sudden drops in approximate signal and abrupt fluctuations in detail signal represent tool slipping, which causes improper material mixing. Macrostructure investigations also reveal better material mixing at 1.8 mm/s for both tools. Reduced fluctuation in approx signal and detail signals also supports this observation. It is also seen that fluctuations are more at lower rotational speeds (800 rpm, 1000 rpm) where large Cu was scratched from base metal. At 1400 rpm, fluctuations in approximate signal and sum of detail signal decreases which can correlate with the degree of deformation increases for both tools.
5. At 1.2 mm/s, the SCT tool's tensile strength suddenly drops (30.1 MPa) due to defects in welding caused by slipping phenomenon. At 1200 rpm, the tensile properties for SCT tool drop suddenly and are caused by negligible mixing between Al and Cu. The SCT tool shows minimum tensile strength (29.9 MPa). The continuous growth in the SCT tool's approximate signals of spindle torque and Z-force supports this observation.
6. At1.8 mm/s, both tools demonstrate enhanced tensile strength. In this case, percentage contributed by fluctuations is minimal for both tools for varying traverse speed. Also, at 1400 rpm, the SH tool exhibits the highest tensile strength (98.2 MPa), correlating with the low percentage contributed by fluctuations for varying rotational speed.

Chapter 7:

Conclusions and Future Scope of work

7.1 Conclusions

The present work focused on the combined effect of tool geometries and process parameters. Besides microstructure and mechanical characterization, Weld quality analysis by force and torque signal characterization is also one of the important aspects of this research work. From present work, significant conclusions are as follows:

1. Compared to SCT tool, the SH tool demonstrated superior performance in material flow, bead surface appearance, and tensile strength. This can be attributed to its pulsating stirring action, which results in less tool slipping and better deformation and mixing.
2. Tool geometries affect heat input, but they have an insignificant effect at the highest traverse speed (SH- 536.04 J/mm and SCT-544.56 J/mm) and rotational speed (SH-641.82J/mm and SCT-643.57 J/mm).
3. Excessive heat generation causes rough surface texture where a high amount of flash is generated (SH-1.2 mm/s). In contrast, inadequate heat generation causes poor surface texture with voids (SCT-1.2 mm/s). An adequate amount of heat generation governs proper material over bead surfaces, resulting in smooth surface texture (SH, SCT-1.8 mm/s and SH, SCT-1400 rpm).
4. Tool slipping affects the material flow. For an SCT tool at 1.2 mm/s, excessive tool slipping causes improper material mixing at the nugget, which causes defects in the bead surface and microstructure.
5. At 1200 rpm, the SCT tool shows sharp separation at Al-Cu interface, possibly due to cracks caused by excessive IMCs formation at the Al-Cu interface.
6. At 1400 rpm, both tools demonstrates proper mixing which may be due to adequate heating and stirring for combined tool rotational and traverse speed.
7. At 1400 rpm, the SH tools exhibited the highest tensile strength, measuring 98.2 MPa, among all welding, where significant plastic deformation and the incorporation of bulk copper were observed. In contrast, at 1200 RPM, the SCT tool demonstrated the lowest tensile strength of all the welding processes due to the formation of excessive intermetallic compound, which led to a crack at the aluminum-copper interface.
8. The dispersion strengthening mechanism has improved tensile strength, especially at 1.8 mm/s for both tools (SH- 93.4 MPa and SCT- 80.2 MPa), where small Cu particles are

dispersed in an Al matrix. Whereas, 1.2 mm/s of traverse speed for SCT tool, drastic fall of tensile strength (30.1 MPa) due to defects in the stir zone

9. Intermetallic compound formation during welding plays a vital role in weld strength. It is also present in suitable welding, but excessive or uneven distribution can harm the joint strength. In the case of the SH tool at a speed of 1.8 mm/s and 1000 rpm, the presence of Al_4Cu_9 is significant in improving tensile strength. Similarly, at a speed of 1.5 mm/s and 1400 rpm, Al+Al_2Cu also play an important role in enhancing strength. In contrast, in the SCT tool at 1.5 mm/s and 1200 rpm, the presence of AlCu has a detrimental effect, reducing the strength to 29.9 MPa.
10. EDS analysis shows Continuous interaction of Aland Cu at the interfacial layer is also a good indicator of good quality of mixing and increases the strength.
11. The Formation of excessive IMCs and solid solutions can increase the hardness at the stir zone.
12. Signal characterization by DWT indicates that approximate signals analysis reflects deformation and material flow during welding. In contrast, the accumulated detail signals highlight concerns such as bead surface texture, material uniformity, and instability during the welding process.
13. The SH tool has less fluctuations in approximate and detail signals than the SCT tool, which signifies that the SH tool performs better in deformation, mixing, and less slipping at the tool workpiece interface.
14. At 1.2 mm/s and 1000 rpm for SCT tool, excessive slipping occurred at the tool-workpiece interface and improper material flow with voids was found at the surface and stir zone. The significant fall of approximate signals and abrupt fluctuations in detail signals can relate to this phenomenon.
15. At 1200 rpm and 1.5 mm/s for the SCT tool, a defect was formed where a sharp discontinuity is seen between Al and Cu at the advancing side. It may be due to the higher hard and brittle intermetallics formation at this combination of rotational and traverse speeds. This also indicates that for the SCT tool at 1200 rpm, the deformation of Cu is comparatively less, resulting in the highest increase in spindle torque, approximate signal, and Z-force approximate signal.

16. When both signals (approximate and detail) fluctuated less, better surface finish, material mixing, and enhanced tensile strength were found (SH, SCT-1400 rpm and 1.5 mm/s,1000 rpm and 1.8 mm/s, 1000 rpm).

7.2 Future Scope of Work

1. The present studies can be further developed into corrosion and fatigue analysis, and TEM and EBSD can also be performed to understand better.
2. Cu has excellent electrical properties, so the characterization of the electrical properties of Al and Cu joints can be evaluated.
3. Studies on joining different higher-strength materials can be explored with varying geometries of tools.
4. The present study agrees well with weld quality and wavelets transform analysis. Therefore, wavelet transform analysis of torque and force signal, along with modern computational tools like ANN and Machine learning, can be used for more accurate prediction and control of weld quality.

References

[1] Kulkarni N, Mishra RS, Yuan W. Friction stir welding of dissimilar alloys and materials. Butterworth-Heinemann; 2015.

[2] Zhang W, Shen Y, Yan Y, Guo R, Guan W, Guo G. Microstructure characterization and mechanical behavior of dissimilar friction stir welded Al/Cu couple with different joint configurations. Int J Adv Manuf Technol 2018;94:1021–30. https://doi.org/10.1007/s00170-017-0961-2.

[3] Li XW, Zhang DT, Qiu C, Zhang W. Microstructure and mechanical properties of dissimilar pure copper/1350 aluminum alloy butt joints by friction stir welding. Trans Nonferrous Met Soc China (English Ed 2012;22:1298–306. https://doi.org/10.1016/S1003-6326(11)61318-6.

[4] Yang H, Xie NS, Liu Q. Study on the welding process and application of Al/Cu materials. Adv Mater Res 2013;800:290–3. https://doi.org/10.4028/www.scientific.net/AMR.800.290.

[5] Ouyang J, Yarrapareddy E, Kovacevic R. Microstructural evolution in the friction stir welded 6061 aluminum alloy (T6-temper condition) to copper. J Mater Process Technol 2006;172:110–22. https://doi.org/10.1016/j.jmatprotec.2005.09.013.

[6] Galvão I, Leal RM, Loureiro A, Rodrigues DM. Material flow in heterogeneous friction stir welding of aluminium and copper thin sheets. Sci Technol Weld Join 2010;15:654–60. https://doi.org/10.1179/136217110X12785889550109.

[7] Liu HJ, Shen JJ, Zhou L, Zhao YQ, Liu C, Kuang LY. Microstructural characterisation and mechanical properties of friction stir welded joints of aluminium alloy to copper. Sci Technol Weld Join 2011;16:92–9. https://doi.org/10.1179/1362171810Y.0000000007.

[8] Esmaeili A, Zareie Rajani HR, Sharbati M, Givi MKB, Shamanian M. The role of rotation speed on intermetallic compounds formation and mechanical behavior of friction stir welded brass/aluminum 1050 couple. Intermetallics 2011;19:1711–9. https://doi.org/https://doi.org/10.1016/j.intermet.2011.07.006.

[9] Thomas WM, Nicholas ED, Needham JC, Murch MG, Templesmith P, Dawes CJ, et al. 9125978.8. Int Pat Appl No PCT/GB92/02203 1991.

[10] Patnaik S, Chattopadhyaya S, Shankar S. Friction Stir Welding and its Applications: An Overview. AIP Conf Proc 2022;2681. https://doi.org/10.1063/5.0116234.

[11] Sharma N, SIDDIQUEE AN, others. Friction stir welding of aluminum to copper—An overview. Trans Nonferrous Met Soc China 2017;27:2113–36.

[12] DebRoy T, Bhadeshia HKDH. Friction stir welding of dissimilar alloys - A perspective. Sci Technol Weld Join 2010;15:266–70. https://doi.org/10.1179/174329310X12726496072400.

[13] Thomas W, Dawes C. TWI bulletin 6 November 1995.

[14] Mishra RS, Ma ZY. Friction stir welding and processing. Mater Sci Eng R Reports 2005;50:1–78.

[15] Banik A, Deb Barma J, Saha SC. Effect of threaded pin tool for friction stir welding of AA6061-T6 at varying traverse speeds: torque and force analysis. Iran J Sci Technol Trans Mech Eng 2020;44:749–64.

[16] Mishra R., Ma Z. doi_10.1016_j.mser.2005.07.001 _ Elsevier Enhanced Reader.pdf. Mater Sci Eng R 2005:1–78.

[17] Zhang YN, Cao X, Larose S, Wanjara P. Review of tools for friction stir welding and processing. Can Metall Q 2012;51:250–61. https://doi.org/10.1179/1879139512Y.0000000015.

[18] Mishra RS, Mahoney MW. Friction Stir Welding and Processing, ASM International,(2007). Mater Park Ohio n.d.

[19] Amini A, Asadi P, Zolghadr P. Friction stir welding applications in industry. Adv Frict Stir Weld Process Woodhead Publ 2014.

[20] Mehta KP, Badheka VJ. Materials and Manufacturing Processes A Review on Dissimilar Friction Stir Welding of Copper to Aluminum : Process , Properties and Variants, 2015, p. 37–41. https://doi.org/10.1080/10426914.2015.1025971.

[21] Ouyang J, Yarrapareddy E, Kovacevic R. Microstructural evolution in the friction stir welded 6061 aluminum alloy (T6-temper condition) to copper. J Mater Process Technol 2006;172:110–22.

[22] Medhi T, Roy BS, Saha SC. An experimental investigation on the influence of rotational speed on microstructure and mechanical properties of friction stir welded dissimilar Al-Cu joints. Int J Mater Prod Technol 2020;60:260–73. https://doi.org/10.1504/IJMPT.2020.110117.

[23] Xue P, Ni DR, Wang D, Xiao BL, Ma ZY. Effect of friction stir welding parameters on

the microstructure and mechanical properties of the dissimilar Al-Cu joints. Mater Sci Eng A 2011;528:4683–9. https://doi.org/10.1016/j.msea.2011.02.067.

[24] Zhou L, Li GH, Zhang RX, Zhou WL, He WX, Huang YX, et al. Microstructure evolution and mechanical properties of friction stir spot welded dissimilar aluminum-copper joint. J Alloys Compd 2019;775:372–82. https://doi.org/10.1016/j.jallcom.2018.10.045.

[25] Muthu MFX, Jayabalan V. Tool travel speed effects on the microstructure of friction stir welded aluminum-copper joints. J. Mater. Process. Technol., vol. 217, 2015, p. 105–13. https://doi.org/10.1016/j.jmatprotec.2014.11.007.

[26] Zhang Q, Gong W, Wei LIU. Microstructure and mechanical properties of dissimilar Al--Cu joints by friction stir welding. Trans Nonferrous Met Soc China 2015;25:1779–86.

[27] Medhi T, Yadava MK, Roy BS, Saha SC. An experimental investigation on implications of traverse speed in joining of dissimilar Al–Cu by friction stir welding. Int J Adv Manuf Technol 2019;104:1461–71. https://doi.org/10.1007/s00170-019-04086-2.

[28] Tan CW, Jiang ZG, Li LQ, Chen YB, Chen XY. Microstructural evolution and mechanical properties of dissimilar Al-Cu joints produced by friction stir welding. Mater Des 2013;51:466–73. https://doi.org/10.1016/j.matdes.2013.04.056.

[29] Xue P, Xiao BL, Ni DR, Ma ZY. Enhanced mechanical properties of friction stir welded dissimilar Al-Cu joint by intermetallic compounds. Mater. Sci. Eng. A, vol. 527, 2010, p. 5723–7. https://doi.org/10.1016/j.msea.2010.05.061.

[30] Shankar S, Vilaça P, Dash P, Chattopadhyaya S, Hloch S. Joint strength evaluation of friction stir welded Al-Cu dissimilar alloys. Meas. J. Int. Meas. Confed., vol. 146, Elsevier Ltd; 2019, p. 892–902. https://doi.org/10.1016/j.measurement.2019.07.019.

[31] Shankar S, Chattopadhyaya S. Friction stir welding of commercially pure copper and 1050 aluminum alloys. Mater Today Proc 2019;25:664–7. https://doi.org/10.1016/j.matpr.2019.07.719.

[32] Bhattacharya TK, Das H, Pal TK. Influence of welding parameters on material flow, mechanical property and intermetallic characterization of friction stir welded AA6063 to HCP copper dissimilar butt joint without offset. Trans Nonferrous Met Soc China (English Ed 2015;25:2833–46. https://doi.org/10.1016/S1003-6326(15)63909-7.

[33] Galvão I, Loureiro A, Verdera D, Gesto D, Rodrigues DM. Influence of tool offsetting on the structure and morphology of dissimilar aluminum to copper friction-stir welds. Metall

Mater Trans A Phys Metall Mater Sci 2012;43:5096–105. https://doi.org/10.1007/s11661-012-1351-x.

[34] Galvão I, Oliveira JC, Loureiro A, Rodrigues DM. Formation and distribution of brittle structures in friction stir welding of aluminium and copper: Influence of process parameters. Sci Technol Weld Join 2011;16:681–9. https://doi.org/10.1179/1362171811Y.0000000057.

[35] Mehta KP, Badheka VJ. Effects of tilt angle on the properties of dissimilar friction stir welding copper to aluminum. Mater Manuf Process 2016;31:255–63. https://doi.org/10.1080/10426914.2014.994754.

[36] Hou W, Ahmad Shah LH, Huang G, Shen Y, Gerlich A. The role of tool offset on the microstructure and mechanical properties of Al/Cu friction stir welded joints. J Alloys Compd 2020;825:154045. https://doi.org/10.1016/j.jallcom.2020.154045.

[37] Sinha VC, Kundu S, Chatterjee S. Microstructure and mechanical properties of similar and dissimilar joints of aluminium alloy and pure copper by friction stir welding. Perspect Sci 2016;8:543–6. https://doi.org/10.1016/j.pisc.2016.06.015.

[38] Akinlabi ET, Els-botes A, Mcgrath PJ. CHAPTER 4 : ENGINEERING MATERIALS AND APPLICATIONS Effect of Travel speed on Joint properties of Dissimilar Metal Friction Stir Welds . Engineering n.d.:155–61.

[39] Celik S, Cakir R. Effect of friction stir welding parameters on the mechanical and microstructure properties of the Al-Cu butt joint. Metals (Basel) 2016;6. https://doi.org/10.3390/met6060133.

[40] Rai R, De A, Bhadeshia HKDH, DebRoy T. Review: Friction stir welding tools. Sci Technol Weld Join 2011;16:325–42. https://doi.org/10.1179/1362171811Y.0000000023.

[41] Akinlabi ET. Effect of shoulder size on weld properties of dissimilar metal friction stir welds. J Mater Eng Perform 2012;21:1514–9. https://doi.org/10.1007/s11665-011-0046-6.

[42] Zhou L, Zhang RX, Li GH, Zhou WL, Huang YX, Song XG. Effect of pin profile on microstructure and mechanical properties of friction stir spot welded Al-Cu dissimilar metals. J. Manuf. Process., vol. 36, 2018, p. 1–9. https://doi.org/10.1016/j.jmapro.2018.09.017.

[43] Felix Xavier Muthu M, Jayabalan V. Effect of pin profile and process parameters on microstructure and mechanical properties of friction stir welded Al-Cu joints. Trans

Nonferrous Met Soc China (English Ed 2016;26:984–93. https://doi.org/10.1016/S1003-6326(16)64195-X.

[44] Galvão I, Leal RM, Rodrigues DM, Loureiro A. Influence of tool shoulder geometry on properties of friction stir welds in thin copper sheets. J Mater Process Technol 2013;213:129–35. https://doi.org/10.1016/j.jmatprotec.2012.09.016.

[45] Galvão I, Oliveira JC, Loureiro A, Rodrigues DM. Formation and distribution of brittle structures in friction stir welding of aluminium and copper: Influence of shoulder geometry. Intermetallics, vol. 22, Elsevier Ltd; 2012, p. 122–8. https://doi.org/10.1016/j.intermet.2011.10.014.

[46] MEHTA KP, BADHEKA VJ. Influence of tool pin design on properties of dissimilar copper to aluminum friction stir welding _ Elsevier Enhanced Reader. Trans Nonferrous Met Soc China (English Ed 2017;27:36–54. https://doi.org/10.1016/S1003-6326(17)60005-0.

[47] Mehta KP, Badheka VJ. Influence of tool design and process parameters on dissimilar friction stir welding of copper to AA6061-T651 joints. Int J Adv Manuf Technol 2015;80:2073–82. https://doi.org/10.1007/s00170-015-7176-1.

[48] Sharma N, Siddiquee AN, Khan ZA, Mohammed MT. Material stirring during FSW of Al–Cu: Effect of pin profile. Mater Manuf Process 2018;33:786–94. https://doi.org/10.1080/10426914.2017.1388526.

[49] Beygi R, Mehrizi MZ, Verdera D, Loureiro A. Influence of tool geometry on material flow and mechanical properties of friction stir welded Al-Cu bimetals. J. Mater. Process. Technol., vol. 255, Elsevier; 2018, p. 739–48. https://doi.org/10.1016/j.jmatprotec.2018.01.033.

[50] Kah P, Vimalraj C, Martikainen J, Suoranta R. Factors influencing Al-Cu weld properties by intermetallic compound formation. Int. J. Mech. Mater. Eng., vol. 10, 2015. https://doi.org/10.1186/s40712-015-0037-8.

[51] Mehta M, Chatterjee K, De A. Monitoring torque and traverse force in friction stir welding from input electrical signatures of driving motors. Sci Technol Weld Join 2013;18:191–7. https://doi.org/10.1179/1362171812Y.0000000084.

[52] Arora A, Mehta M, De A, Debroy T. Load bearing capacity of tool pin during friction stir welding. Int J Adv Manuf Technol 2012;61:911–20. https://doi.org/10.1007/s00170-011-

3759-7.

[53] Trimble D, Monaghan J, O'Donnell GE. Force generation during friction stir welding of AA2024-T3. CIRP Ann - Manuf Technol 2012;61:9–12. https://doi.org/10.1016/j.cirp.2012.03.024.

[54] Kumar U, Yadav I, Kumari S, Kumari K, Ranjan N, Kesharwani RK, et al. Defect identification in friction stir welding using discrete wavelet analysis. Adv Eng Softw 2015;85:43–50. https://doi.org/10.1016/j.advengsoft.2015.02.001.

[55] Das B, Pal S, Bag S. A combined wavelet packet and Hilbert-Huang transform for defect detection and modelling of weld strength in friction stir welding process. J Manuf Process 2016;22:260–8. https://doi.org/10.1016/j.jmapro.2016.04.002.

[56] Das B, Pal S, Bag S. Design and development of force and torque measurement setup for real time monitoring of friction stir welding process. Meas J Int Meas Confed 2017;103:186–98. https://doi.org/10.1016/j.measurement.2017.02.034.

[57] Das B, Pal S, Bag S. Torque based defect detection and weld quality modelling in friction stir welding process. J Manuf Process 2017;27:8–17. https://doi.org/10.1016/j.jmapro.2017.03.012.

[58] Das B, Pal S, Bag S. Weld quality prediction in friction stir welding using wavelet analysis. Int J Adv Manuf Technol 2017;89:711–25. https://doi.org/10.1007/s00170-016-9140-0.

[59] Roy RB, Ghosh A, Bhattacharyya S, Mahto RP, Kumari K, Pal SK, et al. Weld defect identification in friction stir welding through optimized wavelet transformation of signals and validation through X-ray micro-CT scan. Int J Adv Manuf Technol 2018;99:623–33. https://doi.org/10.1007/s00170-018-2519-3.

[60] Rabi J, Balusamy T, Raj Jawahar R. Analysis of vibration signal responses on pre induced tunnel defects in friction stir welding using wavelet transform and empirical mode decomposition. Def Technol 2019;15:885–96. https://doi.org/10.1016/j.dt.2019.05.014.

[61] Zeng WM, Wu HL, Zhang J. Effect of tool wear on microstructure, mechanical properties and acoustic emission of friction stir welded 6061 Al alloy. Acta Metall Sin (English Lett 2006;19:9–19. https://doi.org/10.1016/S1006-7191(06)60018-5.

[62] Senthilkumar Subramaniam NS and DAS. SENTHIKUMAR SUBRAMANIAM Acoustic emission−based monitoring approach for friction stir welding of aluminum alloy AA6063-

T6.pdf n.d.

[63] Chen C, Kovacevic R, Jandgric D. Wavelet transform analysis of acoustic emission in monitoring friction stir welding of 6061 aluminum. Int J Mach Tools Manuf 2003;43:1383–90. https://doi.org/10.1016/S0890-6955(03)00130-5.

[64] Boldsaikhan E, Corwin EM, Logar AM, Arbegast WJ. The use of neural network and discrete Fourier transform for real-time evaluation of friction stir welding. Appl Soft Comput J 2011;11:4839–46. https://doi.org/10.1016/j.asoc.2011.06.017.

[65] Yang Y, Kalya P, Landers RG, Krishnamurthy K. Automatic gap detection in friction stir butt welding operations. Int J Mach Tools Manuf 2008;48:1161–9. https://doi.org/10.1016/j.ijmachtools.2008.01.007.

[66] Esmaeili A, Givi MKB, Rajani HRZ. A metallurgical and mechanical study on dissimilar Friction Stir welding of aluminum 1050 to brass (CuZn30). Mater Sci Eng A 2011;528:7093–102. https://doi.org/10.1016/j.msea.2011.06.004.

[67] Frigaard, Grong, Midling OT. A process model for friction stir welding of age hardening aluminum alloys. Metall Mater Trans A Phys Metall Mater Sci 2001;32:1189–200. https://doi.org/10.1007/s11661-001-0128-4.

[68] Kim YG, Fujii H, Tsumura T, Komazaki T, Nakata K. Three defect types in friction stir welding of aluminum die casting alloy. Mater Sci Eng A 2006;415:250–4. https://doi.org/10.1016/j.msea.2005.09.072.

[69] Raturi M, Garg A, Bhattacharya A. Joint strength and failure studies of dissimilar AA6061-AA7075 friction stir welds: Effects of tool pin, process parameters and preheating. Eng Fail Anal 2019;96:570–88.

[70] Schneider J, Beshears R, Nunes AC. Interfacial sticking and slipping in the friction stir welding process. vol. 436, 2006, p. 297–304. https://doi.org/10.1016/j.msea.2006.07.082.

[71] Shahi P, Barmouz M, Asadi P. Force and torque in friction stir welding. 2014. https://doi.org/10.1533/9780857094551.459.

[72] Li G, Zhou L, Zhou W, Song X, Huang Y. Influence of dwell time on microstructure evolution and mechanical properties of dissimilar friction stir spot welded aluminum-copper metals. J Mater Res Technol 2019;8:2613–24. https://doi.org/10.1016/j.jmrt.2019.02.015.

[73] You J, Zhao Y, Dong C, Miao S, Liu Z, Liu L, et al. Microstructural evolution and

mechanical properties of the Al–Cu dissimilar joint enhanced by stationary-dynamic shoulder friction stir welding. J Mater Process Technol 2022;300. https://doi.org/10.1016/j.jmatprotec.2021.117402.

[74] Solchenbach T, Plapper P, Greger M, Biagi J-L, Bour J, Bomfim JAS. Thermal and electrical aging of laser braze-welded aluminum--copper interconnects. Transl Mater Res 2014;1:15001.

[75] Lei Z, Zhang X, Liu J, Li P. Interfacial microstructure and reaction mechanism with various weld fillers on laser welding-brazing of Al/Cu lap joint. J Manuf Process 2021;67:226–40. https://doi.org/10.1016/j.jmapro.2021.04.065.

[76] Beygi R, Kazeminezhad M, Kokabi AH. Microstructural evolution and fracture behavior of friction-stir-welded Al-Cu laminated composites. Metall Mater Trans A Phys Metall Mater Sci 2014;45:361–70. https://doi.org/10.1007/s11661-013-1989-z.

[77] Wan L, Huang Y, Lv Z, Lv S, Feng J. Effect of self-support friction stir welding on microstructure and microhardness of 6082-T6 aluminum alloy joint. Mater. Des., vol. 55, Elsevier Ltd; 2014, p. 197–203. https://doi.org/10.1016/j.matdes.2013.09.073.

[78] Hollatz S, Heinen P, Limpert E, Olowinsky A, Gillner A. Overlap joining of aluminium and copper using laser micro welding with spatial power modulation. Weld World 2020;64:513–22. https://doi.org/10.1007/s40194-020-00848-9.

[79] Safi SV, Amirabadi H, Besharati M, Kazem G. Formation And Distribution of Brittle Structures in Friction Stir Welding of AA 6061 To Copper . Influence of Preheat Seyed Vahid Safi , Hossein Amirabadi , Mohammad Besharati Givi Kazem To cite this version : HAL Id : hal-01306978 Formation And Distribut 2016. https://doi.org/10.13140/RG.2.1.2620.9684.

[80] Fereiduni E, Movahedi M, Kokabi AH. Journal of Materials Processing Technology Aluminum / steel joints made by an alternative friction stir spot welding process 2015;224:1–10.

[81] Esmaeili A, Givi MKB, Rajani HRZ. A metallurgical and mechanical study on dissimilar Friction Stir welding of aluminum 1050 to brass (CuZn30) 2011;528:7093–102. https://doi.org/10.1016/j.msea.2011.06.004.

[82] Yaduwanshi DK, Bag S, Pal S. On the effect of tool offset in hybrid-FSW of copper-aluminium alloy. Mater Manuf Process 2018;33:277–87.

https://doi.org/10.1080/10426914.2017.1279309.

[83] Mubiayi MP, Akinlabi ET. Characterization of the intermetallic compounds in aluminium and copper friction stir spot welds. Mater Today Proc 2017;4:533–40. https://doi.org/10.1016/j.matpr.2017.01.054.

[84] Das B, Pal S, Bag S. Torque based defect detection and weld quality modelling in friction stir welding process. J Manuf Process 2017;27:8–17. https://doi.org/10.1016/j.jmapro.2017.03.012.

[85] Buffa G, Hua J, Shivpuri R, Fratini L. A continuum based fem model for friction stir welding - Model development. Mater. Sci. Eng. A, vol. 419, 2006, p. 389–96. https://doi.org/10.1016/j.msea.2005.09.040.

[86] Nandan R, Roy GG, Lienert TJ, Debroy T. Three-dimensional heat and material flow during friction stir welding of mild steel. Acta Mater 2007;55:883–95. https://doi.org/10.1016/j.actamat.2006.09.009.

[87] Chen CM, Kovacevic R. Finite element modeling of friction stir welding - Thermal and thermomechanical analysis. Int J Mach Tools Manuf 2003;43:1319–26. https://doi.org/10.1016/S0890-6955(03)00158-5.

[88] Elmetwally HT, SaadAllah HN, Abd-Elhady MS, Abdel-Magied RK. Optimum combination of rotational and welding speeds for welding of Al/Cu-butt joint by friction stir welding. Int J Adv Manuf Technol 2020;110:163–75.

[89] Keivani R, Bagheri B, Sharifi F, Ketabchi M, Abbasi M. Effects of pin angle and preheating on temperature distribution during friction stir welding operation. Trans. Nonferrous Met. Soc. China (English Ed., vol. 23, The Nonferrous Metals Society of China; 2013, p. 2708–13. https://doi.org/10.1016/S1003-6326(13)62788-0.

[90] Kadian AK, Biswas P. Effect of tool pin profile on the material flow characteristics of AA6061. J Manuf Process 2017;26:382–92. https://doi.org/10.1016/j.jmapro.2017.03.005.

[91] Avettand-Fènoël MN, Taillard R, Herbelot C, Imad A. Structure and mechanical properties of friction stirred beads of 6082-T6 Al alloy and pure copper. Mater Sci Forum 2010;638–642:1209–14. https://doi.org/10.4028/www.scientific.net/MSF.638-642.1209.

[92] Tra TH, Okazaki M, Hao DD. Tensile Fracture Behavior of Cu/Al Butt Friction Stir Welding: Role of Interface Morphology. J Mater Eng Perform 2022;31:1039–45. https://doi.org/10.1007/s11665-021-06281-3.

[93] T. Akinlabi E, A. Akinlabi S. Effect of Heat Input on the Properties of Dissimilar Friction Stir Welds of Aluminium and Copper. Am J Mater Sci 2012;2:147–52. https://doi.org/10.5923/j.materials.20120205.03.

Abhishek Mandal
1/7/2024